Stabilised Material Point Method for Fluid-Saturated Geomaterials

Zheng, X.

DOI
10.4233/uuid:44d0401b-9dfb-4510-aa0d-07cdf25b3e2f

Publication date
2022

Document Version
Final published version

Citation (APA)
Zheng, X. (2022). *Stabilised Material Point Method for Fluid-Saturated Geomaterials*. [Dissertation (TU Delft), Delft University of Technology]. https://doi.org/10.4233/uuid:44d0401b-9dfb-4510-aa0d-07cdf25b3e2f

STABILISED MATERIAL POINT METHOD FOR FLUID-SATURATED GEOMATERIALS

STABILISED MATERIAL POINT METHOD FOR FLUID-SATURATED GEOMATERIALS

Dissertation

for the purpose of obtaining the degree of doctor
at Delft University of Technology,
by the authority of the Rector Magnificus Prof. dr. ir. T.H.J.J. van der Hagen,
chair of the Board for Doctorates,
to be defended publicly on 29 April 2022 at 10:00 am.

by

Xiangcou ZHENG

Master of Engineering in Civil Engineering,
Central South University, Changsha, China,
born in Hubei, China.

This dissertation has been approved by the promotors.

Composition of the doctoral committee:

Rector Magnificus,	chairperson
Prof. dr. M. A. Hicks,	Delft University of Technology, promotor
Dr. F. Pisanò,	Delft University of Technology, copromotor

Independent members:

Prof. dr. M. Pastor,	Universidad Politecnica de Madrid, Spain
Dr. M. Martinelli,	Deltares
Prof. dr. ir. C. Vuik,	Delft University of Technology
Prof. dr. ir. C. van Rhee,	Delft University of Technology
Dr. H. Hajibeygi,	Delft University of Technology, reserve member

Other members:

Dr. P. J. Vardon,	Delft University of Technology

Keywords: Explicit time integration, Hydromechanical coupling, Implicit time integration, Large deformations, Material point method, Patch recovery, Pore pressure stabilisation

Printed by: Gildeprint Drukkerijen - Enschede

Front & Back: Xiangcou Zheng, Qin Qin

Email: x.zheng-1@tudelft.nl; xiangcouzheng@gmail.com

ISBN: 978-94-6384-324-9

An electronic version of this dissertation is available at
http://repository.tudelft.nl/.

To my beloved family

CONTENTS

List of figures xi

Summary xv

Samenvatting xvii

1 Introduction 1
- 1.1 Background . . . 2
- 1.2 Aims and objectives . . . 4
- 1.3 Outline of the thesis . . . 4
- References . . . 5

2 MPM background and coupled formulation 9
- 2.1 Fundamentals of MPM . . . 10
- 2.2 Existing MPM variants . . . 11
- 2.3 Hydro-mechanical coupled analysis using MPM . . . 15
  - 2.3.1 Two-phase coupled formulations . . . 15
  - 2.3.2 Coupled numerical implementation using MPM . . . 16
  - 2.3.3 Numerical incompressibility constraints in coupled MPM . . . 19
- 2.4 Concluding remarks . . . 20
- References . . . 20

3 An explicit stabilised MPM for hydromechanical problems in two-phase porous media 25
- 3.1 Introduction . . . 26
- 3.2 Coupled formulation for two-phase porous media . . . 27
  - 3.2.1 Governing equations . . . 28
  - 3.2.2 Boundary and initial conditions . . . 29
  - 3.2.3 Integral weak formulation . . . 29
- 3.3 The GC-SRI-patch method: formulation and implementation . . . 30
  - 3.3.1 Spatial discretisation . . . 30
  - 3.3.2 Time discretisation . . . 31
  - 3.3.3 Mitigating pore pressure instabilities in MPM . . . 32
  - 3.3.4 CMPM stress integration/recovery . . . 35
  - 3.3.5 Numerical implementation . . . 35
- 3.4 Verification examples . . . 36
  - 3.4.1 1D consolidation of a soil column . . . 36
  - 3.4.2 Pressurised hollow cylinder . . . 42
  - 3.4.3 2D slumping block (self-weight consolidation) . . . 43
- 3.5 Conclusions . . . 47
- References . . . 50

4 Formulation and verification of a fully implicit three-field MPM for dynamic coupled problems **55**
4.1 Introduction . . . 56
4.2 *u–p–U* formulation of dynamic hydromechanical problems . . . 57
4.3 Numerical implementation of implicit GIMP-patch method . . . 59
4.3.1 Spatial discretisation . . . 59
4.3.2 Time integration . . . 61
4.3.3 Mitigating numerical instabilities in coupled MPM . . . 63
4.4 Numerical verification examples . . . 65
4.4.1 1D coupled problems with small deformations . . . 65
4.4.2 Example 4: large-deformation 1D consolidation of a soil column . . . 72
4.4.3 Example 5: 2D slumping block . . . 73
4.4.4 Calculation time . . . 75
4.5 Conclusions . . . 78
References . . . 78

5 Implicit MPM simulation of large-deformation problems in coupled elasto-plastic geomaterials **83**
5.1 Introduction . . . 84
5.2 Formulation of the implicit GIMP-patch method . . . 85
5.2.1 Governing equations . . . 85
5.2.2 Space and time discretisation . . . 86
5.3 Implementation of the $\overline{\text{B}}$ locking antidote into the implicit GIMP-patch method . . . 88
5.4 Numerical verification and application examples . . . 90
5.4.1 Bearing capacity of a strip footing . . . 90
5.4.2 Earthen slope failure . . . 95
5.4.3 Bearing capacity of a strip footing near a slope . . . 101
5.5 Conclusions . . . 104
References . . . 106

6 Conclusions and Recommendations **109**
6.1 Concluding remarks . . . 110
6.1.1 Explicit stabilised GC-SRI-patch method . . . 110
6.1.2 Fully implicit stabilised GIMP-patch method . . . 111
6.1.3 Implicit $\overline{B}$ GIMP-patch method: application to elastoplastic coupled problems . . . 112
6.2 Recommendations for future research . . . 112

A Composite Material Point Method (CMPM) **115**
References . . . 117

Notation **119**

Acknowledgements **123**

Curriculum Vitæ **125**

List of Publications **127**

LIST OF FIGURES

1.1 Large deformation slope collapse analysis using traditional FEM 2

2.1 MPM discretisation of a representative problem domain 10
2.2 Illustration of the computational cycle of standard MPM for a time step increment Δt 11
2.3 Standard MPM shape function $N_i(x)$ and its gradient $\nabla N_i(x)$ in 1D case . 12
2.4 GIMP shape function $S_{i,mp}(x)$ and its gradient $\nabla S_{i,mp}(x)$ in the 1D case . 12
2.5 MP support domain updating scheme (as linear quadrilaterals) in CPDI2 (Sadeghirad *et al.*, 2013) 13
2.6 B-spline shape functions with modified boundary in 1D case adopted in Steffen *et al.* (2008) 14
2.7 Comparison between shape function gradients of DDMP, standard MPM, and GIMP methods 14
2.8 Coupled MPM implementation using single set of MPs to describe the response of both phases (Soga *et al.*, 2015) 18
2.9 Coupled MPM implementation using two sets of MPs to describe the response of both phases (Soga *et al.*, 2015) 18

3.1 MPs and integration GPs in MPM 33
3.2 Patch recovery of pore pressure increments from GPs to MPs using MLSA . 34
3.3 Numerical implementation of the coupled MPM algorithm 36
3.4 One dimensional consolidation test 37
3.5 Movable top boundary determination for one dimensional analysis 38
3.6 Comparison between GC-SRI-patch, GIMP and analytical consolidation solutions – small deformation analysis 39
3.7 Comparison between GC-SRI-patch and analytical consolidation solutions – large deformation analysis 41
3.8 Comparison between GC-SRI-patch, GIMP and analytical consolidation solutions – large deformation analysis with $U_s = 0.15$ 42
3.9 Hollow cylinder subjected to internal pressurisation 43
3.10 Distribution of simulated excess pore pressure along the radial direction . 43
3.11 Layout of the 2D slumping block problem (self-weight consolidation) . . 44
3.12 Excess pore pressures at $t = 0.05$ s obtained with MPM/GIMP and GC-SRI-patch 45
3.13 Excess pore pressures at different times obtained with GC-SRI-patch (1024 MPs) 46
3.14 Time evolution of excess pore pressure at two reference MPs in the slumping block 47

3.15 Deviatoric stress distributions at different times obtained with GC-SRI-patch (1024 MPs) . . . 48
3.16 Evolution in time of the excess pore pressure profile at the middle section of the slumping block model – GC-SRI-patch solution . . . 49
3.17 Excess pore pressures at different times obtained with GC-SRI-patch . . . 49

4.1 One-dimensional consolidation model . . . 66
4.2 1D small-deformation consolidation of an elastic soil column: comparison between analytical and MPM (implicit GIMP-patch and explicit GC-SRI-patch) solutions . . . 67
4.3 Dependence of the relative pore pressure error e_p on the step size for the considered implicit and explicit MPMs (small deformation consolidation) 68
4.4 Dependence of the relative pore pressure error e_p on the grid cell size at $T_v = 0.5$ (small deformation consolidation) . . . 68
4.5 Π_1-Π_2 pairs considered in the implicit GIMP-patch simulation of dynamic consolidation – cf. Zienkiewicz *et al.* (1980) . . . 69
4.6 Performance of the GIMP-patch method under different dynamic consolidation regimes . . . 70
4.7 Propagation of a shock pressure wave: comparison between analytical and MPM (implicit GIMP-patch and explicit GC-SRI-patch) solutions . . . 72
4.8 Comparison between implicit GIMP-patch, explicit GC-SRI-patch and analytical consolidation solutions – large deformation analysis . . . 73
4.9 Dependence of the relative pore pressure error e_p on the grid cell size at $U_s = 0.5$ (large deformation consolidation) . . . 74
4.10 Layout of the 2D slumping block problems and corresponding application ramp for the gravitational acceleration . . . 74
4.11 Excess pore pressure distributions at $t = 0.18$ s with implicit GIMP and GIMP-patch methods . . . 75
4.12 Excess pore pressure field at different times obtained for a 2D slumping block using the implicit GIMP-patch method (left) and explicit GC-SRI-patch method (right) . . . 76
4.13 Time evolution of the excess pore pressure at three different locations (points P1, P2, P3 in Fig. 4.10) obtained for a 2D slumping block using the implicit GIMP-patch method and the explicit GC-SRI-patch method . 77
4.14 Solid displacement field obtained at $t = 0.5$ s using the implicit GIMP-patch method and the explicit GC-SRI-patch method . . . 77

5.1 One-dimensional GIMP shape function and its gradient sampled at the centre of a grid cell . . . 90
5.2 Reference bearing capacity problem for a strip footing: computational domain and boundary conditions . . . 91
5.3 SD relationship between normalised load (q/c) and displacement (d/B) for the undrained bearing capacity problem in Figure 5.2 . . . 92

5.4 SD mean stress distribution associated with the last calculation step of the analyses in Figure 5.3: (a) implicit GIMP-patch method by Zheng *et al.* (2021a) vs (b) implicit $\overline{\text{B}}$ GIMP-patch method (this study). The horizontal and vertical axes refer to distance non-dimensionalised with respect to the foundation width B 93
5.5 SD mesh sensitivity of the implicit $\overline{\text{B}}$ GIMP-patch method for the undrained bearing capacity problem in Figure 5.2 (including a zoom-in on the detail at bearing failure) 93
5.6 LD normalised load-displacement curves for the undrained bearing capacity problem in Figure 5.2 94
5.7 LD mean stress and deviatoric plastic strain distributions associated with the last calculation step of the analyses in Figure 5.6 (grid cell size $h = 0.125\,\text{m}$). The horizontal and vertical axes refer to distance non-dimensionalised with respect to the foundation width B 95
5.8 Reference slope stability problem: computational domain and boundary conditions 96
5.9 Time evolution of mean stress in the soil during undrained slope failure in softening clay. Results obtained through (a) implicit GIMP-patch method and (b) implicit $\overline{\text{B}}$ GIMP-patch method 97
5.10 Final distributions of deviatoric plastic strain and total displacement associated with undrained slope failure in softening clay. Results obtained through (a) implicit GIMP-patch method; (b) implicit $\overline{\text{B}}$ GIMP-patch method 98
5.11 Time evolution of excess pore pressure and mean effective stress during slope failure in water-saturated sand. Results obtained with soil permeability $k = 1.0 \times 10^{-4}\,\text{m/s}$ and initial dilatancy angle $\psi_{ini} = -5°$ 99
5.12 Configuration after slope failure (at $t = 50.0\,\text{s}$) in water-saturated sand for different values of soil permeability, and associated contours of total pore pressure and deviatoric plastic strain. Results obtained with initial soil dilatancy angle $\psi_{ini} = -5°$ 100
5.13 Time evolution of the excess pore pressure at the point A shown in Figure 5.11a (initially located near the slope toe) for different values of soil permeability. Results obtained with soil initial dilatancy angle $\psi_{ini} = -5°$ 100
5.14 Configuration after slope failure (at $t = 50.0\,\text{s}$) in water-saturated sand for different values of the initial soil dilatancy angle ψ_{ini}, and associated contours of total displacement and deviatoric plastic strain. Results obtained with soil permeability $k = 1.0 \times 10^{-4}\,\text{m/s}$ 101
5.15 Time evolution of the excess pore pressure at the same point A indicated in Figure 5.11a (initially located near the slope toe) for different values of the initial soil dilatancy angle ψ_{ini}. Results obtained with soil permeability $k = 1.0 \times 10^{-4}\,\text{m/s}$ 102
5.16 Reference footing–slope interaction problem: computational domain and boundary conditions (not to scale) 102
5.17 Influence of the footing-to-crest distance on the large-deformation load–displacement response of the foundation in Figure 5.16 103

5.18 Final excess pore pressure (left) and deviatoric plastic strain (right) distributions associated with the footing–slope interaction problem in Figure 5.16. Results obtained with soil permeability $k = 1.0 \times 10^{-4}$ m/s at a total footing settlement equal to $2B$ 104

A.1 CMPM shape functions with C^2 continuity for a central local grid cell . . . 116
A.2 CMPM shape functions with C^1 continuity for a boundary local grid cell . 117

SUMMARY

LARGE deformations in fluid-saturated geomaterials are central to numerous geotechnical applications, such as landslides and dam failures, pile installations, and underground excavations. An in-depth understanding of the soil's hydromechanical behaviour during large-deformation processes is essential for quantitative predictions about such geotechnical problems, which justifies the considerable importance that detailed numerical simulations have been acquiring in this context. However, such simulations are inevitably associated with significant conceptual and computational complexity, due to the simultaneous presence of possibly very large soil deformations along with dynamic effects. Under such conditions, the most common Lagrangian version of the Finite Element Method (FEM) is known to suffer from the mesh distortion that is induced by large deformations, which has a detrimental impact on the accuracy and stability of the corresponding numerical results. The recently developed Material Point Method (MPM) offers a viable solution to the problem by combining the advantages of both Lagrangian and Eulerian methods, and has therefore received increasing attention within the numerical modelling community.

In this thesis, the MPM has been adopted and further developed for the simulation of dynamic large-deformation problems in fluid-saturated porous materials, with emphasis on the stabilisation of the pore pressure field in the presence of low-order interpolation functions. Particular attention has been placed on developing and verifying the proposed stabilised MPM. As a starting point, an explicit version of the proposed coupled MPM, based on the Generalised Interpolation Material Point (GIMP) method, is implemented. Several numerical challenges, such as (i) the implementation of a single-point two-field dynamic formulation, and (ii) the mitigation of pore pressure oscillations, are tackled and discussed in detail. The resulting explicit GC-SRI-patch method includes the use of: (i) selective reduced integration (SRI) for pore pressure evaluation at the central Gauss points of individual background cells; (ii) patch recovery based on a Moving Least Squares Approximation (MLSA) for mapping pore pressure increments from central GPs to Material Point (MPs); (iii) the Composite Material Point Method (MPM) for enhancing the recovery of effective stresses. The analysis of various poroelastic dynamic consolidation problems over a wide range of loading/drainage conditions demonstrates the effectiveness of the explicit GC-SRI-patch method.

Due to the adoption of explicit time integration, the abovementioned (explicit) GC-SRI-patch method, similar to most coupled MPM formulations from the literature, is only conditionally stable, which imposes extreme limitations on the selection of the time step size. As a consequence, the need for stable time integration restricts the applicability of explicit coupled MPM modelling to problems of considerable size and/or duration. A fully implicit stabilised GIMP using a single-point three-field (u–p–U form) formulation is thus proposed, with pore pressure instabilities being remedied through the same MLSA-based patch recovery. Relevant aspects regarding the numerical implementation of the

implicit GIMP-patch method are discussed in detail. This novel method is shown to produce accurate, stable, and oscillation-free results for coupled problems associated with different inertial and deformation regimes, and is generally more efficient than the explicit GC-SRI-patch method owing to the use of larger time steps.

Following the development of the implicit GIMP-patch method in a poroelastic framework, its extension to elastoplastic large-deformation problems is introduced. In particular, in order to analyse coupled large-deformation problems in (nearly) incompressible elastoplastic geomaterials, an anti-locking $\overline{B}$ algorithm is implemented. The effectiveness of the implicit $\overline{B}$ GIMP-patch method in mitigating the detrimental effects of volumetric locking is highlighted through several practical examples, including (i) a strip footing undergoing both small and large settlements on an incompressible soil, (ii) the failure of an earthen slope, and (iii) the bearing capacity of a strip footing near the crest of a slope. The proposed method is proven to be a suitable tool for simulating the large-deformation failure mechanisms in realistic fluid-saturated geotechnical problems and the quantification of the unstable soil mass during the corresponding failure processes.

In summary, the work presented in this thesis is believed to make significant progress on the applicability of stabilised MPM for large-deformation problems in fluid-saturated geomaterials. The presented new developments will support more efficient and accurate assessment of geohazards and soil-structure interaction in geotechnical engineering practice.

SAMENVATTING

Grote vervormingen in vloeistofverzadigde geo-materialen staan centraal in talrijke geotechnische vraagstukken, zoals aardverschuivingen en damdoorbraken, paalinstalleringen en ondergrondse uitgravingen. Een gedegen inzicht in het hydromechanische gedrag van de grond tijdens grote–vervorming processen is noodzakelijk voor kwantitatieve voorspellingen bij zulke vraagstukken, hetwelk de aanzienlijke aandacht rechtvaardigt die gedetailleerde numerieke simulaties hebben ontvangen in deze context. Het is echter onvermijdbaar dat dit type simulatie gepaard gaat met aanzienlijke conceptuele en rekencomplexiteit, door de gelijktijdige aanwezigheid van mogelijk zeer grote vervormingen en dynamische effecten. Onder deze omstandigheden is het bekend dat de meest gebruikte Lagrangiaanse versie van de Eindige Elementen Methode (FEM) lijdt onder de grote vervorming van het netwerk, wat een nadelige invloed heeft op de nauwkeurigheid en stabiliteit van de numerieke resultaten. De onlangs ontwikkelde Materiaal Punt Methode (MPM) biedt een werkbare oplossing voor dit probleem door de voordelen van zowel Lagrangiaanse als Eulerse methoden te combineren, en trekt daardoor de aandacht binnen de numerieke modellerings gemeenschap.

In deze thesis wordt MPM toegepast en verder ontwikkeld voor de simulatie van dynamische grote-vervorming-problemen in vloeistofverzadigde poreuze materialen, met de nadruk op het stabiliseren van het waterspanningsveld in de aanwezigheid van lage-orde interpolatiefuncties. Bijzondere aandacht is uitgegaan naar de ontwikkeling en verificatie van de voorgestelde gestabiliseerde MPM. Als uitgangspunt is een expliciete versie van de voorgestelde gekoppelde MPM, gebaseerd op de Generalised Interpolation Material Point (GIMP) methode, geïmplementeerd. Meerdere numerieke uitdagingen, zoals (i) de implementatie van een enkelpunts-tweevelden dynamische formulering, en (ii) het tegengaan van oscillaties in waterspanningen, worden aangegaan en in detail besproken. De resulterende CG-SRI-patch methode omvat het gebruik van: (i) Selectief Gereduceerde Integratie (SRI) voor de evaluatie van waterspanningen op de centrale gausspunten (GPs) van iedere achtergrondcel; (ii) Patch Recovery gebaseerd op een bewegende kleinstekwadratenmethode (MLSA) voor het overzetten van waterspanningsincrementen van GPs naar de materiaalpunten (MPs); (iii) de Composite Material Point Method (CMPM) voor het verbeterd terugvinden van effectieve spanningen. De analyse van verscheidene poroelastische dynamische consolodatieproblemen over een grote variëteit aan belastings- en drainagerandvoorwaarden bewijst de effectiviteit van de expliciete GC-SRI-patch methode.

Ten gevolge van het toepassen van expliciete tijdsintegratie is de bovengenoemde (expliciete) GC-SRI-patch methode, net als de meeste in de literatuur aangetroffen MPM-formuleringen, slechts voorwaardelijk stabiel, hetgeen belangrijke beperkingen oplegt aan de keuze van een tijdsstapgrootte. De noodzaak van stabiele tijdsintegratie beperkt de toepasbaarheid van expliciete gekoppelde MPM voor problemen van significant formaat of tijdsduur. Een volledig impliciete gestabiliseerde GIMP, gebruikmakend van een

enkelpunts-drievelden (u-p-U) formulering wordt hierom voorgesteld, waarin instabiliteit van het waterspanningsveld worden tegengegaan middels eenzelfde MLSA-gebaseerde patch recovery. Relevante aspecten met betrekking tot de numerieke implementatie van de impliciete GIMP-patch methode worden in detail besproken. Er wordt aangetoond dat deze nieuwe methode accurate, stabiele, oscillatievrije resultaten oplevert voor gekoppelde problemen in verscheidene traagheids- en vervormingsregimes, en is over het algemeen efficiënter dan de expliciete GC-SRI-patch methode dankzij het gebruik van grotere tijdsstappen.

Na de ontwikkeling van de expliciete GIMP-patch methode in een poroelastisch raamwerk, wordt zij verder ontwikkeld voor toepassing op elastoplastische grote-vervorming-problemen. Teneinde gekoppelde grote-vervorming-problemen in (nagenoeg) onsamendrukbare elastoplastische geo-materialen te kunnen analyseren, wordt een anti-locking $\overline{B}$ algoritme geïmplementeerd. De effectiviteit van de impliciete $\overline{B}$ GIMP-patch methode in het tegengaan van de nadelige effecten van volumetrische locking wordt benadrukt door een aantal praktijkvoorbeelden, waaronder (i) een strokenfundering die zowel grote als kleine zettingen op een onsamendrukbare ondergrond ondergaat, (ii) het bezwijken van een aarden talud, en (iii) de draagkracht van een strokenfundering in de nabijheid van de kruin van een talud. Het wordt aangetoond dat de voorgestelde methode een geschikt gereedschap is voor het simuleren van bezwijkmechanismen bij grote vervormingen in realistische vloeistofverzadigde geotechnische vraagstukken, en ook voor de kwantificatie van de instabiele grondmassieven gedurende deze bezwijkprocessen. Samenvattend kan worden gesteld dat het in deze thesis gepresenteerde werk wordt verondersteld een significante bijdrage te leveren aan de toepasbaarheid van MPM voor grote-vervorming-problemen in vloeistofverzadigde geo-materialen. De hier voorgestelde ontwikkelingen zullen een verbeterde analyse van geotechnische risico's en grond-bouwwerk interactie in de geotechnische ingenieurspraktijk ondersteunen.

1

INTRODUCTION

1

1.1. BACKGROUND

In the field of geotechnical engineering, natural phenomena, such as landslides and debris flows, often result in catastrophic events due to the sudden release and rapid large movement of soil masses. Therefore, the reliable prediction of such events and understanding the soil mechanical processes during these large deformation processes are of particular importance for researchers and engineers for minimising their potential consequences. However, numerical simulation of large deformations is known to be particularly challenging when attempted through conventional, mesh-based Lagrangian methods such as the Finite Element Method (FEM). In most cases of dealing with large deformations, such methods can lead to aborted numerical simulations or misleading results due to excessive mesh distortion (Lee & Bathe, 1993; Rajendran, 2010). As an example, Figure 1.1 gives the solution of a typical geotechnical problem, involving a large deformation slope collapse, as analysed using traditional FEM. Figure 1.1b illustrates that severe mesh distortion occurs during the large deformation collapse process. This severe mesh distortion makes the traditional FEM unsuitable for handling large deformation problems unless special mesh treatments are performed.

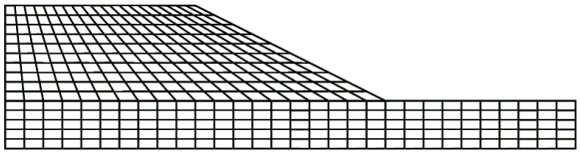

(a) Initial undeformed mesh

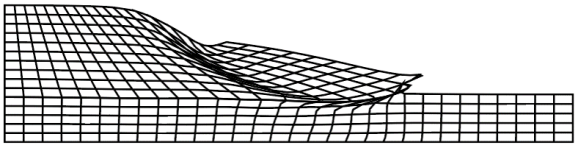

(b) Final deformed configuration

Figure 1.1: Large deformation slope collapse analysis using traditional FEM

To remedy the mesh-distortion issue, various approaches, such as *Arbitary Lagrangian–Eulerian* (ALE) (Hirt *et al.*, 1974; Donea *et al.*, 1982; Nazem *et al.*, 2008; Barlow *et al.*, 2016) and *Coupled Eulerian–Lagrangian* (CEL) modelling (Qiu *et al.*, 2011; Dutta *et al.*, 2015; Wang *et al.*, 2015), have been implemented. Alternatively, several mesh-free/meshless methods have also been proposed, such as the *Smoothed Particle Hydrodynamics* (SPH) method (Gingold & Monaghan, 1977; Monaghan, 1994; Randles & Libersky, 1996; Liu & Liu, 2010; Pastor *et al.*, 2014, 2018), the *Material Point Method* (MPM) (Sulsky *et al.*, 1994, 1995; Bardenhagen & Kober, 2004; Więckowski, 2004), the *element-free Galerkin method* (Belytschko *et al.*, 1995; Beissel & Belytschko, 1996; Häussler-Combe & Korn, 1998; Zhang *et al.*, 2008; Bourantas *et al.*, 2021; Zhang *et al.*, 2021), the *Particle Finite Element Method* (PFEM) (Oñate *et al.*, 2004; Monforte *et al.*, 2017; Della Vecchia *et al.*, 2019; Yuan *et al.*, 2020, 2021), and *Optimal Transportation Meshfree (OTM)* scheme (Li *et al.*, 2010, 2014; Navas *et al.*, 2016, 2018). Each one of these methods features a specific mix of advantages and drawbacks, and recent reviews on the subject of large

deformation modelling can be found, for instance, in Soga *et al.* (2015), Chen *et al.* (2017), and de Vaucorbeil *et al.* (2020). As MPM combines the advantages of both Lagrangian and Eulerian methods, it has been gaining recognition as a robust approach for this class of problem, and has been applied to soil discharging (Więckowski, 2004), landslides (Andersen, 2009; Andersen & Andersen, 2010; Soga *et al.*, 2015; Wang *et al.*, 2018; Yerro *et al.*, 2019), the bearing capacity of footings (Kiriyama & Higo, 2020; Bisht *et al.*, 2021; Wang *et al.*, 2021), anchor pull-out (Coetzee *et al.*, 2005; Ceccato *et al.*, 2020; Liang *et al.*, 2021), cone penetration (Beuth, 2012; Ceccato *et al.*, 2016; Martinelli & Galavi, 2021) and so on. It is also the approach investigated in this thesis.

The numerical analysis of large-deformation dynamic processes in fluid-saturated porous media is extremely relevant to a number of geotechnical problems, as soil masses are natural assemblies of different components and frequently considered as porous media. Therefore, it is quite common, and even necessary in numerical simulations, to include the interaction/coupling between the porous soil skeleton and pore water during the large deformation process. Owing to the algorithmic similarities between MPM and well-studied FEM, MPM seems to be extremely suitable for capturing hydro-mechanical behaviour in large deformation analysis with the incorporation of a suitable soil constitutive model.

However, on the one hand this coupling between two phases frequently adds considerable complexities to the numerical implementation, as well as to the analysis of practical applications, especially when dynamic effects are included. On the other hand, when introducing MPM to two-phase coupled large deformation analysis, it performs poorly in the presence of incompressibility constraints when based on low-order spatial interpolation. This incompressibility constraint can lead to pore pressure instabilities and an over-stiff response of soil skeleton in fluid-saturated soil media. In addition, most current available MPM developments for coupled problems are based on explicit time integration, which is conditionally stable and subjected to the need for extremely small time steps to fulfill the stability condition in nearly or fully incompressible materials. This stability requirement greatly prevents the large-scale application of coupled MPMs for two-phase large deformation simulations.

In this research, the purpose is to develop stabilised MPM approaches for large deformation dynamic problems in fluid-saturated geomaterials. Both explicit and fully implicit coupled MPMs, in conjunction with pore pressure stabilisation techniques and anti-locking algorithms, are implemented to capture the dynamic hydro-mechanical behaviour in two-phase large deformation analysis. It is acknowledged that a comprehensive large deformation analysis framework should be able, simultaneously, to (i) solve the relevant governing equations with respect to the current configuration, and (ii) describe the possible occurrence of large strains (i.e., significant local variations of shape/size) using suitable finite strain measures. However, in this study, the proposed stabilised coupled MPM method does not account for the latter aspect, in that strains are measured according to the simpler infinitesimal definition. Further extension to a finite strain formulation will not jeopardise the effectiveness of the proposed approach in terms of accuracy and/or representation of the stress field.

1.2. AIMS AND OBJECTIVES

THE overall aim of this thesis is to develop stabilised coupled MPM approaches for simulating fully coupled, large deformation, dynamic problems in fluid-infiltrated porous materials, which can be readily applied to simulate practical and challenging geotechnical problems involving large deformations. This research progresses from an explicit stabilised MPM to a fully implicit stabilised MPM, and from poroelastic to elasto-plastic materials. In detail, the further objectives of this thesis are:

- To gain a better insight into the implementation of the fully coupled governing equations within the framework of the Generalised Interpolation Material Point (GIMP) method using both two-field and three-field formulations;
- To develop stabilised schemes for pore pressure recovery and to incorporate anti-locking algorithms for dealing with nearly incompressible fluid-infiltrated porous geomaterials;
- To fully understand the difference in numerical implementations using explicit and fully implicit time integration schemes;
- To validate both explicit and implicit stabilised coupled MPM approaches against analytical/numerical solutions and evaluate their computational performances through several numerical examples;
- To apply the proposed coupled GIMP method for the solution of geo-problems spanning weak to strong hydro-mechanical coupling and small to large deformations.

1.3. OUTLINE OF THE THESIS

THE thesis contains 6 main chapters, and the outline for the remaining chapters is:

- Chapter 2: Describes some fundamentals of MPM and reviews the existing MPM variants relevant to this thesis. This chapter also briefly summarises the equations governing two-phase, fully coupled, problems from three different types of formulation, and coupled numerical implementations using MPM are then reviewed and categorized into different groups.
- Chapter 3: Elaborates an explicit stabilised MPM, based on GIMP with Selective Reduced Integration (SRI), for mitigating the numerical oscillations that occur in nearly incompressible coupled problems. Particular attention is paid to the numerical implementation based on a single-point two-field velocity (v–w) formulation, the patch recovery of pore pressure increments using a Moving Least Squares Approximation (MLSA), and the extension of the Composite Material Point Method (CMPM) for effective stress recovery. The computational performance of the proposed explicit GC-SRI-patch method is verified through analysing various poroelastic consolidation problems, with an emphasis on the representation of pore pressures in time and space.
- Chapter 4: Presents the implementation of a fully implicit stabilised GIMP-patch method using a three-field (u–p–U) form for dynamic problems in two-phase poroelastic

media. Emphasis is on the verification of its accuracy under different regimes of material deformation (small versus large) and dynamic motion (slow versus fast). Special attention is also devoted to highlighting the computational convenience of implicit MPM modelling in comparison to the explicit MPM.

- Chapter 5: Extends the implicit GIMP-patch method for large deformation problems to two-phase elastoplastic geomaterials. The FEM version of the $\bar{B}$ approach for alleviating locking issues caused by the plastic incompressibility constraint is introduced into the implicit GIMP-patch method, and a detailed numerical implementation of the implicit $\bar{B}$ GIMP-patch method is presented. Particular emphasis is placed on (i) mitigating effective stress oscillations and (ii) solving several two-phase, coupled, large deformation geotechnical problems incorporating the use of a Mohr-Coulomb strain softening model.

- Chapter 6: Summarises the key conclusions of this thesis, and outlines some recommendations for future investigation.

REFERENCES

Andersen, S. (2009). *Material-point analysis of large-strain problems: modelling of landslides*. Ph.D. thesis, Aalborg University.

Andersen, S. & Andersen, L. (2010). Modelling of landslides with the material-point method. *Computational Geosciences* **14**, No. 1, 137–147.

Bardenhagen, S. G. & Kober, E. M. (2004). The generalized interpolation material point method. *Computer Modeling in Engineering and Sciences* **5**, No. 6, 477–496.

Barlow, A. J., Maire, P. H., Rider, W. J., Rieben, R. N. & Shashkov, M. J. (2016). Arbitrary Lagrangian–Eulerian methods for modeling high-speed compressible multimaterial flows. *Journal of Computational Physics* **322**, 603–665.

Beissel, S. & Belytschko, T. (1996). Nodal integration of the element-free Galerkin method. *Computer Methods in Applied Mechanics and Engineering* **139**, No. 1-4, 49–74.

Belytschko, T., Organ, D. & Krongauz, Y. (1995). A coupled finite element-element-free Galerkin method. *Computational Mechanics* **17**, No. 3, 186–195.

Beuth, L. (2012). *Formulation and application of a quasi-static material point method*. Ph.D. thesis, University of Stuttgart.

Bisht, V., Salgado, R. & Prezzi, M. (2021). Simulating penetration problems in incompressible materials using the material point method. *Computers and Geotechnics* **133**, 103593.

Bourantas, G., Zwick, B. F., Joldes, G. R., Wittek, A. & Miller, K. (2021). Simple and robust element-free galerkin method with almost interpolating shape functions for finite deformation elasticity. *Applied Mathematical Modelling* **96**, 284–303.

Ceccato, F., Beuth, L., Vermeer, P. A. & Simonini, P. (2016). Two-phase material point method applied to the study of cone penetration. *Computers and Geotechnics* **80**, 440–452.

Ceccato, F., Bisson, A. & Cola, S. (2020). Large displacement numerical study of 3D plate anchors. *European Journal of Environmental and Civil Engineering* **24**, No. 4, 520–538.

Chen, J. S., Hillman, M. & Chi, S. W. (2017). Meshfree methods: progress made after 20 years. *Journal of Engineering Mechanics* **143**, No. 4, 04017001.

Coetzee, C., Vermeer, P. & Basson, A. (2005). The modelling of anchors using the material point method. *International Journal for Numerical and Analytical Methods in Geomechanics* **29**, No. 9, 879–895.

de Vaucorbeil, A., Nguyen, V. P., Sinaie, S. & Wu, J. Y. (2020). Chapter two - material point method after 25 years: Theory, implementation, and applications. Elsevier, pp. 185–398.

Della Vecchia, G., Cremonesi, M. & Pisanò, F. (2019). On the rheological characterisation of liquefied sands through the dam-breaking test. *International Journal for Numerical and Analytical Methods in Geomechanics* **43**, No. 7, 1410–1425.

Donea, J., Giuliani, S. & Halleux, J.-P. (1982). An arbitrary Lagrangian–Eulerian finite element method for transient dynamic fluid–structure interactions. *Computer Methods in Applied Mechanics and Engineering* **33**, No. 1-3, 689–723.

Dutta, S., Hawlader, B. & Phillips, R. (2015). Finite element modeling of partially embedded pipelines in clay seabed using coupled Eulerian–Lagrangian method. *Canadian Geotechnical Journal* **52**, No. 1, 58–72.

Gingold, R. A. & Monaghan, J. J. (1977). Smoothed particle hydrodynamics: theory and application to non-spherical stars. *Monthly Notices of the Royal Astronomical Society* **181**, No. 3, 375–389.

Häussler-Combe, U. & Korn, C. (1998). An adaptive approach with the element–free–galerkin method. *Computer Methods in Applied Mechanics and Engineering* **162**, No. 1-4, 203–222.

Hirt, C. W., Amsden, A. A. & Cook, J. (1974). An arbitrary Lagrangian–Eulerian computing method for all flow speeds. *Journal of computational physics* **14**, No. 3, 227–253.

Kiriyama, T. & Higo, Y. (2020). Arbitrary particle domain interpolation method and application to problems of geomaterial deformation. *Soils and Foundations* **60**, No. 6, 1422–1439.

Lee, N. S. & Bathe, K. J. (1993). Effects of element distortions on the performance of isoparametric elements. *International Journal for Numerical Methods in Engineering* **36**, No. 20, 3553–3576.

Li, B., Habbal, F. & Ortiz, M. (2010). Optimal transportation meshfree approximation schemes for fluid and plastic flows. *International Journal for Numerical Methods in Engineering* **83**, No. 12, 1541–1579.

Li, B., Stalzer, M. & Ortiz, M. (2014). A massively parallel implementation of the optimal transportation meshfree method for explicit solid dynamics. *International Journal for Numerical Methods in Engineering* **100**, No. 1, 40–61.

Liang, W., Zhao, J., Wu, H. & Soga, K. (2021). Multiscale modeling of anchor pullout in sand. *Journal of Geotechnical and Geoenvironmental Engineering* **147**, No. 9, 04021091.

Liu, M. & Liu, G. (2010). Smoothed particle hydrodynamics (SPH): an overview and recent developments. *Archives of computational methods in engineering* **17**, No. 1, 25–76.

Martinelli, M. & Galavi, V. (2021). Investigation of the material point method in the simulation of cone penetration tests in dry sand. *Computers and Geotechnics* **130**, 103923.

Monaghan, J. J. (1994). Simulating free surface flows with SPH. *Journal of Computational Physics* **110**, No. 2, 399–406.

Monforte, L., Carbonell, J. M., Arroyo, M. & Gens, A. (2017). Performance of mixed formulations for the particle finite element method in soil mechanics problems. *Computational Particle Mechanics* **4**, No. 3, 269–284.

Navas, P., Rena, C. Y., López-Querol, S. & Li, B. (2016). Dynamic consolidation problems in saturated soils solved through u–w formulation in a LME meshfree framework. *Computers and Geotechnics* **79**, 55–72.

Navas, P., Sanavia, L., López-Querol, S. & Rena, C. Y. (2018). Explicit meshfree solution for large deformation dynamic problems in saturated porous media. *Acta Geotechnica* **13**, No. 2, 227–242.

Nazem, M., Sheng, D., Carter, J. P. & Sloan, S. W. (2008). Arbitrary Lagrangian–Eulerian method for large-strain consolidation problems. *International Journal for Numerical and Analytical Methods in Geomechanic* **32**, 1023–1050.

Oñate, E., Idelsohn, S. R., Del Pin, F. & Aubry, R. (2004). The particle finite element method—an overview. *International Journal of Computational Methods* **1**, No. 02, 267–307.

Pastor, M., Blanc, T., Haddad, B., Petrone, S., Morles, M. S., Drempetic, V., Issler, D., Crosta, G., Cascini, L., Sorbino, G. *et al.* (2014). Application of a SPH depth-integrated model to landslide run-out analysis. *Landslides* **11**, No. 5, 793–812.

Pastor, M., Yague, A., Stickle, M., Manzanal, D. & Mira, P. (2018). A two-phase SPH model for debris flow propagation. *International Journal for Numerical and Analytical Methods in Geomechanic* **42**, No. 3, 418–448.

Qiu, G., Henke, S. & Grabe, J. (2011). Application of a Coupled Eulerian–Lagrangian approach on geomechanical problems involving large deformations. *Computers and Geotechnics* **38**, No. 1, 30–39.

Rajendran, S. (2010). A technique to develop mesh-distortion immune finite elements. *Computer Methods in Applied Mechanics and Engineering* **199**, No. 17-20, 1044–1063.

Randles, P. & Libersky, L. D. (1996). Smoothed particle hydrodynamics: some recent improvements and applications. *Computer Methods in Applied Mechanics and Engineering* **139**, No. 1-4, 375–408.

Soga, K., Alonso, E., Yerro, A., Kumar, K. & Bandara, S. (2015). Trends in large-deformation analysis of landslide mass movements with particular emphasis on the material point method. *Géotechnique* **66**, No. 3, 248–273.

Sulsky, D., Chen, Z. & Schreyer, H. L. (1994). A particle method for history-dependent materials. *Computer Methods in Applied Mechanics and Engineering* **118**, No. 1-2, 179–196.

Sulsky, D., Zhou, S. J. & Schreyer, H. L. (1995). Application of a particle-in-cell method to solid mechanics. *Computer Physics Communications* **87**, No. 1-2, 236–252.

Wang, B., Vardon, P. J. & Hicks, M. A. (2018). Rainfall-induced slope collapse with coupled material point method. *Engineering Geology* **239**, 1–12.

Wang, D., Bienen, B., Nazem, M., Tian, Y., Zheng, J., Pucker, T. & Randolph, M. F. (2015). Large deformation finite element analyses in geotechnical engineering. *Computers and Geotechnics* **65**, 104–114.

Wang, L., Coombs, W. M., Augarde, C. E., Cortis, M., Brown, M. J., Brennan, A. J., Knappett, J. A., Davidson, C., Richards, D., White, D. J. *et al.* (2021). An efficient and locking-free material point method for three-dimensional analysis with simplex elements. *International Journal for Numerical Methods in Engineering* .

Więckowski, Z. (2004). The material point method in large strain engineering problems. *Computer Methods in Applied Mechanics and Engineering* **193**, No. 39-41, 4417–4438.

Yerro, A., Soga, K. & Bray, J. (2019). Runout evaluation of oso landslide with the material point method. *Canadian Geotechnical Journal* **56**, No. 9, 1304–1317.

Yuan, W.-H., Liu, K., Zhang, W., Dai, B. & Wang, Y. (2020). Dynamic modeling of large deformation slope failure using smoothed particle finite element method. *Landslides* , 1–13.

Yuan, W.-H., Wang, H.-C., Zhang, W., Dai, B.-B., Liu, K. & Wang, Y. (2021). Particle finite element method implementation for large deformation analysis using abaqus. *Acta Geotechnica* , 1–14.

Zhang, X., Zhang, P., Qin, W. & Shi, X. (2021). An adaptive variational multiscale element free Galerkin method for convection–diffusion equations. *Engineering with Computers* , 1–18.

Zhang, Z., Liew, K. M., Cheng, Y. & Lee, Y. (2008). Analyzing 2D fracture problems with the improved element-free Galerkin method. *Engineering Analysis with Boundary Elements* **32**, No. 3, 241–250.

2

MPM BACKGROUND AND LITERATURE REVIEW

2.1. FUNDAMENTALS OF MPM

THE Material Point Method (MPM) is a well-developed numerical method, which was first proposed by Sulsky *et al.* (1994) for solid mechanics. This method was derived from the Particle-in-cell (PIC) method (Harlow, 1964), that was originally developed for solving complex fluid mechanics problems. To overcome the excessive energy dissipation of the PIC method, Brackbill & Ruppel (1986) and Brackbill *et al.* (1988) proposed the so-called Fluid Implicit Particle (FLIP) method, with particles carrying all physical properties for the numerical calculation. The FLIP method was later modified and reformulated for numerical simulation in solid mechanics by Sulsky *et al.* (1994), and then the method became known as the MPM for applications in upcutting and upsetting and Taylor impact problems (Sulsky & Schreyer, 1996).

As a variant of traditional FEM, the MPM is viewed as a hybrid Eulerian–Lagrangian approach, as it adopts two different discretisations (as shown in Figure 2.1): a fixed Eulerian background grid and moving Lagrangian particles. As an example, Figure 2.1 displays the typical MPM discretisation of a representative problem with a reference configuration domain Ω_0 at time t and a current configuration domain Ω at time $t+\Delta t$. Note that the background grid is used solely for solving the governing equations and remains unchanged at the beginning of each computational step, while the MPs carry all state variables and move through the background mesh to track the configuration of the problem domain. In this way, the MPM can effectively avoid the treatment of convection terms in the Eulerian formulation and excessive mesh distortion in the Lagrangian formulation (Sulsky *et al.*, 1994), which is extremely suitable for large deformation analysis.

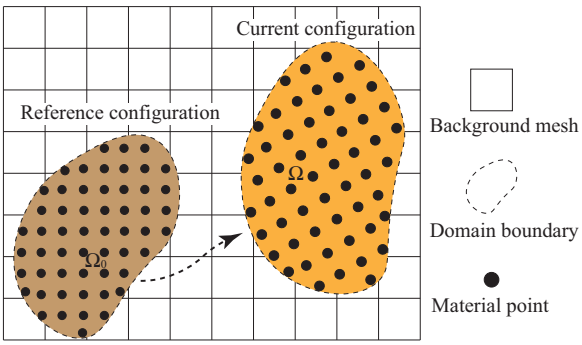

Figure 2.1: MPM discretisation of a representative problem domain

For a more detailed description, Figure 2.2 gives a representative computational cycle of the standard MPM for a considered time step increment Δt. Slightly different from the computational process of traditional FEM, the computational cycle of MPM includes the following main steps (Sulsky *et al.*, 1994; Soga *et al.*, 2016; Wang, 2017): (a) mapping information from material points to grid nodes; (b) solving the governing equations at the grid nodes using UL-FEM; (c) upgrading the state variables of the MPs using the updated nodal variables and resetting the background grid.

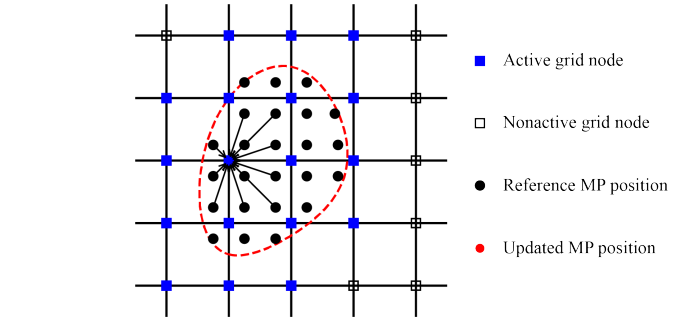

(a) Mapping variables from MPs to nodes

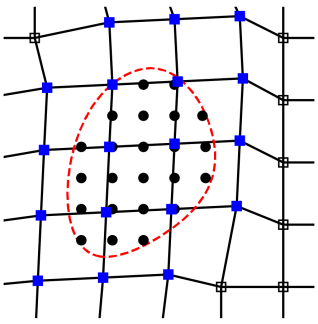

(b) Solving governing equations at nodes and updating grid

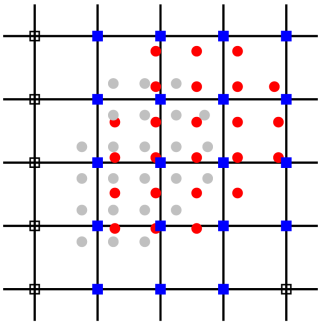

(c) Updating state variables from nodes to MPs and resetting background grid

Figure 2.2: Illustration of the computational cycle of standard MPM for a time step increment Δt

2.2. EXISTING MPM VARIANTS

THIS section reviews the existing MPM variants that are available in literature and briefly describes their main differences with standard MPM. Particular emphasis is placed upon the recent developments in improving the accuracy of original MPM.

For standard MPM, a linear shape function, which is exactly the same as that adopted in the linear FEM, has been used by choosing the Dirac delta function as a particle characteristic function $\chi_{mp}(x)$ (Sulsky *et al.*, 1994). Figure 2.3 gives the basic shape function $N_i(x)$ and its gradient $\nabla N_i(x)$ for standard MPM in the 1D case. Note that this shape function is typically C^0 continuous, which leads to a discontinuous gradient at a given node (for example at node i shown in Figure 2.3b). This discontinuity in the shape function gradient can cause the so-called cell crossing issue (Bardenhagen & Kober, 2004) as MPs move from one cell to another. As a consequence, this cell crossing issue can lead to huge oscillation in the internal force calculation, which was recently studied by González Acosta (2020).

To remedy the cell crossing issue, Bardenhagen & Kober (2004) proposed the Generalized Interpolation Material Point (GIMP) Method by choosing a particle characteristic

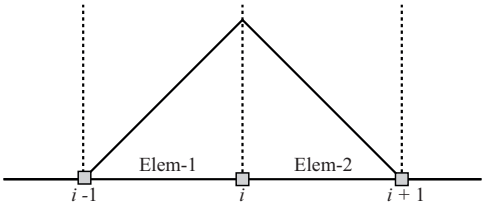

(a) MPM shape function $N_i(x)$

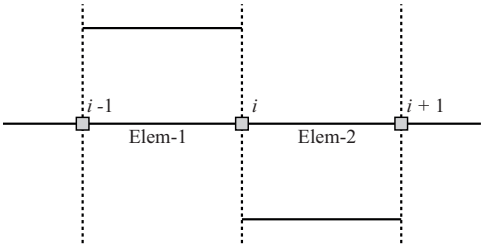

(b) MPM shape function gradient $\nabla N_i(x)$

Figure 2.3: Standard MPM shape function $N_i(x)$ and its gradient $\nabla N_i(x)$ in 1D case

function (of finite extent), which defines contiguous MPs and a step function as follows:

$$\chi_{mp}(x) = \begin{cases} 1, & \text{if } x \in \Omega_{mp} \\ 0, & \text{otherwise} \end{cases} \tag{2.1}$$

where χ_{mp} is the "particle characteristic function", and Ω_{mp} is the support domain of the MP and assumed to be of size $2l_p$ in each dimension. The values of $2l_p$ can be computed by dividing the grid cell size by the initial number of MPs along the considered direction.

Following this algorithm, the GIMP shape function is constructed by integrating linear FEM shape functions $N_i(x)$ over the MP support domain Ω_p (as shown in Figure 2.4). In one dimension, the GIMP shape function $S_{i,mp}$ and its gradient $\nabla S_{i,mp}$ are calculated as

$$S_{i,mp} = \frac{1}{V_{mp}} \int_{\Omega_{mp} \cap \Omega} \chi_{mp}(x) N_i(x) dx \tag{2.2}$$

$$\nabla S_{i,mp} = \frac{1}{V_{mp}} \int_{\Omega_{mp} \cap \Omega} \chi_{mp}(x) \nabla N_i(x) dx \tag{2.3}$$

over the problem domain Ω, where subscripts i and mp denote the i^{th} grid node and mp^{th} MP, respectively. Figure 2.4 explicitly displays the GIMP shape function $S_{i,mp}(x)$ and its gradient $\nabla S_{i,mp}(x)$ in the 1D case. More specific equations and details are given in Bardenhagen & Kober (2004) and are therefore not included in this thesis.

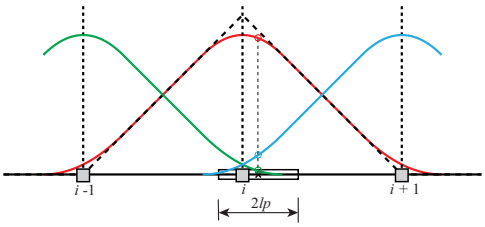

(a) GIMP shape function $S_{i,mp}(x)$

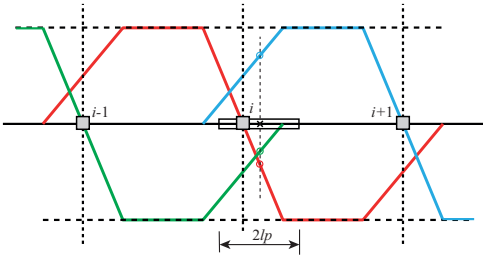

(b) GIMP shape function gradient $\nabla S_{i,mp}(x)$

Figure 2.4: GIMP shape function $S_{i,mp}(x)$ and its gradient $\nabla S_{i,mp}(x)$ in the 1D case

As illustrated in Figure 2.4b, the gradient of the GIMP shape function is C^1 continuous, i.e., without discontinuity even at the cell edges. This gradual change in the shape function gradient is found to greatly alleviate the cell crossing error and improve the numerical performance of MPM (Sulsky *et al.*, 1994). Note that, for the GIMP, it is assumed that the MP support domain in 2D problems always remains as a rectangle and aligns with the grid even for large deformation problems. However, this assumption is not always the case, particularly for problem domains that undergo extremely large shear deformations or large rotations. For the former case, the support domain of the MP may not remain as a rectangle but become a quadrilateral during the shear deformation; whereas the MP support domain can become misaligned with the background grid for the latter case. This specific type of MP support domain may lead to the GIMP suffering from low accuracy under extremely large deformation patterns.

To address the limitation of the GIMP for simulating problems with large shear deformation or rotation, Sadeghirad *et al.* (2011, 2013) proposed the convected particle domain interpolation (CPDI) method, including the CPDI1 and CPDI2. In CPDI1 the MP support domains are tracked as parallelograms in 2D analyses. As an enhanced extension of CPDI1, the MP support domains in CPDI2 are tracked as quadrilaterals in the 2D case. The CPDI2 is proven to remove the overlaps and gaps between the MP support domains, and to be more accurate and efficient. As an example, only the MP support domain updating scheme in CPDI2 is shown in Figure 2.5. More details about CPDI1 and CPDI2 can be found in Sadeghirad *et al.* (2011, 2013) and Nguyen *et al.* (2017).

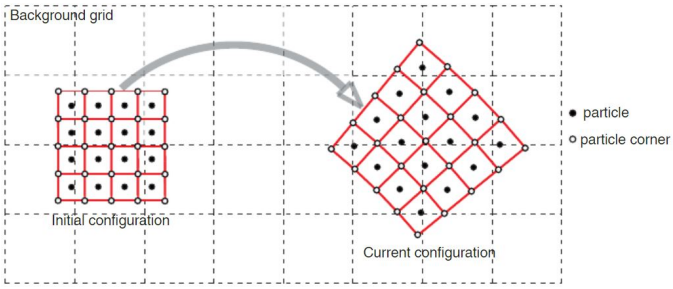

Figure 2.5: MP support domain updating scheme (as linear quadrilaterals) in CPDI2 (Sadeghirad *et al.*, 2013)

Another available method to solve the cell crossing issue is the combination of MPM with B-splines basis functions, which is known as BSMPM (Steffen *et al.*, 2008). This method has been further studied by other researchers (Stomakhin *et al.*, 2014; Tielen *et al.*, 2017; Gan *et al.*, 2018; Bing *et al.*, 2019). Figure 2.6 shows the B-spline shape functions with modified boundary adopted in Steffen *et al.* (2008). Similar to the shape functions of GIMP, these B-spline shape functions are at least C^1 continuous and have proven to significantly reduce the typical cell crossing error that exists in the standard MPM.

Instead of constructing a new basic shape function, Zhang *et al.* (2011) proposed the dual domain material point (DDMP) method by using identical shape functions as in standard MPM $N_i(x)$ (as shown in Figure 2.3a), but replacing the stepped shape function gradient ∇S with a modified $\overline{\nabla S}$ (DDMP) (as shown in Figure 2.7). Figure 2.7 gives the comparison between the shape function gradient of the DDMP, standard MPM, and GIMP

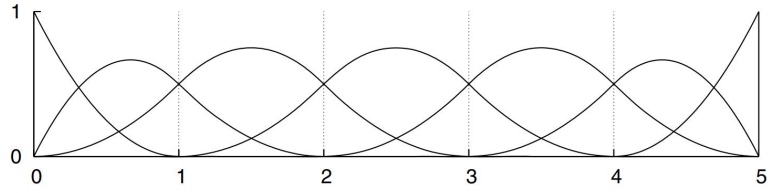

(a) Quadratic B-Spine ($k = 3$)

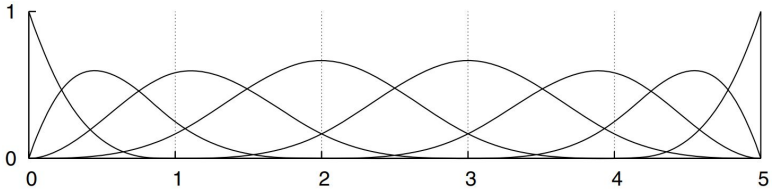

(b) Cubic B-Spine ($k = 4$)

Figure 2.6: B-spline shape functions with modified boundary in 1D case adopted in Steffen *et al.* (2008)

methods. The modified shape function gradient uses an enlarged influence domain relative to the standard MPM and is proven to significantly improve the cell crossing error.

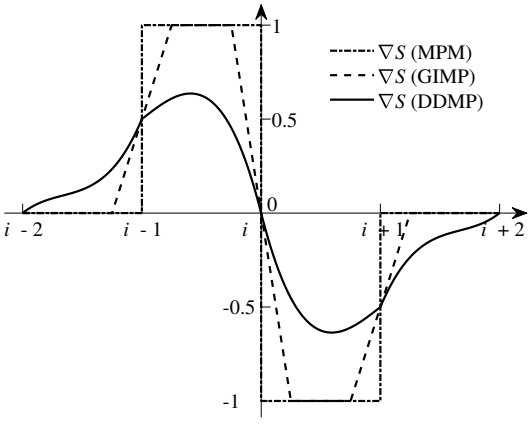

Figure 2.7: Comparison between shape function gradients of DDMP, standard MPM, and GIMP methods

Apart from the above mentioned MPM advances, several other improvements, such as weighted least squares MPM (Wallstedt & Guilkey, 2011), Moving Least Square MPM (Edwards & Bridson, 2012), and improved MPM (Sulsky & Gong, 2016) have been proposed in order to improve both the accuracy and convergence of MPM.

Low-order shape functions are often preferred in MPM, so as to avoid the numerical divergence possibly caused by the negative parts of higher-order polynomial shape functions. The shape functions play an especially important role in MPM, as quadrature takes place directly using the material point locations and often grid cells are only partially

filled, so material points far away from the node (which usually take the negative part of the shape function) can strongly influence the quadrature. Alternatively, the use of higher-order interpolation functions, such as B-spline functions, which do not have the negative parts that polynomial interpolation functions have, have also been considered. However, 2D and 3D implementations using B-spline functions have not been well developed; meanwhile, the use of B-spline functions can lead to a significant increase in computational costs, especially for two-phase coupled large deformation problems. For this reason, this thesis focuses on the improvement of low-order coupled GIMP.

2.3. HYDRO-MECHANICAL COUPLED ANALYSIS USING MPM

2.3.1. TWO-PHASE COUPLED FORMULATIONS

In what follows, soil-like fully saturated porous media are considered. The density of the soil–water mixture ρ is obtained from the individual phase densities as $\rho = (1-n)\,\rho_s + n\rho_w$, where subscripts w and s respectively denote water and soil phases, and n is the volume porosity. Based on the well-established effective stress principle, the behaviour of the solid skeleton is assumed to be governed by the effective stress $\boldsymbol{\sigma}'$, defined, in vector notation, as $\boldsymbol{\sigma}' = \boldsymbol{\sigma} + \boldsymbol{m}p$, where $\boldsymbol{\sigma}$ is the total stress, p is the pore water pressure, and $\boldsymbol{m}$ is the vector representation of the Kronecker tensor. Bold symbols indicate matrices and vectors; positive values are used for tensile total/effective stress components and compressive pore pressures.

Following the previous work of Zienkiewicz and co-workers (Zienkiewicz *et al.*, 1980, 1999), when modeling fully coupled hydro-mechanical problems, three main types of formulation can be identified according to different adopted unknowns. The formulations that govern the motion of a fully saturated porous medium are written as follows:

1. Three-field u–w–p form

$$\mathbf{S}^{\mathrm{T}}\boldsymbol{\sigma} - \rho\ddot{\boldsymbol{u}} - \rho_w\left(\dot{\boldsymbol{w}} + \boldsymbol{w}\nabla^{\mathrm{T}}\boldsymbol{w}\right) + \rho\boldsymbol{b} = \mathbf{0} \tag{2.4}$$

$$-\nabla p - \boldsymbol{R} - \rho_w\ddot{\boldsymbol{u}} - \rho_w\left(\dot{\boldsymbol{w}} + \boldsymbol{w}\nabla^{\mathrm{T}}\boldsymbol{w}\right)/n + \rho_w\boldsymbol{b} = \mathbf{0} \tag{2.5}$$

$$\nabla^{\mathrm{T}}\boldsymbol{w} + \boldsymbol{m}\dot{\varepsilon} + \frac{\dot{p}}{Q} + n\frac{\dot{\rho}_w}{\rho_w} + \dot{s}_0 = 0 \tag{2.6}$$

   where $\mathbf{S}$ is a differential divergence operator, $\boldsymbol{u}$ is the absolute displacement of the soil skeleton, $\boldsymbol{w}$ is the average (Darcy) velocity of the water phase relative to the solid phase, $\boldsymbol{b}$ is an external body force, $\boldsymbol{R}$ is the drag force exchanged by the soil skeleton and the pore water due to their relative motions, dots are used to indicate time differentiation, $\dot{\varepsilon}$ is the rate of strain, Q is a stiffness parameter defined as $1/Q = n/K_w + (1-n)/K_s$, K_w and K_s are the bulk moduli of the water phase and soil particles, respectively, and $\dot{s}_0$ is the rate of soil volume expansion due to thermal changes.

2. Two-field u–p form

   When neglecting the apparently small terms in the three-field formulation, namely the relative water acceleration $\dot{\boldsymbol{w}}$ and the associated convective term $\boldsymbol{w}\nabla^{\mathrm{T}}\boldsymbol{w}$ in the

governing equations, the governing equations become the simplified two-field u–p form:

$$\mathbf{S}^{\mathrm{T}}\boldsymbol{\sigma} - \rho\ddot{\boldsymbol{u}} + \rho\boldsymbol{b} = \mathbf{0} \tag{2.7}$$

$$\nabla^{\mathrm{T}}\boldsymbol{k}\left(-\nabla p - \rho_w\ddot{\boldsymbol{u}} + \rho_w\boldsymbol{b}\right) + \boldsymbol{m}\dot{\varepsilon} + \frac{\dot{p}}{Q} + n\frac{\dot{\rho}_w}{\rho_w} + \dot{s}_0 = 0 \tag{2.8}$$

where $\boldsymbol{k}$ is the permeability of the soil and its relationship with the drag force $\boldsymbol{R}$ is defined by $\boldsymbol{kR} = \boldsymbol{w}$.

3. Two-phase u–U form

   When neglecting only the convective term in the governing equation of the three-field formulation and using the total displacement U to define the motion of the water phase, the three-field formulation reduces to the two-phase u–U form, which is written as:

$$\mathbf{S}^{\mathrm{T}}\boldsymbol{\sigma} + Q(1-n)\nabla\left(\nabla^{\mathrm{T}}\boldsymbol{u}\right) + Qn\nabla\left(\nabla^{\mathrm{T}}\boldsymbol{U}\right) - (1-n)\rho\ddot{\boldsymbol{u}} - \rho_w n\ddot{\boldsymbol{U}} + \rho\boldsymbol{b} = \mathbf{0} \tag{2.9}$$

$$(1-n)Q\nabla\left(\nabla^{\mathrm{T}}\boldsymbol{u}\right) + nQ\nabla\left(\nabla^{\mathrm{T}}\boldsymbol{U}\right) - n\boldsymbol{k}^{-1}(\boldsymbol{U}-\boldsymbol{u}) - \rho_w\boldsymbol{U} + \rho_w\boldsymbol{b} = \mathbf{0} \tag{2.10}$$

   In the above equations, the total water displacement $\boldsymbol{U}$ is defined by $\boldsymbol{U} = \boldsymbol{u} + \boldsymbol{u}^r$, where $\boldsymbol{u}^r$ is the displacement of the water phase relative to the solid phase with $\dot{\boldsymbol{u}}^r = \boldsymbol{w}/n$.

For a better comparison, Table 2.1 summarises the basic unknowns and treatment regarding the relative water acceleration for three main types of governing equations in water-saturated porous media. Only a very simple introduction to these three formulations are provided here. More details can be found in Zienkiewicz *et al.* (1980, 1999), and the adopted coupled formulations within the framework of MPM are also briefly discussed in the following chapters for the completeness of description.

Table 2.1: Overview of three main types of coupled governing equations in water-saturated porous media

Governing equations	Basic unknowns			Relative water acceleration terms	
				$\dot{\boldsymbol{w}}$	$\boldsymbol{w}\nabla^{\mathrm{T}}\boldsymbol{w}$
Three-field u–w–p form	u	w	p	Included	Included
Two-field u–p form	u	–	p	Neglected	Neglected
Two-field u–U form	u	U	–	Included	Neglected

2.3.2. COUPLED NUMERICAL IMPLEMENTATION USING MPM

In common with FEM poromechanical formulations (Zienkiewicz *et al.*, 1980, 1999), recent developments in MPM formulations for coupled problems can be categorised with respect to: (i) different types of coupled formulation; (ii) different layers of MPs; (iii) different time integration algorithms.

- **Using different types of coupled formulation**

The MPM solution of dynamic two-phase problems has most often been tackled using one of two alternative mathematical formulations: (i) the u–p formulation, or (ii) the v–w formulation in which the velocities of the solid (v) and fluid (w) phases are considered (in essence equivalent to the u–U form described by Zienkiewicz *et al.* (1980, 1999)). The main difference between these two options lies in whether or not the relative acceleration of the fluid with respect to the solid is taken into account – in fact, the relative acceleration of the pore fluid is neglected in the u–p formulation. Although the u–p formulation is known to be inaccurate for fast dynamic phenomena, a number of coupled MPM implementations have been developed based on this approach (Zhang *et al.*, 2009; Higo *et al.*, 2010; Zabala & Alonso, 2011; Abe *et al.*, 2013; Zheng *et al.*, 2013; Higo *et al.*, 2015; Zhao & Choo, 2020) due to its simplicity in numerical implementation. Conversely, the accelerations of both the solid and fluid phases are exactly represented in formulations of the v–w type, which are therefore applicable to any dynamic regime. In the light of this consideration, several MPM implementations have been built on the v–w approach (Zhang *et al.*, 2007; Jassim *et al.*, 2013; Bandara & Soga, 2015; Soga *et al.*, 2015; Yerro *et al.*, 2015; Yerro, 2015; Ceccato *et al.*, 2016; Liu *et al.*, 2017; Yerro *et al.*, 2017; González Acosta *et al.*, 2019).

- **Using different layers of MPs**

In the context of coupled MPM, both single-layer and two-layer approaches have been explored, i.e., the use of one or two sets of material points (MPs) to describe the response of distinct phases (Soga *et al.*, 2015).

For the single-layer approach, as illustrated in Figure 2.8, each specific MP carries all information for both the soil and water phases. When using a single-layer of MPs, the position of an MP is updated following the movement of the solid phase. Even though this approach only guarantees mass conservation of the solid phase, the lower computational costs that are associated with the single-layer approach have motivated its most frequent use in previous coupled MPM research (Zhang *et al.*, 2009; Zabala & Alonso, 2011; Jassim *et al.*, 2013; Zheng *et al.*, 2013; Ceccato *et al.*, 2016; Lei *et al.*, 2020; Zhao & Choo, 2020).

Conversely, as illustrated in Figure 2.9, two sets of MPs, i.e., a soil layer and a water layer, have also been used in coupled MPM (Zhang *et al.*, 2007; Abe *et al.*, 2013; Bandara & Soga, 2015; Liu *et al.*, 2017; Tran & Sołowski, 2019; Kularathna *et al.*, 2021). In the two-layer approach, these two sets of MPs are respectively used for tracking the motion of the solid and water phases. As two sets of MPs are used, it can easily guarantee the mass conservation of both phases and capture the interaction between them. Nevertheless, the presence of two layers of MPs leads to a significant increase in computational costs, which limits the practical application of coupled MPM especially for large deformation analyses in nearly or fully incompressible materials. Furthermore, special treatments are required for modeling interface regions (i.e., the interface between free water and soil–water mixture) in the two-layer approach (Soga *et al.*, 2015).

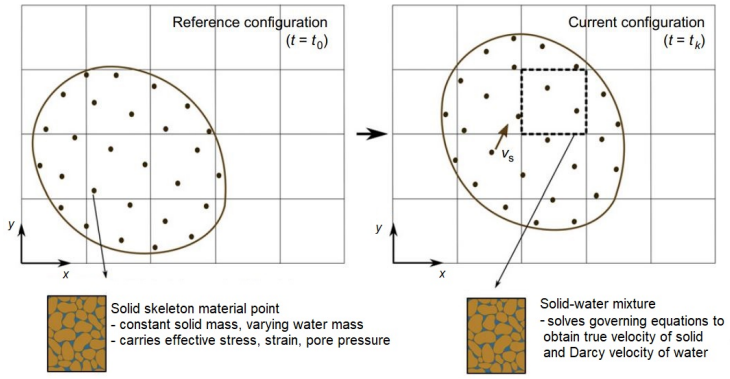

Figure 2.8: Coupled MPM implementation using single set of MPs to describe the response of both phases (Soga *et al.*, 2015)

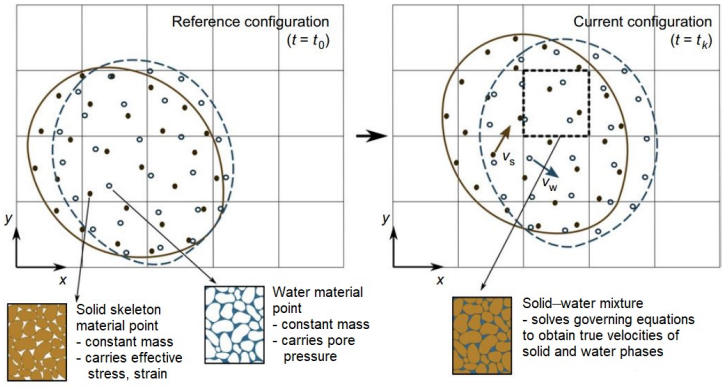

Figure 2.9: Coupled MPM implementation using two sets of MPs to describe the response of both phases (Soga *et al.*, 2015)

- **Using different time integration algorithms**

For coupled MPM, the time integration algorithm is also a key factor for large deformation analysis, as it can affect both the overall stability and efficiency of the numerical scheme. However, most previous implementations of the coupled MPM have so far been developed using explicit, conditionally stable time integration (Zhang *et al.*, 2007, 2009; Zabala & Alonso, 2011; Abe *et al.*, 2013; Jassim *et al.*, 2013; Zheng *et al.*, 2013; Bandara & Soga, 2015; Ceccato *et al.*, 2016; Liu *et al.*, 2017; Tran & Sołowski, 2019; Lei *et al.*, 2020). To allow the use of larger time steps and more convenient stability properties, semi-implicit (Kularathna *et al.*, 2021) and fully implicit (Zhao & Choo, 2020) MPMs have recently begun to emerge in the literature.

For a better overview, Table 2.2 shows a brief summary of coupled MPM formulations for fully saturated porous media.

Table 2.2: Overview of existing MPM formulations for large-deformation problems in fully saturated porous media

Reference	Formulation	MP layering	Time integration algorithm
Zhang *et al.* (2007)	u–U form	Two-layers	Explicit
Zhang *et al.* (2009)	u–p form	Single-layer	Explicit
Zabala & Alonso (2011)	u–p form	Single-layer	Explicit
Abe *et al.* (2013)	u–p form	Two-layers	Explicit
Jassim *et al.* (2013)	v–w form	Single-layer	Explicit
Zheng *et al.* (2013)	u–p form	Single-layer	Explicit
Bandara & Soga (2015)	v–w form	Two-layers	Explicit
Ceccato *et al.* (2016)	v–w form	Single-layer	Explicit
Liu *et al.* (2017)	v–w form	Two-layers	Explicit
Wang *et al.* (2018)	v–w form	Single-layers	Explicit
Tran & Sołowski (2019)	v–w form	Two-layers	Explicit
Lei *et al.* (2020)	v–w form	Single-layer	Explicit
Zhao & Choo (2020)	u–p form	Single-layer	Implicit
Kularathna *et al.* (2021)	u–U form	Single-layer	Semi-implicit

2.3.3. NUMERICAL INCOMPRESSIBILITY CONSTRAINTS IN COUPLED MPM

Similarly to the case of coupled Finite Element Methods (FEMs), also MPMs perform poorly in the presence of incompressibility constraints when built on low-order spatial interpolation. With regard to fluid-saturated geomaterials, incompressible behaviour may be associated with hindered pore water drainage and/or an isochoric (or nearly isochoric) response of the solid skeleton (Bandara & Soga, 2015): while the former may introduce well-known instabilities in the simulated pore pressure field, the latter may give rise to an excessively stiff response of the system (volumetric locking) – it is worth recalling that constitutive models for geomaterials produce only limited volumetric strain increments when substantial plasticity is mobilised. However, most existing literature on coupled MPM formulations concerns two-phase materials with compressible components. By considering water to be more compressible, spurious oscillations can be reduced. In addition, unsaturated conditions (such as in Wang *et al.* (2018)) are implicitly much more compressible, and therefore result in less oscillations. Nonetheless, a large number of previous studies have not explicitly mentioned the (near) incompressbility induced oscillations, and only a few of them have dealt with the (near) incompressbility in coupled MPM.

To suppress pore pressure instabilities in low-order coupled MPMs, several stabilisation approaches have been proposed, including fractional time stepping (Kularathna *et al.*, 2021), polynomial pressure projection (Zhao & Choo, 2020), and reduced integration (Abe *et al.*, 2013; Bandara & Soga, 2015; Wang *et al.*, 2018), and volumetric strain averaging (Jassim *et al.*, 2013; Ceccato *et al.*, 2016; Lei *et al.*, 2020). On the other hand, locking-related inaccuracies can be mitigated in two-phase coupled problems by means of techniques initially developed for one-phase media. In the context of one-phase MPM modelling, solutions based, e.g., on mixed variational principles (Mast *et al.*, 2012; Iaconeta *et al.*,

2019), fractional time stepping (Kularathna & Soga, 2017; Zhang *et al.*, 2017), and $\overline{\text{F}}$ and $\overline{\text{B}}$ methods (Coombs *et al.*, 2018; Bisht *et al.*, 2021) have already proven successful against locking in one-phase large-deformation problems. In very few instances, such locking remedies have also been implemented in coupled (standard) MPMs (Jassim *et al.*, 2013; Bandara & Soga, 2015), but exclusively in combination with explicit time integration. Most recently, Kularathna *et al.* (2021) proposed a stable time-stepping scheme for the MPM modelling of fluid-saturated porous media within the framework of the GIMP.

2.4. CONCLUDING REMARKS

VARIOUS studies using MPM have been performed in previous research to study the hydro-mechanical behaviour of large deformation problems in two-phase porous media such as soils. Most of these studies have been carried out using explicit time integration (conditionally stable) or considering a compressible porous medium (without explicitly stating the algorithm for dealing with the incompressibility constraints). A brief review of coupled analysis using MPM is summarised as follows:

- MPM has shown a promising capacity for modeling large deformation processes in the geotecinical field, owing to its significant advantages in large deformation simulation. Different advances have been reported, such as GIMP, CPDI, DDMP, BSMPM, and so on, with the aim of improving the performance and accuracy of standard MPM, and some of them have been implemented for two-phase coupled analysis.

- Low-order MPMs are often preferred and investigated in large deformation analysis, especially in fully saturated coupled analysis due to its simplicity in implementation and lower computational cost. In addition, most recent coupled MPM studies have been performed based on the v–w formulation, which includes soil–water relative acceleration terms, to address dynamic applications.

- MPM performs poorly in the presence of incompressibility constraints when built on low-order spatial interpolation (such as in standard MPM and GIMP). These incompressibility constraints can lead to pore pressure instabilities and an over-stiff response of the soil skeleton in fluid-saturated soils. Limited coupled MPM studies have been reported to fully address the numerical issues caused by incompressibility constraints.

- Most currently available MPM developments for coupled problems still build on explicit time integration, which is conditionally stable and subjected to extremely small time steps to fulfill stability conditions for nearly or fully incompressible materials.

REFERENCES

Abe, K., Soga, K. & Bandara, S. (2013). Material point method for coupled hydromechanical problems. *Journal of Geotechnical and Geoenvironmental Engineering* **140**, No. 3, 04013033.

Bandara, S. & Soga, K. (2015). Coupling of soil deformation and pore fluid flow using material point method. *Computers and Geotechnics* **63**, 199–214.

Bardenhagen, S. G. & Kober, E. M. (2004). The generalized interpolation material point method. *Computer Modeling in Engineering and Sciences* **5**, No. 6, 477–496.

Bing, Y., Cortis, M., Charlton, T., Coombs, W. & Augarde, C. (2019). B-spline based boundary conditions in the material point method. *Computers & Structures* **212**, 257–274.

Bisht, V., Salgado, R. & Prezzi, M. (2021). Simulating penetration problems in incompressible materials using the material point method. *Computers and Geotechnics* **133**, 103593.

Brackbill, J. U., Kothe, D. B. & Ruppel, H. M. (1988). FLIP: a low-dissipation, particle-in-cell method for fluid flow. *Computer Physics Communications* **48**, No. 1, 25–38.

Brackbill, J. U. & Ruppel, H. M. (1986). FLIP: A method for adaptively zoned, particle-in-cell calculations of fluid flows in two dimensions. *Journal of Computational Physics* **65**, No. 2, 314–343.

Ceccato, F., Beuth, L., Vermeer, P. A. & Simonini, P. (2016). Two-phase material point method applied to the study of cone penetration. *Computers and Geotechnics* **80**, 440–452.

Coombs, W. M., Charlton, T. J., Cortis, M. & Augarde, C. E. (2018). Overcoming volumetric locking in material point methods. *Computer Methods in Applied Mechanics and Engineering* **333**, 1–21.

Edwards, E. & Bridson, R. (2012). A high-order accurate particle-in-cell method. *International Journal for Numerical Methods in Engineering* **90**, No. 9, 1073–1088.

Gan, Y., Sun, Z., Chen, Z., Zhang, X. & Liu, Y. (2018). Enhancement of the material point method using b-spline basis functions. *International Journal for Numerical Methods in engineering* **113**, No. 3, 411–431.

González Acosta, L. J. (2020). *Investigation of mpm inaccuracies, contact simulation and robust implementation for geotechnical problems*. Ph.D. thesis, Delft University of Technology.

González Acosta, L. J., Zheng, X. C., Vardon, P. J., Hicks, M. A. & Pisanó, F. (2019). On stress oscillation in MPM simulations involving one or two phases. In *MPM 2019: 2nd International Conference on the Material Point Method for Modelling Soil–Water–Structure Interaction*.

Harlow, F. H. (1964). The particle-in-cell computing method for fluid dynamics. *Methods in Computational Physics* **3**, 319–343.

Higo, Y., Nishimura, D. & Oka, F. (2015). Dynamic analysis of unsaturated embankment considering the seepage flow by a GIMP-FDM coupled method. In *Computer Methods and Recent Advances in Geomechanics: Proceedings of the 14th International Conference of International Association for Computer Methods and Recent Advances in Geomechanics, 2014 (IACMAG 2014)*, Taylor & Francis Books Ltd, pp. 1761–1766.

Higo, Y., Oka, F., Kimoto, S., Morinaka, Y., Goto, Y. & Chen, Z. (2010). A coupled MPM-FDM analysis method for multi-phase elasto-plastic soils. *Soils and Foundations* **50**, No. 4, 515–532.

Iaconeta, I., Larese, A., Rossi, R. & Oñate, E. (2019). A stabilized mixed implicit material point method for non-linear incompressible solid mechanics. *Computational Mechanics* **63**, No. 6, 1243–1260.

Jassim, I., Stolle, D. & Vermeer, P. (2013). Two-phase dynamic analysis by material point method. *International Journal for Numerical and Analytical Methods in Geomechanics* **37**, No. 15, 2502–2522.

Kularathna, S., Liang, W., Zhao, T., Chandra, B., Zhao, J. & Soga, K. (2021). A semi-implicit material point method based on fractional-step method for saturated soil. *International Journal for Numerical and Analytical Methods in Geomechanics* .

Kularathna, S. & Soga, K. (2017). Implicit formulation of material point method for analysis of incompressible materials. *Computer Methods in Applied Mechanics and Engineering* **313**, 673–686.

Lei, X., He, S. & Wu, L. (2020). Stabilized generalized interpolation material point method for coupled hydro-mechanical problems. *Computational Particle Mechanics* , 1–20.

Liu, C. Q., Sun, Q. C., Jin, F. & Zhou, G. G. (2017). A fully coupled hydro-mechanical material point method for saturated dense granular materials. *Powder Technology* **314**, 110–120.

Mast, C., Mackenzie-Helnwein, P., Arduino, P., Miller, G. R. & Shin, W. (2012). Mitigating kinematic locking in the material point method. *Journal of Computational Physics* **231**, No. 16, 5351–5373.

Nguyen, V. P., Nguyen, C. T., Rabczuk, T. & Natarajan, S. (2017). On a family of convected particle domain interpolations in the material point method. *Finite Elements in Analysis and Design* **126**, 50–64.

Sadeghirad, A., Brannon, R. M. & Burghardt, J. (2011). A convected particle domain interpolation technique to extend applicability of the material point method for problems involving massive deformations. *International Journal for Numerical Methods in Engineering* **86**, No. 12, 1435–1456.

Sadeghirad, A., Brannon, R. M. & Guilkey, J. (2013). Second-order convected particle domain interpolation (CPDI2) with enrichment for weak discontinuities at material interfaces. *International Journal for Numerical Methods in Engineering* **95**, No. 11, 928–952.

Soga, K., Alonso, E., Yerro, A., Kumar, K. & Bandara, S. (2015). Trends in large-deformation analysis of landslide mass movements with particular emphasis on the material point method. *Géotechnique* **66**, No. 3, 248–273.

Soga, K., Alonso, E., Yerro, A., Kumar, K. & Bandara, S. (2016). Trends in large-deformation analysis of landslide mass movements with particular emphasis on the material point method. *Géotechnique* **66**, No. 3, 248–273.

Steffen, M., Wallstedt, P., Guilkey, J., Kirby, R. & Berzins, M. (2008). Examination and analysis of implementation choices within the material point method (MPM). *Computer Modeling in Engineering and Sciences* **31**, No. 2, 107–127.

Stomakhin, A., Schroeder, C., Jiang, C., Chai, L., Teran, J. & Selle, A. (2014). Augmented mpm for phase-change and varied materials. *ACM Transactions on Graphics (TOG)* **33**, No. 4, 1–11.

Sulsky, D., Chen, Z. & Schreyer, H. L. (1994). A particle method for history-dependent materials. *Computer Methods in Applied Mechanics and Engineering* **118**, No. 1-2, 179–196.

Sulsky, D. & Gong, M. (2016). Improving the material-point method. In *Innovative Numerical Approaches for Multi-field and Multi-scale Problems*, Springer, pp. 217–240.

Sulsky, D. & Schreyer, H. L. (1996). Axisymmetric form of the material point method with applications to upsetting and taylor impact problems. *Computer Methods in Applied Mechanics and Engineering* **139**, No. 1-4, 409–429.

Tielen, R., Wobbes, E., Möller, M. & Beuth, L. (2017). A high order material point method. *Procedia Engineering* **175**, 265–272.

Tran, Q.-A. & Sołowski, W. (2019). Temporal and null-space filter for the material point method. *International Journal for Numerical Methods in Engineering* **120**, No. 3, 328–360.

Wallstedt, P. & Guilkey, J. (2011). A weighted least squares particle-in-cell method for solid mechanics. *International Journal for Numerical Methods in Engineering* **85**, No. 13, 1687–1704.

Wang, B. (2017). *Slope failure analysis using the material point method*. Ph.D. thesis, Delft University of Technology.

Wang, B., Vardon, P. J. & Hicks, M. A. (2018). Rainfall-induced slope collapse with coupled material point method. *Engineering Geology* **239**, 1–12.

Yerro, A. (2015). *MPM modelling of landslides in brittle and unsaturated soils*. Ph.D. thesis, Universitat Politècnica de Catalunya.

Yerro, A., Alonso, E. & Pinyol, N. (2015). The material point method for unsaturated soils. *Géotechnique* **65**, No. 3, 201–217.

Yerro, A., Rohe, A. & Soga, K. (2017). Modelling internal erosion with the material point method. *Procedia Engineering* **175**, 365–372.

Zabala, F. & Alonso, E. (2011). Progressive failure of aznalcóllar dam using the material point method. *Géotechnique* **61**, No. 9, 795–808.

Zhang, D. Z., Ma, X. & Giguere, P. T. (2011). Material point method enhanced by modified gradient of shape function. *Journal of Computational Physics* **230**, No. 16, 6379–6398.

Zhang, F., Zhang, X., Sze, K. Y., Lian, Y. & Liu, Y. (2017). Incompressible material point method for free surface flow. *Journal of Computational Physics* **330**, 92–110.

Zhang, H. W., Wang, K. P. & Chen, Z. (2009). Material point method for dynamic analysis of saturated porous media under external contact/impact of solid bodies. *Computer Methods in Applied Mechanics and Engineering* **198**, No. 17-20, 1456–1472.

Zhang, H. W., Wang, K. P. & Zhang, Z. (2007). Material point method for numerical simulation of failure phenomena in multiphase porous media. In *Computational Mechanics: International Symposium on Computational Mechanics*, Springer, pp. 36–47.

Zhao, Y. & Choo, J. (2020). Stabilized material point methods for coupled large deformation and fluid flow in porous materials. *Computer Methods in Applied Mechanics and Engineering* **362**, 112742.

Zheng, Y. G., Gao, F., Zhang, H. W. & Lu, M. K. (2013). Improved convected particle domain interpolation method for coupled dynamic analysis of fully saturated porous media involving large deformation. *Computer Methods in Applied Mechanics and Engineering* **257**, 150–163.

Zienkiewicz, O., Chang, C. & Bettess, P. (1980). Drained, undrained, consolidating and dynamic behaviour assumptions in soils. *Géotechnique* **30**, No. 4, 385–395.

Zienkiewicz, O. C., Chan, A., Pastor, M., Schrefler, B. & Shiomi, T. (1999). *Computational geomechanics*. Wiley: New York.

3

AN EXPLICIT STABILISED MPM FOR HYDROMECHANICAL PROBLEMS IN TWO-PHASE POROUS MEDIA

This chapter presents a single-point Material Point Method (MPM) for large deformation problems in two-phase porous media such as soils. Many MPM formulations are known to produce numerical oscillations and inaccuracies in the simulated results, largely due to numerical integration and stress recovery performed at non-ideal locations, cell crossing errors, and mass moving from one background grid cell to another. The same drawbacks lead to even worse consequences in the presence of an interstitial fluid phase, especially when undrained/incompressible conditions are approached. In this study, an explicit stabilised MPM, based on the Generalised Interpolation Material Point (GIMP) method with Selective Reduced Integration (SRI), is proposed to mitigate typical numerical oscillations in (nearly) incompressible coupled problems. It includes two additional features to improve stress and pore pressure recovery, namely (i) patch recovery of pore pressure increments based on a Moving Least Squares Approximation, and (ii) two-phase extension of the Composite Material Point Method for effective stress recovery. The combination of components leads to a new method named GC-SRI-patch. After a detailed description of the approach, its effectiveness is verified through analysing various consolidation problems, with emphasis on the representation of pore pressures in time and space.

Parts of this chapter have been published in Zheng *et al.* (2021).

3.1. INTRODUCTION

THE core of MPM relates to the use of a background mesh to solve (the discrete version of) the relevant governing equations, while MPs serve as quadrature points and can freely move within the domain set by the mesh, see e.g., Sulsky *et al.* (1994, 1995). Low-order shape functions are often preferred in MPM, so as to avoid the numerical divergence possibly caused by the negative parts of higher-order polynomial shape functions. These play an especially important role in MPM, as quadrature takes place directly using the material point locations and often grid cells are only partially filled, so material points far away from the node (which usually take the negative part of the shape function) can strongly influence the quadrature. When applied to coupled hydromechanical problems, however, low-order MPM may suffer from numerical instabilities, typically in the vicinity of the so-called undrained-incompressible limit. Unstable/inaccurate results will normally be obtained under such conditions, due to MPM's low-order interpolation functions violating well-known *inf-sup* requirements, in a way similar to that widely observed for finite element calculations (Brezzi & Bathe, 1990; Bathe, 2001). Alternatively, the use of higher-order interpolation functions, such as B-spline functions, which do not have the negative parts that polynomial interpolation functions have, has also been considered (Steffen *et al.*, 2008; Tielen *et al.*, 2017; Gan *et al.*, 2018; Tran *et al.*, 2019). However, resorting to higher-order interpolation directly leads to a larger number of material points (MPs) (Zhao & Choo, 2020) and 2D or 3D implementations have not been developed. For this reason, the present work focuses on the improvement of low-order, coupled MPM.

Most existing literature on coupled MPM formulations concerns two-phase materials with compressible components. By considering water to be more compressible, spurious oscillations can be reduced. In addition, unsaturated conditions (such as in Wang *et al.* (2018)) implicitly are much more compressible, and therefore result in less oscillations. Nonetheless, a few studies dealing with (nearly) incompressible problems and *inf-sup*-related instabilities have already been published. For example, a fractional time stepping method combined within an enhanced volumetric strain formulation was proposed in Jassim *et al.* (2013) to mitigate pathological locking and spurious oscillations in the pore pressure field. However, this time stepping method is not equally effective for all possible drainage conditions, nor straightforward to implement into existing coupled MPM codes. A stabilised implicit MPM has been recently developed by Zhao & Choo (2020), in which the mass balance equation is augmented with a stabilising term to make equal-order mixed interpolation stable under undrained conditions. Such a term is derived using polynomial pressure projection in a way specific to the adopted time integration algorithm.

In standard MPM, integration and recovery of strains, stresses and pore pressures always occurs at the MPs. Reducing the number of integration points, and fixing the location within individual grid cells (i.e. at so-called Gauss points as used in finite elements) can be used for stabilisation purposes. The idea of benefiting in coupled-MPM from reduced integration has been previously introduced, for instance, by Abe *et al.* (2013), Bandara & Soga (2015), and Wang *et al.* (2018). Accordingly, pore pressures are evaluated at the central Gauss points (GPs) of the background mesh (instead of at MPs), which has been found to alleviate the aforementioned pore pressure instabilities. Additionally, as reduced integration is exclusively performed to evaluate pore pressure variations, compu-

ted results appear not to suffer from spurious hourglass modes (Chen *et al.*, 2018). This approach can be readily implemented into existing explicit MPM codes and is further pursued in the present study.

It emerges from previous literature that pore pressures are most usually recovered from GPs to MPs by assuming uniform pore pressure increments within each grid cell of the background mesh. This determines the direct influence of grid cell size on MPM solutions, and can sometimes lead to pore pressure discontinuities (at inter-cell boundaries) and inaccuracies (at MPs). When MPs cross such grid cell edges, it can cause a sudden change in pore pressure at the MPs, and, as a consequence, spurious variations of nodal internal forces and stress oscillations, especially when a coarse background mesh is adopted. In this respect, some authors tested reduced integration in the Generalised Interpolation Material Point (GIMP) method (Bardenhagen & Kober, 2004) as a way to alleviate the stress oscillations related to cell-crossing (Abe *et al.*, 2013). More recently, GIMP has also been introduced in the implicit MPM to mitigate cell-crossing inaccuracies in two-phase problems built on the simplified $u-p$ formulation – see the aforementioned work (Zhao & Choo, 2020).

This chapter proposes an explicit stabilised MPM, named Generalised Interpolation Material Point method with Selective Reduced Integration, based on the patch recovery of pore pressure increments (GC-SRI-patch) and a complete dynamic formulation of the $v-w$ type. The GIMP method (Bardenhagen & Kober, 2004) contributes to reducing (stress) oscillations promoted by grid crossing errors. To avert spurious pore pressures, selective reduced integration (SRI) has also been introduced for pore pressure recovery at central GPs. Patch recovery based on a Moving Least Squares Approximation (MLSA) (similar to the moving least squares technique used in Tran *et al.* (2020) for improved moving least square shape function construction) is proposed to map calculated pore pressure increments from central GPs to MPs in order to increase the accuracy of the results. As for the evaluation of effective stresses, the same approach adopted in the recent (one-phase) Composite Material Point Method (CMPM) (González Acosta *et al.*, 2017) is herein extended to the proposed GC-SRI-patch to enhance stress recovery. This work is limited to elastic constitutive behaviour of the solid skeleton, and focuses on exploring the effectiveness of (the ingredients combined in) the proposed method. Further investigation is necessary to guarantee stable/accurate solutions in the presence of material plasticity (Coombs *et al.*, 2018), as well as to explain fundamentally why the GC-SRI-patch approach is beneficial against *inf-sup* related instabilities.

The content of the chapter is organised as follows. After providing the governing hydromechanical equations (Section 3.2), the technical details regarding the numerical formulation and implementation of the proposed GC-SRI-patch method are described in Section 3.3. Section 3.4 presents 1D/2D numerical examples for the verification of the proposed GC-SRI-patch method.

3.2. COUPLED FORMULATION FOR TWO-PHASE POROUS MEDIA

In line with most MPM literature, this work builds on a velocity formulation of the governing hydromechanical equations (Jassim *et al.*, 2013; Wang *et al.*, 2018; González Acosta *et al.*, 2019). In particular, a fully dynamic formulation is used, in which the total velocities of the soil skeleton and pore water, $\boldsymbol{v}_s$ and $\boldsymbol{v}_w$ respectively, are used as primary

variables. However, it should be noted that the relative discharge (Darcy) velocity $\boldsymbol{w}$ may be used in lieu of $\boldsymbol{v}_w$, as explained, e.g., by Zienkiewicz *et al.* (1999).

3.2.1. GOVERNING EQUATIONS

Momentum balance for the whole two-phase mixture is fulfilled if

$$\mathbf{S}^{\mathrm{T}}\boldsymbol{\sigma} - (1-n)\rho_s\dot{\boldsymbol{v}}_s - n\rho_w\dot{\boldsymbol{v}}_w + \rho\boldsymbol{b} = \mathbf{0} \tag{3.1}$$

where $\boldsymbol{S}$ is the differential operator defined for 2D problems (Zienkiewicz *et al.*, 1999):

$$\boldsymbol{S} = \begin{bmatrix} \frac{\partial}{\partial x} & 0 \\ 0 & \frac{\partial}{\partial y} \\ \frac{\partial}{\partial y} & \frac{\partial}{\partial x} \end{bmatrix} \tag{3.2}$$

while $\boldsymbol{v}_s$ and $\boldsymbol{v}_w$ are the total (true) velocities of the soil and pore water, respectively, $\boldsymbol{b}$ is a body acceleration term (e.g., gravity acceleration), and dots above symbols indicate time differentiation. It is also worth noting that the relative discharge velocity $\boldsymbol{w}$ may be obtained from the individual true velocities as $\boldsymbol{w} = n(\boldsymbol{v}_w - \boldsymbol{v}_s)$.

A similar equilibrium equation can be formulated for the water phase only:

$$-\nabla p_w - \boldsymbol{R} - \rho_w\dot{\boldsymbol{v}}_w + \rho_w\boldsymbol{b} = \mathbf{0} \tag{3.3}$$

where $\boldsymbol{R}$ represents the drag force exchanged by the solid and fluid phases during water seepage, which is proportional to the relative discharge velocity $\boldsymbol{w}$ according to Darcy's law:

$$\boldsymbol{R} = \frac{n\rho_w g}{k}(\boldsymbol{v}_w - \boldsymbol{v}_s) \tag{3.4}$$

where the hydraulic conductivity k is here assumed to be isotropic for simplicity, and g is the gravitational acceleration.

For mass balance, the following equations ensure the conservation of solid and water masses – under the assumptions of uniform densities and porosity, and incompressible soil grains:

$$\dot{n} = (1-n)\nabla\cdot\boldsymbol{v}_s \tag{3.5}$$

$$\rho_w\dot{n} + n\dot{\rho}_w + n\rho_w\nabla\cdot\boldsymbol{v}_w = 0 \tag{3.6}$$

Density variations in a barotropic fluid obey the following relationship:

$$\frac{\dot{\rho}_w}{\rho_w} = -\frac{\dot{p}_w}{K_w} \tag{3.7}$$

where K_w is the bulk modulus of the fluid. Substituting Eq. (3.5) into Eq. (3.6) and combining with Eq. (3.7) allows the pore pressure rate to be obtained:

$$\dot{p}_w = \frac{K_w}{n}\left[(1-n)\nabla\cdot\boldsymbol{v}_s + n\nabla\cdot\boldsymbol{v}_w\right] \tag{3.8}$$

The constitutive relationship between strain ($\dot{\boldsymbol{\varepsilon}}$) and effective stress ($\dot{\boldsymbol{\sigma}}'$) rates can be expressed as (Zienkiewicz *et al.*, 1999)

$$\dot{\boldsymbol{\sigma}}' = \boldsymbol{D}(\dot{\boldsymbol{\varepsilon}} - \dot{\boldsymbol{\varepsilon}}_0) \tag{3.9}$$

where $\boldsymbol{D}$ is the tangent stiffness matrix of the solid skeleton, and $\dot{\boldsymbol{\varepsilon}}_0$ is a strain rate term related to, e.g., thermal effects. Since emphasis is hereafter on the development and verification of the proposed GC-SRI-patch method, (i) isotropic linear elastic behaviour of the solid phase and (ii) linearised/infinitesimal definition of strain rates are exclusively considered. Fully general modelling of large deformations can be achieved by adopting well-established finite strain measures (Holzapfel, 2000), though with no expected detriment to the hydromechanical performance of the proposed method.

3.2.2. BOUNDARY AND INITIAL CONDITIONS

Considering a fully saturated porous domain Ω, its boundary surface Γ can be decomposed into subsurfaces on which Dirichlet and/or Neumann boundary conditions are imposed. Surface decomposition should be such that $\Gamma = \Gamma_u \cup \Gamma_\tau = \Gamma_p \cup \Gamma_w$ and $\Gamma_u \cap \Gamma_\tau = \Gamma_p \cap \Gamma_w = \emptyset$, so as to enable the enforcement of relevant conditions on the solid and water velocities:

$$\boldsymbol{v}_s(\boldsymbol{x},t) = \tilde{\boldsymbol{v}}_s(t) \quad \text{on} \quad \Gamma_u(t) \tag{3.10}$$

$$\boldsymbol{v}_w(\boldsymbol{x},t) = \tilde{\boldsymbol{v}}_w(t) \quad \text{on} \quad \Gamma_w(t) \tag{3.11}$$

as well as on the (total) surface traction and water pressure:

$$\boldsymbol{\sigma}(\boldsymbol{x},t)\cdot\boldsymbol{G} = \tilde{\boldsymbol{\tau}}(t) \quad \text{on} \quad \Gamma_\tau(t) \tag{3.12}$$

$$\boldsymbol{m}p_w(\boldsymbol{x},t)\cdot\boldsymbol{G} = \tilde{\boldsymbol{p}}_w(t) \quad \text{on} \quad \Gamma_p(t) \tag{3.13}$$

In Eqs. (3.12) – (3.13), $\boldsymbol{G}$ is a matrix containing components of the unit vector normal to the boundary surface Γ (Zienkiewicz *et al.*, 1999), while $\tilde{\boldsymbol{v}}_s(t)$, $\tilde{\boldsymbol{v}}_w(t)$, $\tilde{\boldsymbol{\tau}}(t)$ and $\tilde{\boldsymbol{p}}_w(t)$ are prescribed boundary values of the solid and water velocities, surface traction and pore pressure, respectively.

The full set of initial conditions are

$$\boldsymbol{v}_\alpha(\boldsymbol{x},0) = \boldsymbol{v}_{\alpha 0}(\boldsymbol{x}) \quad (\alpha = w,s) \tag{3.14}$$

$$\boldsymbol{\sigma}(\boldsymbol{x},0) = \boldsymbol{\sigma}_0(\boldsymbol{x}) \quad \text{and} \quad p_w(\boldsymbol{x},0) = p_{w0}(\boldsymbol{x}) \tag{3.15}$$

in which α equals s or w to indicate either the solid or water phase.

3.2.3. INTEGRAL WEAK FORMULATION

Standard manipulation of the governing equations and boundary conditions allows the following integral/weak version of the momentum balance equations, Eqs. (3.1) and (3.3), to be obtained (Zienkiewicz *et al.*, 1999):

$$\begin{aligned}\int_\Omega \delta\boldsymbol{v}^{\mathrm{T}}\cdot(\nabla\cdot\boldsymbol{\sigma})\mathrm{d}\Omega - \int_\Omega \delta\boldsymbol{v}^{\mathrm{T}}\cdot(1-n)\rho_s\dot{\boldsymbol{v}}_s\mathrm{d}\Omega - \\ \int_\Omega \delta\boldsymbol{v}^{\mathrm{T}}\cdot n\rho_w\dot{\boldsymbol{v}}_w\mathrm{d}\Omega + \int_\Omega \delta\boldsymbol{v}^{\mathrm{T}}\cdot\rho\boldsymbol{b}\mathrm{d}\Omega + \int_{\Gamma_\tau}\delta\boldsymbol{v}^{\mathrm{T}}\cdot\tilde{\boldsymbol{\tau}}\mathrm{d}\Gamma_\tau = 0\end{aligned} \tag{3.16}$$

$$\begin{aligned}-\int_\Omega \delta\boldsymbol{v}^{\mathrm{T}}\cdot\nabla p_w\mathrm{d}\Omega - \int_\Omega \delta\boldsymbol{v}^{\mathrm{T}}\cdot\frac{n\rho_w g}{k}(\boldsymbol{v}_w-\boldsymbol{v}_s)\mathrm{d}\Omega - \\ \int_\Omega \delta\boldsymbol{v}^{\mathrm{T}}\cdot\rho_w\dot{\boldsymbol{v}}_w\mathrm{d}\Omega + \int_\Omega \delta\boldsymbol{v}^{\mathrm{T}}\cdot\rho_w\boldsymbol{b}\mathrm{d}\Omega + \int_{\Gamma_p}\delta\boldsymbol{v}^{\mathrm{T}}\cdot\tilde{\boldsymbol{p}}_w\mathrm{d}\Gamma_p = 0\end{aligned} \tag{3.17}$$

where $\delta\boldsymbol{v}$ is a vector of suitable test functions.

3.3. THE GC-SRI-PATCH METHOD: FORMULATION AND IMPLEMENTATION

THIS section provides technical details regarding the formulation and implementation of the proposed GC-SRI-patch method. Emphasis is on the combined application of lessons learned from previous studies, with a view to mitigating the deficiencies of standard MPM with respect to cell crossing errors, pore pressure instabilities, and numerical quadrature and stress/pore pressure recovery performed at non-ideal locations.

3.3.1. SPATIAL DISCRETISATION

Primary unknowns in the adopted velocity formulation (Jassim *et al.*, 2013; González Acosta *et al.*, 2019) are the velocities of the solid ($\boldsymbol{v}_s$) and water ($\boldsymbol{v}_w$) phases. The same shape functions are used to approximate the velocities of both phases, as well as the test function vector $\delta\boldsymbol{v}$:

$$\boldsymbol{v}_\alpha = \boldsymbol{N}(\boldsymbol{x})\hat{\boldsymbol{v}}_\alpha \quad \delta\boldsymbol{v} = \boldsymbol{N}(\boldsymbol{x})\delta\hat{\boldsymbol{v}} \quad (\alpha = w, s) \tag{3.18}$$

where $\hat{\boldsymbol{v}}_\alpha$ and $\delta\hat{\boldsymbol{v}}$ define vectors of nodal values. In regular MPM, $\boldsymbol{N}(\boldsymbol{x})$ contains linear shape functions of the same kind as those used in FEM. It is known that regular MPM may suffer from stress oscillations when MPs cross grid cell boundaries due to discontinuous shape function gradients. GIMP was thus proposed (Bardenhagen & Kober, 2004) to alleviate such oscillations, with shape functions $S_i(x)$ constructed by integrating linear FEM shape functions $N_i(x)$ over the MP support domain Ω_p.

After substituting the approximation (Eq. (3.18)) using GIMP shape functions $\boldsymbol{S}(\boldsymbol{x})$ into Eqs. (3.16) and (3.17), the discrete versions of Eqs. (3.1) and (3.3) are:

$$\boldsymbol{M}_s\dot{\hat{\boldsymbol{v}}}_s = -\overline{\boldsymbol{M}}_w\dot{\hat{\boldsymbol{v}}}_w + \boldsymbol{F}_m^{trac} + \boldsymbol{F}_m^{body} - \boldsymbol{F}_m^{int} \tag{3.19}$$

$$\boldsymbol{M}_w\dot{\hat{\boldsymbol{v}}}_w = \boldsymbol{F}_w^{trac} + \boldsymbol{F}_w^{grav} - \boldsymbol{F}_w^{int} - \boldsymbol{F}_w^{drag} \tag{3.20}$$

where $\boldsymbol{M}_s$, $\boldsymbol{M}_w$, and $\overline{\boldsymbol{M}}_w$ are global nodal mass matrices which are diagonalised through "mass lumping- see, e.g., Kafaji (2013). In addition to s and w, the subscript m is used to denote "soil-water mixture". The superscripts $trac$, $body$, int, and $drag$ denote global force terms associated with surface tractions, body forces, internal forces and soil–water drag, respectively.

The global mass matrices in Eqs. (3.19) and (3.20) are obtained by assembling the following local mass matrices associated with individual grid cells:

$$\boldsymbol{m}_{w,i} = \sum_{mp=1}^{N_{mp}} \boldsymbol{S}_i^{\mathrm{T}}(\boldsymbol{x}_{mp}) m_{w,mp}\boldsymbol{S}_i(\boldsymbol{x}_{mp}) = \sum_{mp=1}^{N_{mp}} \boldsymbol{S}_i^{\mathrm{T}}(\boldsymbol{x}_{mp})\rho_{w,mp}V_{mp}\boldsymbol{S}_i(\boldsymbol{x}_{mp}) \tag{3.21}$$

$$\overline{\boldsymbol{m}}_{w,i} = \sum_{mp=1}^{N_{mp}} \boldsymbol{S}_i^{\mathrm{T}}(\boldsymbol{x}_{mp}) n_{mp} m_{w,mp}\boldsymbol{S}_i(\boldsymbol{x}_{mp}) \tag{3.22}$$

$$\boldsymbol{m}_{s,i} = \sum_{mp=1}^{N_{mp}} \boldsymbol{S}_i^{\mathrm{T}}(\boldsymbol{x}_{mp})(1-n_{mp}) m_{s,mp}\boldsymbol{S}_i(\boldsymbol{x}_{mp}) \tag{3.23}$$

where subscript i defines the i^{th} grid cell node, and N_{mp} is the number of MPs in the grid cell whose spatial coordinates, mass, volume, density and porosity are denoted by $\boldsymbol{x}_{mp}$, $m_{\alpha,mp}$, V_{mp}, $\rho_{\alpha,mp}$, and n_{mp}, respectively (with $\alpha = s, w$). The remaining force terms are obtained as follows:

$$\boldsymbol{F}^{trac}_{w,i} = \sum_{mp=1}^{N_{bmp}} \boldsymbol{S}_i^{\mathrm{T}}(\boldsymbol{x}_{mp})\boldsymbol{m}\tilde{p}_{w,bmp} \tag{3.24}$$

$$\boldsymbol{F}^{trac}_{m,i} = \sum_{mp=1}^{N_{bmp}} \boldsymbol{S}_i^{\mathrm{T}}(\boldsymbol{x}_{mp})\tilde{\boldsymbol{\tau}}_{m,bmp} \tag{3.25}$$

$$\boldsymbol{F}^{body}_{w,i} = \sum_{mp=1}^{N_{mp}} \boldsymbol{S}_i^{\mathrm{T}}(\boldsymbol{x}_{mp})m_{w,mp}\boldsymbol{b} \tag{3.26}$$

$$\boldsymbol{F}^{body}_{m,i} = \sum_{mp=1}^{N_{mp}} \boldsymbol{S}_i^{\mathrm{T}}(\boldsymbol{x}_{mp})m_{m,mp}\boldsymbol{b} \tag{3.27}$$

$$\boldsymbol{F}^{int}_{w,i} = \sum_{mp=1}^{N_{mp}} \nabla\boldsymbol{S}_i^{\mathrm{T}}(\boldsymbol{x}_{mp})\boldsymbol{m}\tilde{p}_{w,mp}V_{mp} = \sum_{mp=1}^{N_{mp}} \boldsymbol{B}_i^{\mathrm{T}}(\boldsymbol{x}_{mp})\boldsymbol{m}\tilde{p}_{w,mp}V_{mp} \tag{3.28}$$

$$\boldsymbol{F}^{int}_{m} = \sum_{p=1}^{N_{mp}} \nabla\boldsymbol{S}_i^{\mathrm{T}}(\boldsymbol{x}_{mp})\tilde{\boldsymbol{\sigma}}_{mp}V_{mp} = \sum_{p=1}^{N_{mp}} \boldsymbol{B}_i^{\mathrm{T}}(\boldsymbol{x}_{mp})\tilde{\boldsymbol{\sigma}}_{mp}V_{mp} \tag{3.29}$$

$$\boldsymbol{F}^{drag}_{w,i} = \sum_{mp=1}^{N_{mp}} \frac{n_{mp}m_{w,mp}g}{k}\boldsymbol{S}_i(\boldsymbol{x}_{mp})(\tilde{\boldsymbol{v}}_{w,mp} - \tilde{\boldsymbol{v}}_{s,mp}) \tag{3.30}$$

where N_{bmp} is the number of MPs near the domain boundary Γ on which the traction forces are applied. In Eqs. (3.24) – (3.30), $\tilde{p}_{w,bmp}$ and $\tilde{\boldsymbol{\tau}}_{m,bmp}$ are the prescribed pore pressure and traction force at MPs near the domain boundary, while $\tilde{p}_{w,mp}$, $\tilde{\boldsymbol{\sigma}}_{mp}$, $\tilde{\boldsymbol{v}}_{w,mp}$, and $\tilde{\boldsymbol{v}}_{s,mp}$ are the respective pore pressure, total stress, water velocity and solid skeleton velocity at the MP locations. $\boldsymbol{b}$ and $m_{m,mp} = \rho V_{mp}$ are the body forces and mass of the mixture at the MPs, while the compatibility matrices $\boldsymbol{B}_i(\boldsymbol{x}_{mp})$ contain derivatives of the shape functions in $\boldsymbol{S}_i(\boldsymbol{x}_{mp})$.

3.3.2. TIME DISCRETISATION

An explicit algorithm is adopted to integrate Eqs. (3.19) and (3.20) in time. Considering a generic time t, the accelerations of the water ($\dot{\hat{\boldsymbol{v}}}^t_{w,i}$) and solid ($\dot{\hat{\boldsymbol{v}}}^t_{s,i}$) phases at a node i can be straightforwardly obtained as

$$\dot{\hat{\boldsymbol{v}}}^t_{w,i} = (\boldsymbol{M}^t_{w,i})^{-1}[\boldsymbol{F}^{trac,t}_{w,i} + \boldsymbol{F}^{body,t}_{w,i} - \boldsymbol{F}^{int,t}_{w,i} - \boldsymbol{F}^{drag,t}_{w,i}] \tag{3.31}$$

$$\dot{\hat{\boldsymbol{v}}}^t_{s,i} = (\boldsymbol{M}^t_{s,i})^{-1}[-\overline{\boldsymbol{M}}^t_{w,i}\dot{\hat{\boldsymbol{v}}}^t_{w,i} + \boldsymbol{F}^{trac,t}_{m,i} + \boldsymbol{F}^{body,t}_{m,i} - \boldsymbol{F}^{int,t}_{m,i}] \tag{3.32}$$

owing to the diagonality of the above lumped mass matrices. The nodal accelerations are then used to update phase velocities over the time increment Δt at the MP locations:

$$\hat{\boldsymbol{v}}_{\alpha,mp}^{t+\Delta t} = \hat{\boldsymbol{v}}_{\alpha,mp}^{t} + \Delta t \sum_{i=1}^{N_n} S_i(\boldsymbol{x}_{mp}) \dot{\hat{\boldsymbol{v}}}_{\alpha,i}^{t} \quad (\alpha = w, s) \tag{3.33}$$

where N_n is the total number of nodes in the problem domain, and subscripts mp and i denote MPs and background mesh nodes, respectively. It should be noted that the same shape functions $S_i(\boldsymbol{x}_{mp})$ are used to map kinematic information from MPs to nodes in the background mesh and vice versa. After mapping the velocities at MPs $\hat{\boldsymbol{v}}_{\alpha,mp}^{t+\Delta t}$ to background nodes, the new nodal velocities $\hat{\boldsymbol{v}}_{\alpha,i}^{t+\Delta t}$ are updated as

$$\hat{\boldsymbol{v}}_{\alpha,i}^{t+\Delta t} = \frac{\sum_{mp=1}^{N_{mp}} S_i(\boldsymbol{x}_{mp}) m_{\alpha,mp} \hat{\boldsymbol{v}}_{\alpha,mp}^{t+\Delta t}}{m_{\alpha,i}} \quad (\alpha = w, s) \tag{3.34}$$

and the strain rates at MPs are evaluated as

$$\dot{\hat{\boldsymbol{\varepsilon}}}_{\alpha,mp}^{t} = \sum_{i=1}^{N_n} \boldsymbol{B}_i(\boldsymbol{x}_{mp}) \hat{\boldsymbol{v}}_{\alpha,i}^{t+\Delta t} \quad (\alpha = w, s) \tag{3.35}$$

where $\boldsymbol{B}_i(\boldsymbol{x}_{mp})$ is the shape function gradient. Finally, the strains, (effective) stresses, pore pressures and porosity values are updated as

$$\hat{\boldsymbol{\varepsilon}}_{\alpha,mp}^{t+\Delta t} = \hat{\boldsymbol{\varepsilon}}_{\alpha,mp}^{t} + \Delta t \dot{\hat{\boldsymbol{\varepsilon}}}_{\alpha,mp}^{t} \quad (\alpha = w, s) \tag{3.36}$$

$$\hat{\boldsymbol{\sigma}}'^{t+\Delta t}_{s,mp} = \hat{\boldsymbol{\sigma}}'^{t}_{s,mp} + \Delta t \boldsymbol{D} \dot{\hat{\boldsymbol{\varepsilon}}}_{s,mp}^{t} \tag{3.37}$$

$$\hat{p}_{w,mp}^{t+\Delta t} = \hat{p}_{w,mp}^{t} + \Delta t \frac{K_w}{n_{mp}} [(1 - n_{mp}) \mathrm{tr}(\dot{\hat{\boldsymbol{\varepsilon}}}_{s,mp}^{t}) + n_{mp} \mathrm{tr}(\dot{\hat{\boldsymbol{\varepsilon}}}_{w,mp}^{t})] \tag{3.38}$$

$$n_{mp}^{t+\Delta t} = 1 - \frac{1 - n_{mp}^{t}}{J(\boldsymbol{x}_{mp}, t + \Delta t)} \tag{3.39}$$

where J is the Jacobian of the deformation gradient tensor, i.e. $J(\boldsymbol{x}_{mp}, t+\Delta t) = 1+\mathrm{tr}(\hat{\boldsymbol{\varepsilon}}_{s,mp}^{t+\Delta t})$.

3.3.3. MITIGATING PORE PRESSURE INSTABILITIES IN MPM

Due to its apparent similarity to FEM, MPM suffers from *inf-sup*-related instabilities when low-order (linear) interpolation is adopted. This can also be the case for hydromechanical incompressible problems in porous media, giving rise to undesired oscillations in the pore pressure field (Belytschko *et al.*, 2013; Bathe, 2001; Chen *et al.*, 2018).

Currently, a number of techniques, such as multi-field variational principles, fractional step time integration, high-order interpolation and selective reduced integration are employed in FEM (Li *et al.*, 2003; Zienkiewicz *et al.*, 2005; Bathe, 2006; White & Borja, 2008; Belytschko *et al.*, 2013; McGann *et al.*, 2015; Pisanò & Pastor, 2011) in order to mitigate this type of pore pressure instability. These techniques may also be applied to MPM. Herein, the performance of the proposed method is improved by combining GIMP, which partially enhances the order of the interpolation, with Selective Reduced Integration (GIMP-SRI) of the pore pressures.

In its original conception (Bardenhagen & Kober, 2004), GIMP was used to integrate stresses in one-phase media, resulting in a significant improvement due to reduced cell-crossing errors. Nevertheless, in the two-phase case, large pore pressure oscillations

remain inside grid cells even using GIMP. Further benefits can be achieved by adopting reduced integration (GIMP-SRI) for pore pressure recovery, as illustrated in Figure 3.1. However, instead of directly calculating incremental pore pressures at MPs, reduced integration requires pore pressure increments to be computed at central integration GPs in each grid cell (e.g. GP1, GP2, GP3, and GP4 in Figure 3.1) as

$$\Delta p^t_{w,gp} = \Delta t \frac{K_w}{n^t_{gp}} \left[(1 - n^t_{gp}) \mathrm{tr}(\dot{\boldsymbol{\varepsilon}}^t_{s,gp}) + n_{gp} \mathrm{tr}(\dot{\boldsymbol{\varepsilon}}^t_{w,gp}) \right] \tag{3.40}$$

where $\dot{\boldsymbol{\varepsilon}}^t_{s,gp}$ and $\dot{\boldsymbol{\varepsilon}}^t_{w,gp}$ are volumetric strain rates of the solid/water phases, and n^t_{gp} is a weighted porosity. They are evaluated at the central GP position $\boldsymbol{x}_{gp}$ by

$$\dot{\boldsymbol{\varepsilon}}^t_{\alpha,gp} = \sum_{i=1}^{N_n} \boldsymbol{B}_i(\boldsymbol{x}_{gp}) \hat{\boldsymbol{v}}^{t+\Delta t}_{\alpha,i} \quad (\alpha = w, s) \tag{3.41}$$

and

$$n^t_{gp} = \frac{\sum_{mp=1}^{N_{mp}} n^t_{mp} V^t_{mp,e}}{\sum_{mp=1}^{N_{mp}} V^t_{mp,e}} \tag{3.42}$$

where $V^t_{mp,e}$ is the intersection volume between the MP support domain and the current grid cell where the considered GP is located. As reduced integration is only performed to evaluate pore pressure variations, computed results are found not to suffer from spurious hourglass modes (Chen *et al.*, 2018).

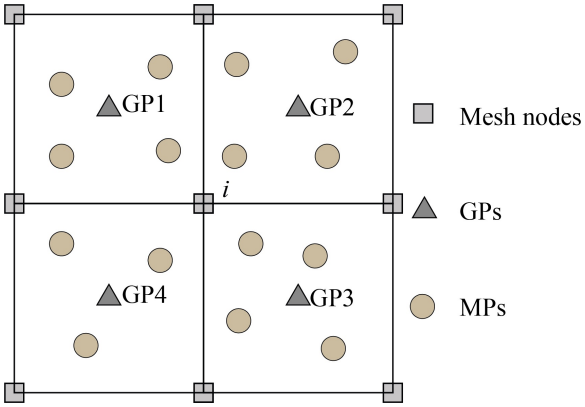

Figure 3.1: MPs and integration GPs in MPM

After obtaining incremental pore pressures through Eq. (4.22) at the central GPs, the key issue is to recover them back to the MPs. It is well-known that stresses calculated at the centre of low-order rectangular elements in FEM are of high accuracy and convergence order. As the calculation phase in MPM is a FEM calculation, with modified integration, it can be concluded that this also holds for an MPM grid cell. Following Zienkiewicz &

Zhu (1992a), it is here proposed to calculate the pore pressure increments at the MPs by so-called patch recovery based on a moving least squares approximation (MLSA). As shown in Figure 3.2, a patch of four quadrilateral cells can be identified for each internal node i. Within such a patch, a rectangular area can be delimited around the node by using the central GPs in the four grid cells. It is thus possible to introduce for the pore pressure increments (Δp_w) the following polynomial approximation of order p in the considered rectangular domain Ω_i (bounded by the red dashed lines in Figure 3.2):

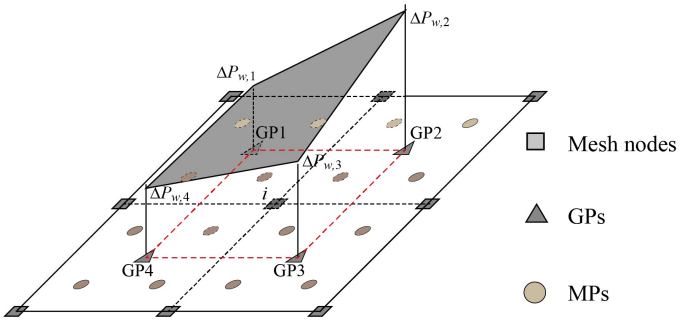

Figure 3.2: Patch recovery of pore pressure increments from GPs to MPs using MLSA

$$\Delta p_w(x,y) = \boldsymbol{Q}(x,y)\boldsymbol{a} \tag{3.43}$$

where (x,y) is the location of GPs in Ω_i, while $\boldsymbol{Q}$ and $\boldsymbol{a}$ are vectors containing polynomial shape functions and interpolation degrees-of-freedom. In general, different shape functions may be chosen to approximate the incremental pore pressure field. In this study, a linear version of $\boldsymbol{Q}(x_i,y_i) = [1 \; x_i \; y_i]$ is chosen, giving rise to the interpolation plane in Figure 3.2 after the determination of the coefficients in $\boldsymbol{a} = [a_0 \; a_1 \; a_2]^{\mathrm{T}}$. Based on a posteriori error estimator, the relative error at sampling GPs is calculated as

$$E(\boldsymbol{a}) = \sum_{i=1}^{N_{gp}} \left[\Delta p^t_{w,gp}(x_i,y_i) - \boldsymbol{Q}(x_i,y_i)\boldsymbol{a}\right]^2 \tag{3.44}$$

where N_{gp} is the total number of GPs in the approximation domain Ω_i, and (x_i,y_i) are the coordinates of the GPs. Minimising the error with respect to $\boldsymbol{a}$ leads to the following linear system:

$$\boldsymbol{A}\boldsymbol{a} = \boldsymbol{b} \tag{3.45}$$

where $\boldsymbol{A} = \sum_{i=1}^{N_{gp}} \boldsymbol{Q}^{\mathrm{T}}(x_i,y_i)\boldsymbol{Q}(x_i,y_i)$ and $\boldsymbol{b} = \sum_{i=1}^{N_{gp}} \boldsymbol{Q}^{\mathrm{T}}(x_i,y_i)\Delta p^t_{w,gp}(x_i,y_i)$.

Finally, the pore pressure increments at the MPs located in the approximation domain Ω_i can be obtained as

$$\Delta p^t_{w,mp} = \boldsymbol{Q}(x_{mp},y_{mp})\boldsymbol{a} \tag{3.46}$$

and these can be used to derive the pore pressure at time $t+\Delta t$. For MPs near the domain boundary, there are insufficient grid cells to form a complete patch. For these cases, the pore pressure increments are determined by extending internal patches up to the MP

position. Similar concepts for determining stresses at the boundary nodes in FEM can be found in previous studies (Zienkiewicz & Zhu, 1992a,b; Zienkiewicz *et al.*, 2005).

3.3.4. CMPM STRESS INTEGRATION/RECOVERY

In general, MPM also suffers from oscillations and inaccuracies due to performing numerical integration and stress recovery at non-ideal (MP) locations. The recently developed Composite Material Point Method (CMPM) (González Acosta *et al.*, 2017, 2020), which extends the solution domain for each grid cell through considering the influence of neighbouring cells, can significantly alleviate stress oscillations and help to recover stresses for one-phase problems.

In CMPM, new grid cell shape functions are established based on an extended influence domain (i.e., a patch) using Lagrangian interpolation. All nodal displacements within this extended domain are used for stress recovery, which can lead to improved stress values at MPs. The constructed shape functions are summarised in Appendix A, while more details can be found in González Acosta *et al.* (2017, 2020). Here, CMPM is firstly extended to the case of coupled two-phase problems and then exploited to improve the recovery of effective stresses at MPs in selected verification examples.

3.3.5. NUMERICAL IMPLEMENTATION

Each step in the proposed GC-SRI-patch method is explicitly solved according to the following sequence of sub-steps (see also the flow chart in Figure 3.3):

(1) initialise all variables at the nodes of the background mesh (Eqs. (3.21)–(3.30));

(2) calculate the water nodal accelerations $\dot{\hat{\boldsymbol{v}}}_w^t$ using the discrete equilibrium equation for the water phase (Eq. (3.31));

(3) substitute the water nodal accelerations $\dot{\hat{\boldsymbol{v}}}_w^t$ into the discrete equilibrium equation for the soil–water mixture and calculate the soil nodal accelerations $\dot{\hat{\boldsymbol{v}}}_s^t$ (Eq. (3.32));

(4) update both soil and water nodal velocities using explicit forward Euler integration;

(5) update the velocity and position of all MPs;

(6) update the nodal velocities for both the soil and water by mapping variables back from the MPs;

(7) calculate the effective stresses at the MPs by using GIMP combined with CMPM (Eq. (3.37));

(8) calculate the pore pressure at the GPs via Eq. (3.40), and then recover the pore pressures at the MPs from the GPs using Eqs. (3.43)–(3.46);

(9) reset the background mesh and restart from (1) for the solution of the next calculation step.

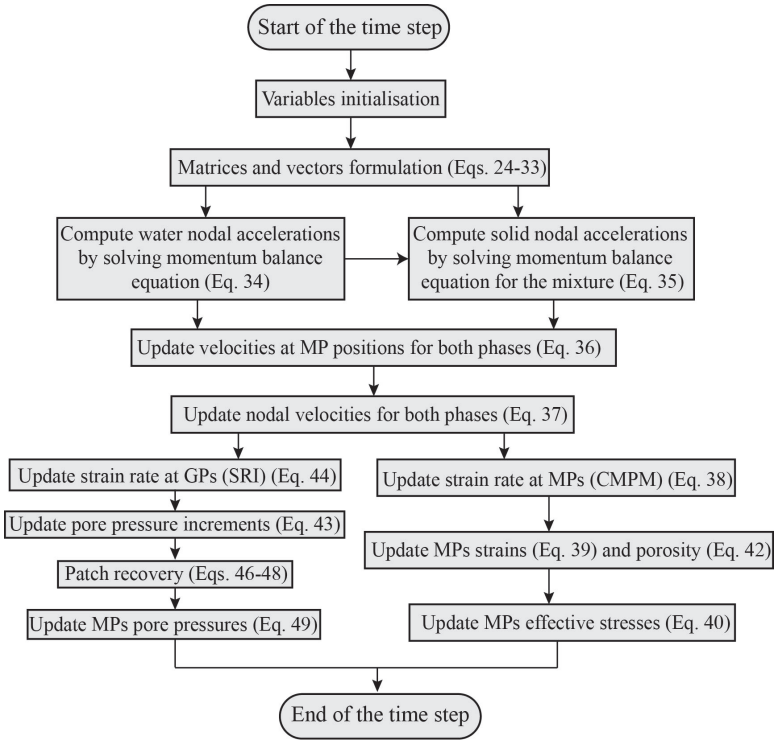

Figure 3.3: Numerical implementation of the coupled MPM algorithm

3.4. VERIFICATION EXAMPLES

THIS section presents three (plane strain) verification examples confirming the suitability of the proposed GC-SRI-patch method. In all examples the considered porous medium (soil) is fully saturated, with a solid skeleton modelled as isotropic linear elastic. Square background meshes are used in all cases, with each grid cell initially hosting four, equally-spaced material points. Given the emphasis of this work on the development of the GC-SRI-patch method, only relatively simple boundary conditions are considered in these analyses; further work will be devoted in the future to tackling more complex hydro-mechanical boundary conditions.

3.4.1. 1D CONSOLIDATION OF A SOIL COLUMN

The first example is Terzaghi's 1D consolidation problem, which is commonly used to verify numerical methods for coupled poromechanical problems (Bandara & Soga, 2015; Jeremić *et al.*, 2008). Figure 3.4a illustrates the problem geometry and boundary conditions. The width and height of the problem domain are 0.1 m and 1.0 m, respectively. The pore water is allowed to drain through the top surface, whereas all other boundaries are impermeable. The displacement boundary conditions are a fixed mesh base and rollers at the two vertical boundaries allowing only vertical displacement.

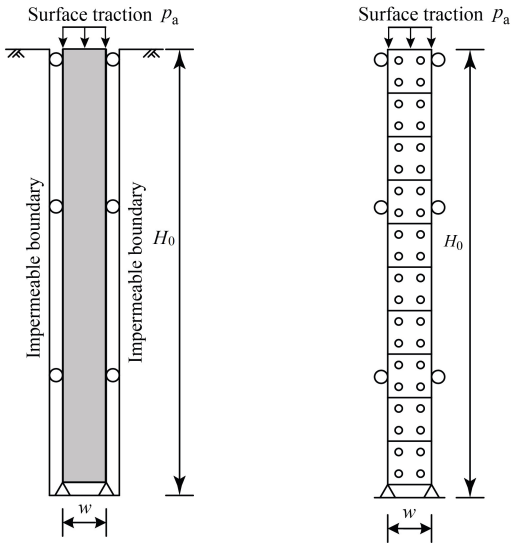

(a) Problem geometry (b) MPM discretisation

Figure 3.4: One dimensional consolidation test

The properties of the elastic soil skeleton and pore water are as follows: Young's modulus $E = 1.0 \times 10^3$ kPa, Possison's ratio $\nu = 0.0$, soil grain density $\rho_s = 2.65 \times 10^3$ kg/m^3, porosity $n = 0.3$, water bulk modulus $K_w = 2.2 \times 10^6$ kPa, hydraulic conductivity $k = 1.0 \times 10^{-4}$ m/s, and water density $\rho_w = 1.0 \times 10^3$ kg/m^3.

A uniformly distributed static load p_a, of either 1.0 kPa or 200.0 kPa (with no gravity loading), has been applied to the top surface to test GC-SRI-patch's performance for small or large deformations, respectively. The MPM discretisation is shown in Figure 3.4b. The problem domain is discretised by ten 4-node quadrilaterial grid cells of size 0.1 m × 0.1 m, while a time-step size of $\Delta t = 1.0 \times 10^{-6}$ s has been used for time marching. It should be noted that, instead of applying external tractions on the top layer of MPs, they are directly applied on the movable top surface of the column (Vardon *et al.*, 2019), as illustrated in Figure 3.5. For each MP, the support domain is defined by $2l_{px}$ and $2l_{py}$ in the horizontal and vertical directions, respectively. Thus, the location of the top boundary can be determined by the coordinates of the uppermost layer of MPs combined with the value of l_{py}. At each time step, the support domain of the MPs at time $t + \Delta t$ is updated as

$$l_{px}^{t+\Delta t} = l_{px}^{t}\left(1 + \Delta\varepsilon_{xx}^{t+\Delta t}\right) \tag{3.47a}$$

$$l_{py}^{t+\Delta t} = l_{py}^{t}\left(1 + \Delta\varepsilon_{yy}^{t+\Delta t}\right) \tag{3.47b}$$

where $\Delta\varepsilon_{xx}^{t+\Delta t}$ and $\Delta\varepsilon_{yy}^{t+\Delta t}$ are the calculated incremental strains over the time step Δt in the x and y directions, respectively. After determining the position of the top surface, the applied external distributed load $\bar{\tau}_{m,ts}$ is mapped from the top surface to the surrounding

background nodes $\tilde{\boldsymbol{\tau}}_{m,i}$ using regular shape functions:

$$\tilde{\boldsymbol{\tau}}_{m,i} = \boldsymbol{N}_i(\boldsymbol{x}_{ts})\tilde{\tau}_{m,ts}\frac{\Delta h}{2} \tag{3.48}$$

where $\boldsymbol{x}_{ts}$ is the position of top surface, and Δh is the grid size of the background square mesh. It should be pointed out that a linear shape function $\boldsymbol{N}_i(\boldsymbol{x}_{ts})$ is used here for the mapping of the applied external load.

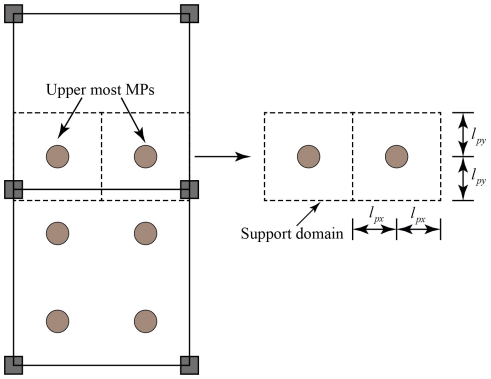

Figure 3.5: Movable top boundary determination for one dimensional analysis

SMALL DEFORMATION ANALYSIS

Figure 3.6 compares the GC-SRI-patch solution to the corresponding analytical solution for different values of the (dimensionless) time factor T_v, defined as

$$T_v = \frac{c_v t}{H_v^2} \tag{3.49}$$

where H_v is the drainage path length (here equal to the thickness of the soil layer), and c_v is the coefficient of consolidation defined by[1]

$$c_v = \frac{k}{\gamma_w(\frac{1}{E} + \frac{n}{K_w})} \tag{3.50}$$

The small deformation analytical solution, reported by Terzaghi (1943), relies on the assumption that the layer thickness (H_v), hydraulic conductivity (k), and Young's modulus (E) of the soil layer remain constant during the consolidation process. For a clearer comparison, a dimensionless pore pressure p and a dimensionless current layer thickness H are introduced:

$$p = p_w / p_a, \qquad H = H_v / H_0 \tag{3.51}$$

[1] The stiffness modulus under confined one-dimensional compression (so-called "oedometric modulus") coincides with E for the considered case of $\nu = 0.0$.

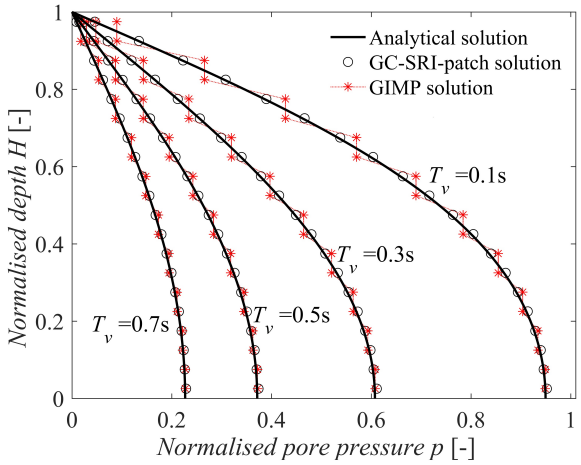

(a) Excess pore pressure isochrones

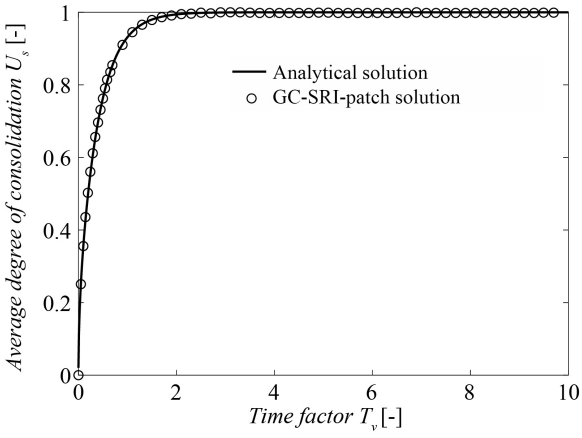

(b) Average degree of consolidation

Figure 3.6: Comparison between GC-SRI-patch, GIMP and analytical consolidation solutions – small deformation analysis

The analytical solution for the considered initial/boundary conditions can be expressed in terms of pore pressure as a function of dimensionless depth and time (as shown in Figure 3.6a):

$$p(H,T_v)=\sum_{m=1}^{\infty}\frac{2}{M}\sin(MH)e^{-M^2T_v} \tag{3.52}$$

where $M=(m-\frac{1}{2})\pi$. The average degree of consolidation, as shown in Figure 3.6b is defined as

$$U_s=1-\sum_{m=1}^{\infty}\frac{2}{M^2}e^{-M^2T_v} \tag{3.53}$$

The results in Figure 3.6 confirm the excellent agreement between the analytical and GC-SRI-patch solutions in terms of both excess pore pressure and average degree of consolidation. The proposed smooth distributions of pore pressure further demonstrate the advantage of the GC-SRI-patch even when using a relatively coarse background mesh. In comparison, the GIMP solution shows piecewise constant pore pressures over each cell. Similar results can also be found in Bandara & Soga (2015), where a much finer background mesh is needed to obtain a satisfactory solution (note that in Bandara & Soga (2015) a mesh ten times finer than in the present GC-SRI-patch case is used).

LARGE DEFORMATION ANALYSIS

The reference large deformation theory of soil consolidation was developed by Gibson *et al.* (1967). Among other aspects, the presence of large deformations makes it no longer appropriate to consider a constant H_v and k, as their values may change significantly due to soil deformation and reduction in porosity (n). This aspect is captured in the analytical solution presented in Xie & Leo (2004), which builds on Gibson's theory and the assumption of porosity-dependent hydraulic conductivity $k_t(n)$, given as:

$$k_t(n) = k_0 \left(\frac{1-n_0}{1-n} \right)^2 \tag{3.54}$$

where k_0 and n_0 are the initial hydraulic conductivity and porosity, respectively, which are the same as used above for the small deformation case. According to Xie and Leo's large deformation solution (Xie & Leo, 2004), the dimensionless pore pressure varies in space and time as follows:

$$p(H, T_v) = \frac{1}{m_{vl} p_a} \ln \left\{ 1 + (e^{m_{vl} p_a} - 1) \sum_{m=1}^{\infty} \frac{2}{M} \sin(MH) e^{-M^2 T_v} \right\} \tag{3.55}$$

where $m_{vl} = 1/E$ is the 1D compressibility[2] and p_a is the applied external load.

The analytical and GC-SRI-patch solutions, which are both based on the relationship in Equation (3.54), are compared in Figure 3.7. The numerical and analytical excess pore pressure isochrones at different average degrees of consolidation U_s, from $U_s = 0$ to $U_s = 0.9$, are compared in Figure 3.7a. In the presence of large deformations, U_s is obtained as

$$U_s = \frac{S_t}{S_\infty} \tag{3.56}$$

where S_t is the top surface settlement at time t, calculated analytically as

$$S_t = H_0 (1 - e^{-m_{vl} p_a}) (1 - \sum_{m=1}^{\infty} \frac{2}{M^2} e^{-M^2 T_v}) \tag{3.57}$$

and S_∞ is the asymptotic value of S_t as $T_v \to \infty$:

$$S_\infty = H_0 (1 - e^{-m_{vl} p_a}) \tag{3.58}$$

[2] In the reference analytical solution (Xie & Leo, 2004), m_{vl} is assumed not to vary with soil porosity as a first approximation.

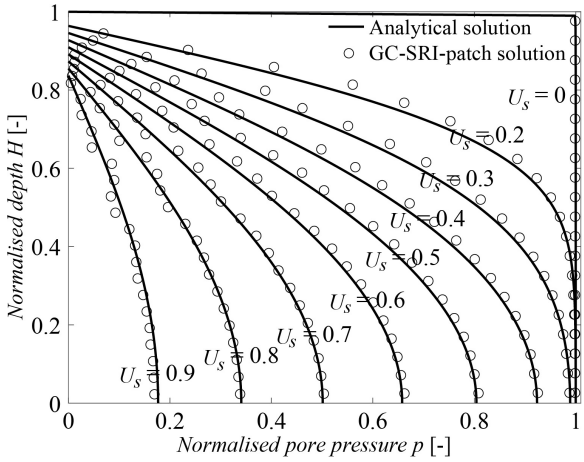

(a) Excess pore pressure isochrones

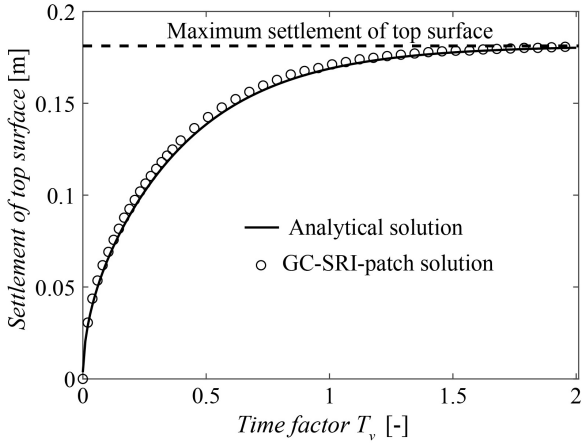

(b) Settlement of top surface

Figure 3.7: Comparison between GC-SRI-patch and analytical consolidation solutions – large deformation analysis

The comparison in terms of top surface settlement is given in Figure 3.7b. Overall, Figure 3.7 shows that the GC-SRI-patch results compare well with the analytical large-deformation solution, notwithstanding the simplified representation of the strain field mentioned in Section 2.1. However, slight pore pressure oscillations are visible near the top boundary in Figure 3.7a, which may be related to the external load being applied at the top of the MPM domain and then transferred to the background mesh nodes using shape functions.

It should be noted that, in the large deformation case, large pore pressure oscillations (at MPs) near the top domain boundary lead the explicit GIMP simulation to abort after significant displacement of the MPs. For comparison purposes, Figure 3.8 shows pore

pressure profiles corresponding to $U_s = 0.15$ for the GC-SRI-patch, GIMP, and analytical solutions. The comparison further demonstrates the applicability of the explicit stabilised GC-SRI-patch method proposed in this study.

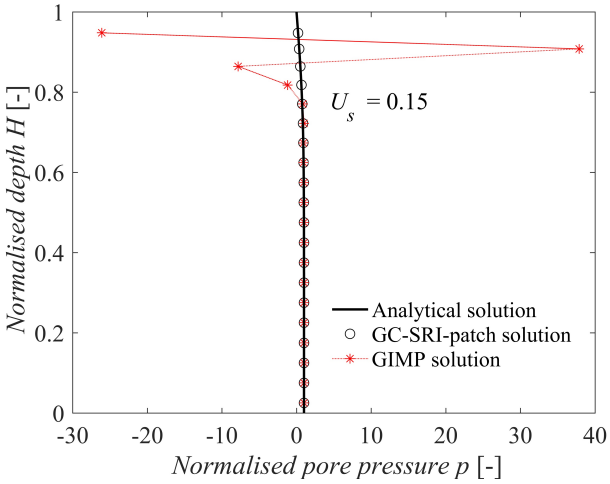

Figure 3.8: Comparison between GC-SRI-patch, GIMP and analytical consolidation solutions – large deformation analysis with $U_s = 0.15$

3.4.2. PRESSURISED HOLLOW CYLINDER

In this benchmark, a two-phase hollow cylinder subjected to an internal pressure is studied. The problem geometry and boundary conditions are shown in Figure 3.9. The inner and outer cylinder radii are $r_i = 0.20\,\text{m}$ and $r_e = 1.20\,\text{m}$, respectively, giving a cylinder wall thickness of 1.0 m. The height of the cylinder H is equal to 1.0 m, while the problem domain is discretised using grid cells of dimensions $\Delta r = \Delta y = 0.20\,\text{m}$. The boundary conditions are that the nodes at the top and bottom of the domain are only allowed to move in the radial direction, while the nodes at the outer boundary are fully fixed. The pore water is not allowed to flow in/out of the cylinder, so as to replicate (globally) undrained conditions. The soil and water properties are the same as in Section 3.4.1.

The benchmark has been solved by applying an internal total pressure $p_i = 100\,\text{kPa}$. Since drainage is not allowed, the pressure applied to the cylinder is transferred onto the (nearly incompressible) pore water. The near incompressibility also implies that the MPs do not displace significantly from their original positions.

Figure 3.10 compares the normalised radial excess pore pressure distribution through the cylinder wall obtained using MPM, GIMP and GC-SRI-patch. Because the location of the MPs hardly change due to the pressurisation, the pore pressures obtained via MPM and GIMP are almost identical. The results obtained using GC-SRI-patch correctly show a constant pore pressure, equal to the applied pressure p_i, through the cylinder wall. In contrast, large pore pressure oscillations are observed in both the MPM and GIMP solutions, with values near the pressurised boundary being significantly smaller than the

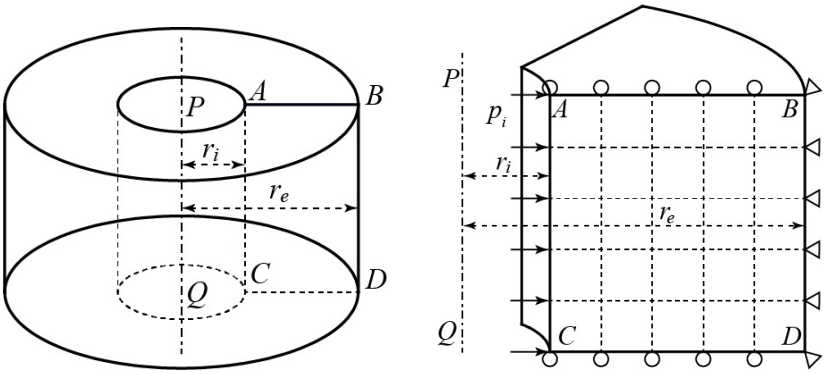

(a) Problem geometry (b) Axisymmetric discretisation

Figure 3.9: Hollow cylinder subjected to internal pressurisation

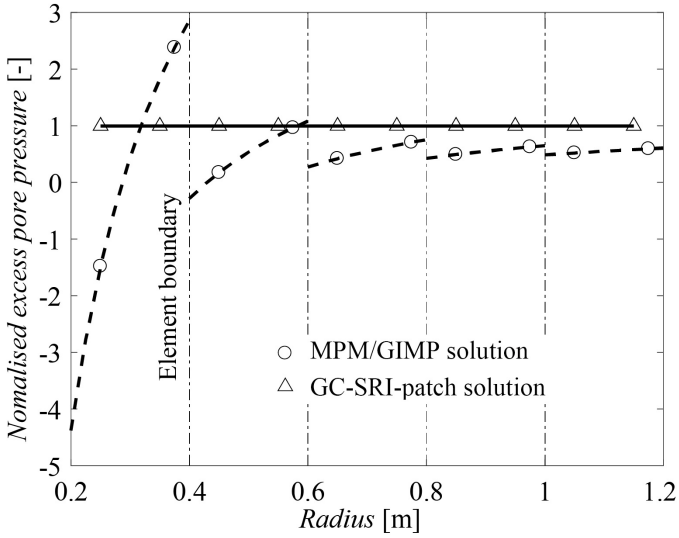

Figure 3.10: Distribution of simulated excess pore pressure along the radial direction

applied pressure.

3.4.3. 2D SLUMPING BLOCK (SELF-WEIGHT CONSOLIDATION)

In this section, the 2D large-deformation consolidation of an elastic slumping block (of width and height equal to 4 m and 2 m, respectively) under the sole action of gravity is studied (Zhao & Choo, 2020). Taking advantage of symmetry, only the right half of the domain is considered as shown in Figure 3.11a. Both the top and right boundaries are unconstrained and freely draining, while the left and bottom boundaries are impermeable and supported by rollers. No surface loads are applied, so that the consolidation process is exclusively driven by gravity loading applied with a ramp-like time history to avoid

dynamic oscillations (Figure 3.11b). The gravitational force gives rise to pore pressure build-up, the dissipation of which promotes gradual deformation of the block.

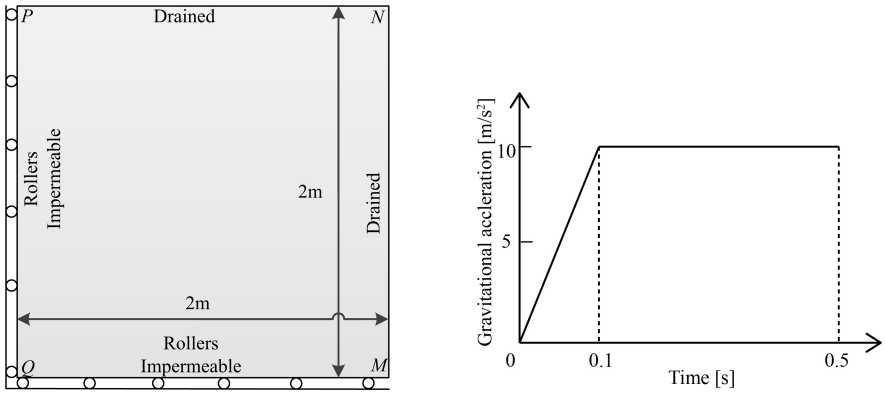

(a) Problem domain

(b) Applied gravity ramp

Figure 3.11: Layout of the 2D slumping block problem (self-weight consolidation)

The soil and water properties are: Young's modulus $E = 1.0 \times 10^2$ kPa, Possison's ratio $\nu = 0.3$, soil grain density $\rho_s = 2.65 \times 10^3$ kg/m^3, initial porosity $n = 0.4$, water bulk modulus $K_w = 2.2 \times 10^6$ kPa, initial hydraulic conductivity $k = 1.0 \times 10^{-4}$ m/s, and water density $\rho_w = 1.0 \times 10^3$ kg/m^3. The problem domain is discretised using 16×16, 4-node quadrilateral grid cells of size 0.125 m $\times$ 0.125 m. Time-domain simulations were performed with a time-step size equal to $\Delta t = 1.0 \times 10^{-6}$ s. For comparative purposes, standard MPM, GIMP, and GC-SRI-patch methods were used to analyse the problem.

Figure 3.12 shows the excess pore pressure distributions at $t = 0.05$ s obtained in the MPM, GIMP and GC-SRI-patch analyses. Due to only limited displacement experienced by the MPs up to that time, the MPM and GIMP analyses return very similar results. However, large pore pressure oscillations in a typical checkerboard pattern are visible in Figure 3.12a. Because of the lack of MP grid crossing during the short time considered, the observed oscillation may be attributed to incompressibility and related instabilities. The extent of the oscillatory behaviour increases as the consolidation process evolves, and causes the explicit GIMP simulation to abort soon after the end of the loading ramp. This confirms the ineffectiveness of the low-order, non-stabilised GIMP scheme for incompressible problems (González Acosta *et al.*, 2019).

The excess pore pressure response resulting from the proposed GC-SRI-patch is presented in Figure 3.12b. In contrast with the GIMP checkerboard pattern shown in Figure 3.12a, the GC-SRI-patch solution appears to be oscillation-free with compressive pore pressures everywhere. Due to the relatively quick gravity loading, water cannot rapidly drain and the numerical simulation develops under approximately undrained conditions. Therefore, the applied gravity loading is mostly translated into pore water pressure increase, as can be observed in Figure 3.12b. Unlike a uniform pore pressure in each grid cell, the pore pressures show a continuous distribution both within each grid cell and at inter-cell boundaries. The visible smoothness of the pore pressure field further confirms the suitability of the proposed GC-SRI-patch, even very near the undrained-

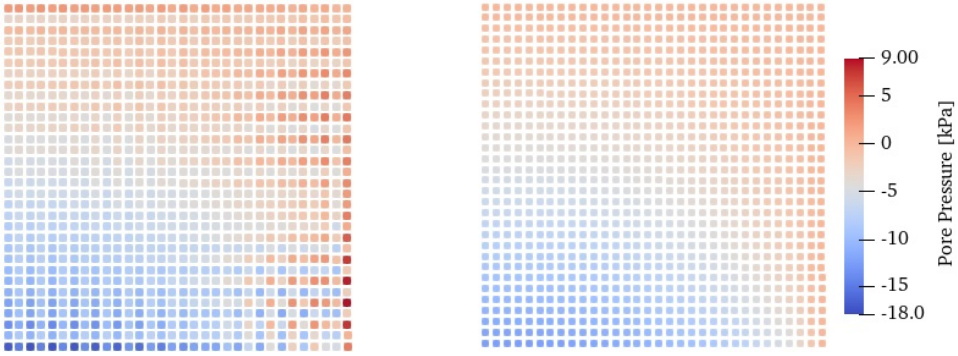

(a) MPM/GIMP (b) GC-SRI-patch

Figure 3.12: Excess pore pressures at $t = 0.05\,\text{s}$ obtained with MPM/GIMP and GC-SRI-patch

incompressible limit.

Additionally, Figure 3.13 shows the simulated excess pore pressure distributions at different times during the self-weight consolidation, from $t = 0.1\,\text{s}$ until $t = 0.5\,\text{s}$. As observed in Ma *et al.* (2010) with regard to the GIMP method, if MPs are located at the far sides of a cell, the masses of some nodes (typically those close to the domain surface) may become small while shape function gradients and nodal forces may not. As nodal accelerations are explicitly obtained by dividing total nodal forces by nodal masses, large accelerations are obtained, which can in turn cause numerical instability. To alleviate acceleration inaccuracies, a distribution coefficient algorithm to deal with small nodal masses in MPM was proposed by Ma *et al.* (2010), and applied in this study in combination with the proposed GC-SRI-patch method. Following the distribution coefficient algorithm, a part of the force acting on a node with a small mass is transferred to neighbouring nodes with a larger mass, so that mass and momentum conservation laws continue to be fulfilled. However, in the author's opinion, such an algorithm cannot fully resolve acceleration inaccuracies near domain boundary nodes. Moreover, the same issue is particularly problematic in two-phase coupled problems, as it leads to spurious pore pressure oscillations in the presence of nearly incompressible pore water. For this benchmark, it was observed that pore pressure increments $\Delta p^t_{w,gp}$ at the GPs were usually very small (i.e., $\Delta p^t_{w,gp} \leq 1 \times 10^{-5}\,\text{kPa}$), but occasionally very large values (i.e., $\Delta p^t_{w,gp} \geq 1.0 \times 10^{-3}\,\text{kPa}$) occurred for some grid cells at the domain boundary, especially those cells not containing MPs but influenced by the particle support domain within the framework of GIMP. These spurious large increments are directly related to large nodal accelerations caused by the small nodal mass issue that typically occurs near the domain surface. These large pore pressure increments can lead to inaccurate pore pressure recovery at a small number of surrounding MPs (less than 1% of the total number of MPs). Without special treatment, these inaccurate pore pressures may propagate to the whole problem domain and result in a misleading pore pressure distribution across all MPs. For this reason, if the calculated pore pressure increment $\Delta p^t_{w,gp}$ of a grid cell at the domain boundary is larger in absolute value than a specified threshold ζ_d (for this benchmark,

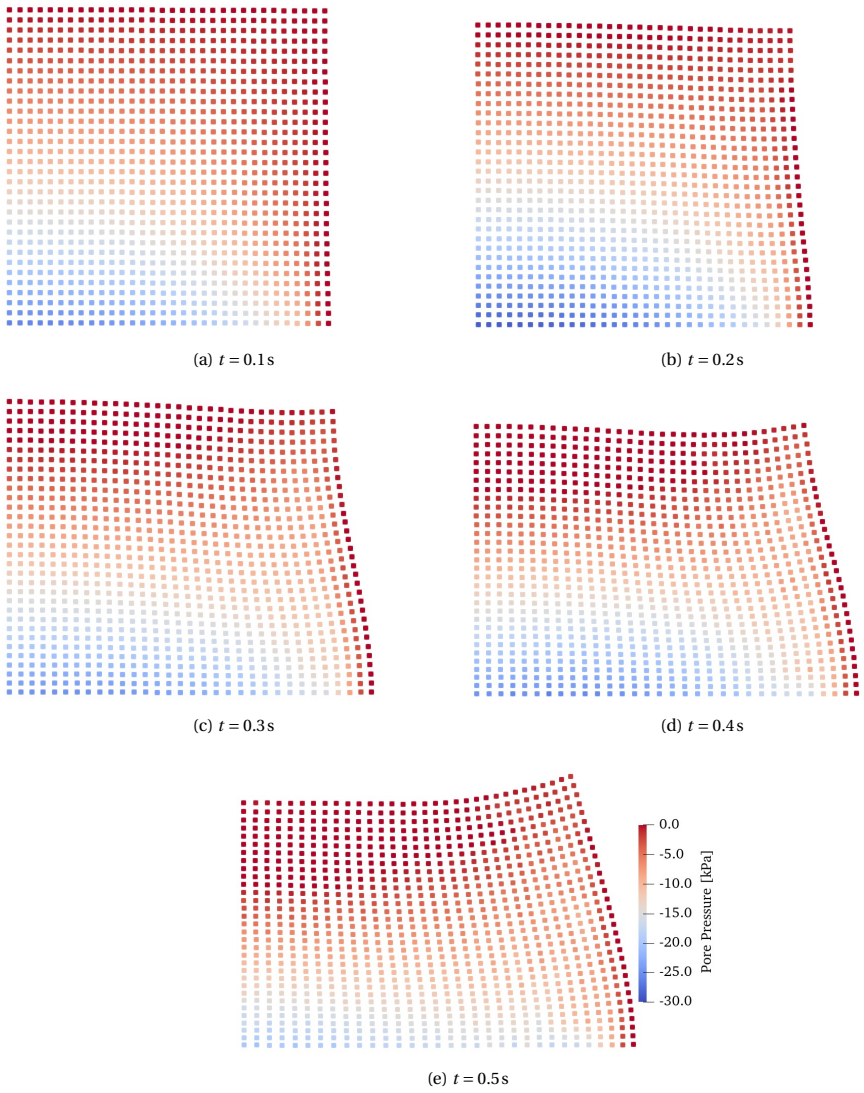

(a) $t = 0.1\,\mathrm{s}$ (b) $t = 0.2\,\mathrm{s}$

(c) $t = 0.3\,\mathrm{s}$ (d) $t = 0.4\,\mathrm{s}$

(e) $t = 0.5\,\mathrm{s}$

Figure 3.13: Excess pore pressures at different times obtained with GC-SRI-patch (1024 MPs)

$\zeta_d = 1.0 \times 10^{-3}\,\mathrm{kPa}$), then it is set to zero. Even though this treatment was rarely used in this analysis and influenced only a small number of MPs, it was found to be generally effective in suppressing spurious pore pressure oscillations originating from MPs near the domain boundary.

Figures 3.13a – 3.13e show how pore water drainage takes place gradually through the permeable boundaries of the block and promotes mechanical deformation of the solid skeleton during consolidation. As is apparent in Figure 3.13a – 3.13c, the pore pressure dissipation is not monotonic in time, an occurrence associated in 2D problems with the

so-called Mandel-Cryer effect (Mandel, 1953; Cryer, 1963). The same characteristic is more clearly illustrated in Figure 3.14, where the time evolution of the excess pore pressure at two selected MPs (A and B) is plotted for both GIMP and GC-SRI-patch simulations. Stable GIMP results are only available up to shortly after the end of the gravity ramp loading. Conversely, GC-SRI-patch provides stable results for the entire duration of the hydromechanical analysis. In addition, it can be observed that the results of GC-SRI-patch with a much coarser mesh are quite similar to the solutions provided in Zhao & Choo (2020). The deviatoric stress (defined as $\sqrt{\frac{1}{2}((\sigma_1-\sigma_2)^2+(\sigma_2-\sigma_3)^2+(\sigma_3-\sigma_1)^2)}$, where σ_1, σ_2 and σ_3 are principal stresses) distributions shown in Figure 3.15 demonstrate the applicability of CMPM in coupled problems, and further validate the performamce of the proposed GC-SRI-patch.

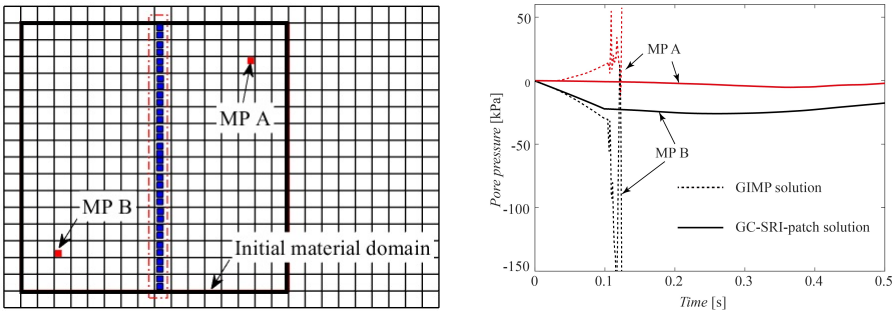

(a) Reference MPs

(b) GIMP vs GC-SRI-patch solutions

Figure 3.14: Time evolution of excess pore pressure at two reference MPs in the slumping block

Figure 3.16 displays the evolution in time, during and after the gravity ramp, of the excess pore pressure at the middle section of the slumping block (i.e., along the column of MPs highlighted in Figure 3.14a). It is worth noting that the proposed GC-SRI-patch method captures correctly the gradual build-up of pore pressures during the ramp loading, as well as the downward propagation of a pore pressure wave when the increase in gravity is suddenly arrested at $t = 0.1$ s. Such propagation occurs simultaneously with global pore pressure dissipation, and is a natural outcome of the complete dynamic formulation.

To determine the influence of space discretisation on the numerical solution, two additional space discretisations are used to simulate the consolidation of the slumping block (i.e., 400 and 2500 MPs initially placed on 100 and 625 square grid cells, respectively). Figure 3.17 shows the calculated excess pore pressures at different times using GC-SRI-patch for both cases. The GC-SRI-patch returns stabilised solutions for both additional discretisations, with encouraging convergence performance upon mesh refinement – compare to the results in Figure 3.13.

3.5. CONCLUSIONS

THIS study has presented an explicit, stabilised two-phase material point method named GC-SRI-patch for application in coupled poromechanical problems. The Generalised Interpolation Material Point (GIMP) method with a single set of MPs was

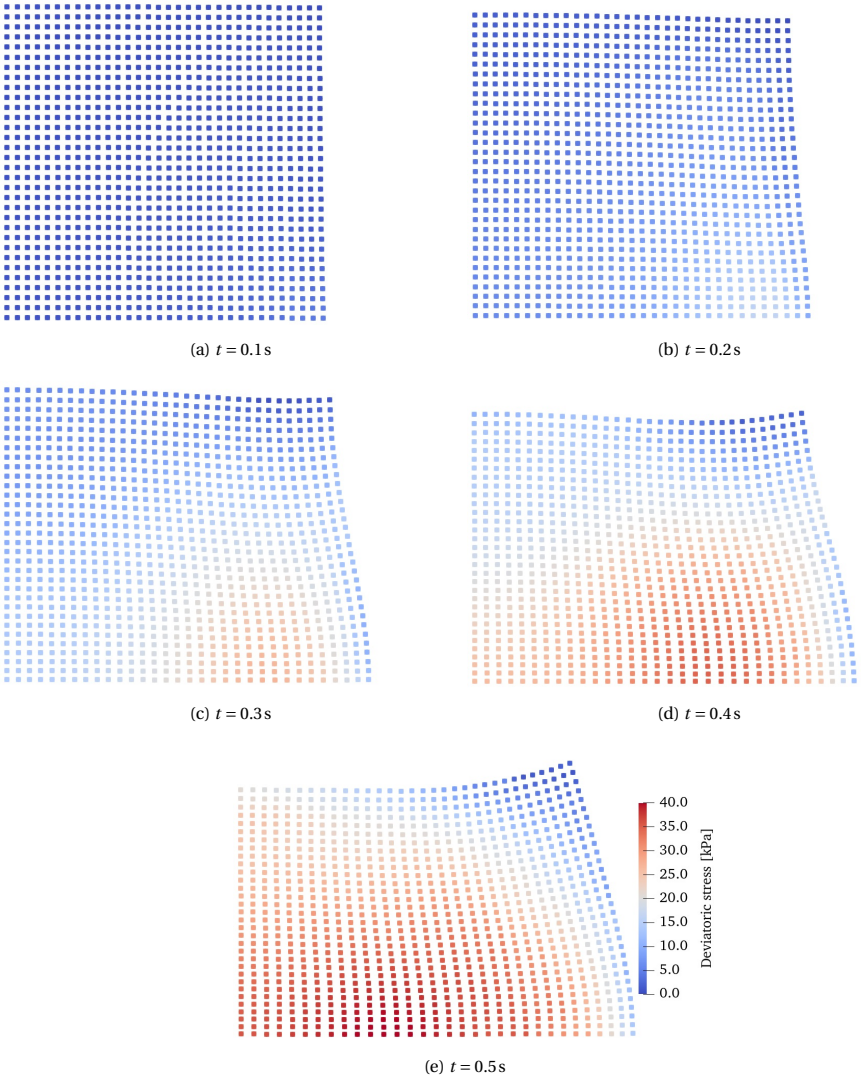

(a) $t = 0.1\,\mathrm{s}$ (b) $t = 0.2\,\mathrm{s}$

(c) $t = 0.3\,\mathrm{s}$ (d) $t = 0.4\,\mathrm{s}$

(e) $t = 0.5\,\mathrm{s}$

Figure 3.15: Deviatoric stress distributions at different times obtained with GC-SRI-patch (1024 MPs)

adopted to alleviate cell-crossing errors and reduce the computational burden. To avert pore pressure instabilities, a Selective Reduced Integration (SRI) was used for the calculation of pore pressure increments at central GPs, which are of high(er) accuracy and convergence order. Such increments are then mapped to MPs using the proposed linear patch based on a Moving Least Squares Approximation (MLSA). Further improvement of effective stress recovery was achieved through the recently proposed Composite Material Point Method (CMPM), here applied for the first time to coupled two-phase problems. Other practical issues, including application of a surface traction on a movable boundary

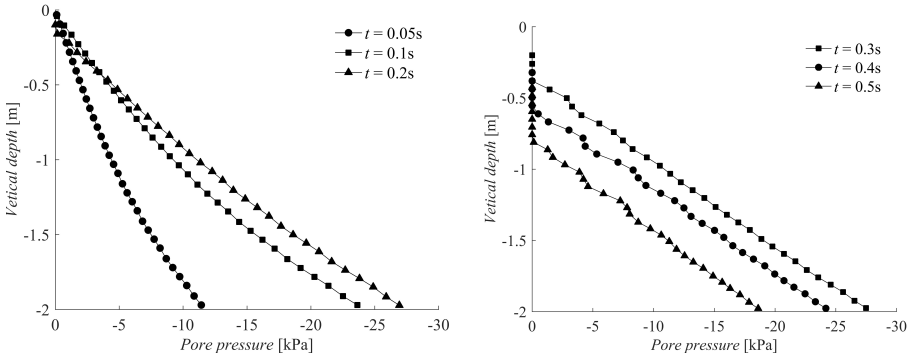

(a) During gravity ramp (b) After gravity ramp

Figure 3.16: Evolution in time of the excess pore pressure profile at the middle section of the slumping block model – GC-SRI-patch solution

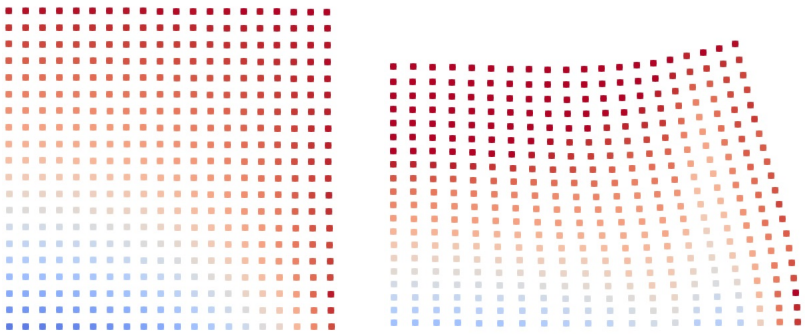

(a) 400 MPs (Left: $t = 0.1$ s; Right: $t = 0.5$ s)

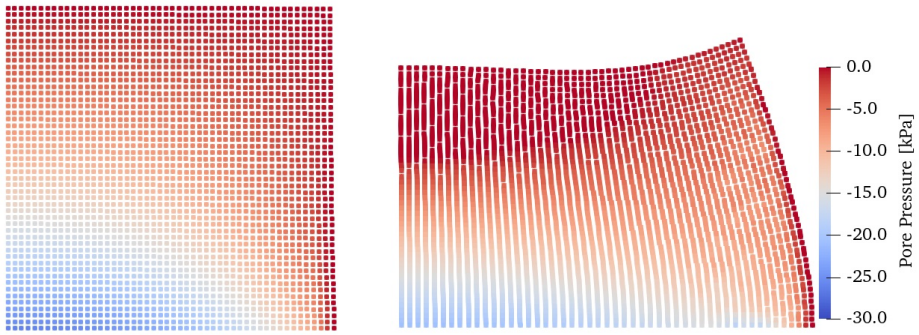

(b) 2500 MPs (Left: $t = 0.1$ s; Right: $t = 0.5$ s)

Figure 3.17: Excess pore pressures at different times obtained with GC-SRI-patch

and the mitigation of 'small mass' issues near the domain boundaries, were also investigated.

Numerical verification examples supported the conclusion that the proposed GC-SRI-

patch method can effectively be used to analyse relevant hydromechanical processes over a wide range of loading/drainage conditions. Instead of piecewise constant pore pressures over each cell, the proposed pore pressures return continuous distributions both within grid cells and at inter-cell boundaries, even in the presence of a coarse background grid. In particular, pore pressure instabilities were greatly mitigated by the new method, as is clearly demonstrated by the benchmark numerical solutions in terms of pore pressures and effective stresses. Future work will be devoted to further testing more challenging large-deformation analyses, more complex hydro-mechanical boundary conditions and more sophisticated constitutive models for the soil skeleton.

REFERENCES

Abe, K., Soga, K. & Bandara, S. (2013). Material point method for coupled hydromechanical problems. *Journal of Geotechnical and Geoenvironmental Engineering* **140**, No. 3, 04013033.

Bandara, S. & Soga, K. (2015). Coupling of soil deformation and pore fluid flow using material point method. *Computers and Geotechnics* **63**, 199–214.

Bardenhagen, S. G. & Kober, E. M. (2004). The generalized interpolation material point method. *Computer Modeling in Engineering and Sciences* **5**, No. 6, 477–496.

Bathe, K. J. (2001). The inf–sup condition and its evaluation for mixed finite element methods. *Computers and Structures* **79**, No. 2, 243–252.

Bathe, K. J. (2006). *Finite element procedures*. Klaus-Jurgen Bathe.

Belytschko, T., Liu, W. K., Moran, B. & Elkhodary, K. (2013). *Nonlinear finite elements for continua and structures*. Wiley: New York.

Brezzi, F. & Bathe, K. J. (1990). A discourse on the stability conditions for mixed finite element formulations. *Computer Methods in Applied Mechanics and Engineering* **82**, No. 1-3, 27–57.

Chen, Z. P., Zhang, X., Sze, K. Y., Kan, L. & Qiu, X. M. (2018). v-p material point method for weakly compressible problems. *Computers and Fluids* **176**, 170–181.

Coombs, W. M., Charlton, T. J., Cortis, M. & Augarde, C. E. (2018). Overcoming volumetric locking in material point methods. *Computer Methods in Applied Mechanics and Engineering* **333**, 1–21.

Cryer, C. (1963). A comparison of the three-dimensional consolidation theories of Biot and Terzaghi. *The Quarterly Journal of Mechanics and Applied Mathematics* **16**, No. 4, 401–412.

Gan, Y., Sun, Z., Chen, Z., Zhang, X. & Liu, Y. (2018). Enhancement of the material point method using b-spline basis functions. *International Journal for Numerical Methods in Engineering* **113**, No. 3, 411–431.

Gibson, R., England, G. & Hussey, M. (1967). The theory of one-dimensional consolidation of saturated clays: 1. finite non-linear consildation of thin homogeneous layers. *Geotechnique* **17**, No. 3, 261–273.

González Acosta, L. J., Vardon, P. J. & Hicks, M. A. (2017). Composite material point method (CMPM) to improve stress recovery for quasi-static problems. *Procedia Engineering* **175**, 324–331.

González Acosta, L. J., Vardon, P. J., Remmerswaal, G. & Hicks, M. A. (2020). An investigation of stress inaccuracies and proposed solution in the material point method. *Computational Mechanics* **65**, No. 2, 555–581.

González Acosta, L. J., Zheng, X. C., Vardon, P. J., Hicks, M. A. & Pisanó, F. (2019). On stress oscillation in MPM simulations involving one or two phases. In *MPM 2019: 2nd International Conference on the Material Point Method for Modelling Soil–Water–Structure Interaction*.

Holzapfel, A. G. (2000). *Nonlinear solid mechanics II*. Wiley: New York.

Jassim, I., Stolle, D. & Vermeer, P. (2013). Two-phase dynamic analysis by material point method. *International Journal for Numerical and Analytical Methods in Geomechanics* **37**, No. 15, 2502–2522.

Jeremić, B., Cheng, Z., Taiebat, M. & Dafalias, Y. (2008). Numerical simulation of fully saturated porous materials. *International Journal for Numerical and Analytical Methods in Geomechanics* **32**, No. 13, 1635–1660.

Kafaji, I. K. a. (2013). *Formulation of a dynamic material point method (MPM) for geomechanical problems*. Ph.D. thesis, University of Stuttgart.

Li, X., Han, X. & Pastor, M. (2003). An iterative stabilized fractional step algorithm for finite element analysis in saturated soil dynamics. *Computer Methods in Applied Mechanics and Engineering* **192**, No. 35-36, 3845–3859.

Ma, X., Giguere, P. T., Jayaraman, B. & Zhang, D. Z. (2010). Distribution coefficient algorithm for small mass nodes in material point method. *Journal of Computational Physics* **229**, No. 20, 7819–7833.

Mandel, J. (1953). Consolidation des sols (étude mathématique). *Geótechnique* **3**, No. 7, 287–299.

McGann, C. R., Arduino, P. & Mackenzie-Helnwein, P. (2015). A stabilized single-point finite element formulation for three-dimensional dynamic analysis of saturated soils. *Computers and Geotechnics* **66**, 126–141.

Pisanò, F. & Pastor, M. (2011). 1D wave propagation in saturated viscous geomaterials: Improvement and validation of a fractional step Taylor–Galerkin finite element algorithm. *Computer Methods in Applied Mechanics and Engineering* **200**, No. 47-48, 3341–3357.

Steffen, M., Kirby, R. M. & Berzins, M. (2008). Analysis and reduction of quadrature errors in the material point method (MPM). *International Journal for Numerical Methods in Engineering* **76**, No. 6, 922–948.

Sulsky, D., Chen, Z. & Schreyer, H. L. (1994). A particle method for history-dependent materials. *Computer Methods in Applied Mechanics and Engineering* **118**, No. 1-2, 179–196.

Sulsky, D., Zhou, S. J. & Schreyer, H. L. (1995). Application of a particle-in-cell method to solid mechanics. *Computer Physics Communications* **87**, No. 1-2, 236–252.

Terzaghi, K. (1943). *Theoretical soil mechanics*. Wiley: New York.

Tielen, R., Wobbes, E., Möller, M. & Beuth, L. (2017). A high order material point method. *Procedia Engineering* **175**, 265–272.

Tran, Q. A., Sołowski, W., Berzins, M. & Guilkey, J. (2020). A convected particle least square interpolation material point method. *International Journal for Numerical Methods in Engineering* **121**, No. 6, 1068–1100.

Tran, Q. A., Wobbes, E., Sołowski, W., Möller, M. & Vuik, C. (2019). Moving least squares reconstruction for B-spline material point method. In *MPM 2019: 2nd International Conference on the Material Point Method for Modelling Soil–Water–Structure Interaction*.

Vardon, P. J., Remmerswaal, G., Bolognin, M. & Hicks, M. A. (2019). Application of boundary conditions in MPM. In *Proceedings of the Mathematics of Finite Elements and Applications (MAFELAP)*.

Wang, B., Vardon, P. J. & Hicks, M. A. (2018). Rainfall-induced slope collapse with coupled material point method. *Engineering Geology* **239**, 1–12.

White, J. A. & Borja, R. I. (2008). Stabilized low-order finite elements for coupled solid-deformation/fluid-diffusion and their application to fault zone transients. *Computer Methods in Applied Mechanics and Engineering* **197**, No. 49-50, 4353–4366.

Xie, K. & Leo, C. J. (2004). Analytical solutions of one-dimensional large strain consolidation of saturated and homogeneous clays. *Computers and Geotechnics* **31**, No. 4, 301–314.

Zhao, Y. & Choo, J. (2020). Stabilized material point methods for coupled large deformation and fluid flow in porous materials. *Computer Methods in Applied Mechanics and Engineering* **362**, 112742.

Zheng, X. C., Pisanò, F., Vardon, P. J. & Hicks, M. A. (2021). An explicit stabilised material point method for coupled hydromechanical problems in two-phase porous media. *Computers and Geotechnics* **135**, 104112.

Zienkiewicz, O. C., Chan, A., Pastor, M., Schrefler, B. & Shiomi, T. (1999). *Computational geomechanics*. Wiley: New York.

Zienkiewicz, O. C., Taylor, R. L. & Zhu, J. Z. (2005). *The finite element method: its basis and fundamentals*. Elsevier: Oxford.

Zienkiewicz, O. C. & Zhu, J. (1992a). The superconvergent patch recovery (SPR) and adaptive finite element refinement. *Computer Methods in Applied Mechanics and Engineering* **101**, No. 1-3, 207–224.

Zienkiewicz, O. C. & Zhu, J. Z. (1992b). The superconvergent patch recovery and a posteriori error estimates. part 2: Error estimates and adaptivity. *International Journal for Numerical Methods in Engineering* **33**, No. 7, 1365–1382.

4

FORMULATION AND VERIFICATION OF A FULLY IMPLICIT THREE-FIELD MPM FOR DYNAMIC COUPLED PROBLEMS

This chapter presents the formulation and implementation of a fully implicit stabilised Material Point Method (MPM) for dynamic problems in two-phase porous media. In particular, the proposed method is built on a three-field formulation of the governing conservation laws, which uses solid displacement, pore pressure and fluid displacement as primary variables (u–p–U formulation). Stress oscillations associated with grid-crossing and pore pressure instabilities near the undrained/incompressible limit are mitigated by implementing enhanced shape functions according to the Generalised Interpolation Material Point (GIMP) method, as well as a patch recovery of pore pressures – from background nodes to material points – based on the same Moving Least Square Approximation (MLSA) approach investigated in Chapter 3 (Zheng et al., 2021a). The accuracy and computational convenience of the proposed method are discussed with reference to several poroelastic verification examples, spanning different regimes of material deformation (small versus large) and dynamic motion (slow versus fast).

Parts of this chapter appear in Zheng *et al.* (2021b).

4.1. INTRODUCTION

MOST current coupled MPMs published so far, including the work of Zheng *et al.* (2021a), adopt explicit time integration. Although the implementation of an explicit scheme is relatively straightforward, it may not fully suit the solution of (nearly) incompressible coupled problems, due to the stringent time step restrictions that result in the presence of a relatively stiff pore fluid (such as water in soil-like mixtures). However, only very few instances of semi-implicit (Kularathna *et al.*, 2021) and fully implicit (Zhao & Choo, 2020) coupled schemes have been proposed to date, although it is well known that, for uncoupled problems, the implicit version of MPM (Cummins & Brackbill, 2002; Guilkey & Weiss, 2003; Sulsky & Kaul, 2004; Wang *et al.*, 2016; Charlton *et al.*, 2017; Coombs *et al.*, 2020; González Acosta *et al.*, 2021) generally allows for larger time steps and can be more stable. Hence, this is the approach followed in this study.

As standard MPM formulations (and its variant GIMP) often use low-order shape functions over the background mesh for the relevant field variables (usually two), pore pressure instabilities may arise in the vicinity of the so-called undrained–incompressible limit. Similarly to that observed for two-phase FEM models, the violation of the well-known *inf-sup* condition can result in undesired pore pressure oscillations and, overall, inaccurate results (Brezzi & Bathe, 1990; Bathe, 2001). A typical countermeasure (often applied in FEM) is to use different orders of interpolation for the primary variables – e.g., in u–p-based two-phase models, the displacement field would require shape functions of higher order than for the pore pressure (Taylor & Hood, 1973). However, the computational convenience of equal/low-order interpolation in MPM has promoted the development of MPMs that can suppress pore pressure instabilities by means of fractional time stepping (Jassim *et al.*, 2013), polynomial pressure projection (Zhao & Choo, 2020), and reduced integration (Abe *et al.*, 2013; Bandara & Soga, 2015; Wang *et al.*, 2018; Zheng *et al.*, 2021a). Chapter 3 (Zheng *et al.*, 2021a) proposed an explicit coupled MPM in which numerical instabilities are substantially alleviated by combining selective reduced integration with a patch recovery of pore pressures based on Moving Least Square Approximation (MLSA).

This chapter presents a new fully implicit, stabilised MPM for dynamic hydromechanical problems. The proposed method builds on a three-field formulation of the underlying coupled problem, and adopts the Generalised Interpolation Material Point (GIMP) method proposed by Bardenhagen & Kober (2004) to mitigate the spurious stress oscillations associated in the original MPM with MP cell-crossing. The three-field formulation adopts equal-order interpolation for the selected primary variables, i.e., solid displacement (u), pore pressure (p), and fluid displacement (U). The resulting u–p–U formulation enables accurate analysis of slow as well as fast dynamic phenomena (Zienkiewicz & Shiomi, 1984), and has been successfully implemented/verified in FEM (Gajo *et al.*, 1994; Arduino & Macari, 2001; Jeremić *et al.*, 2008; Staubach *et al.*, 2020). In the context of FEM, the u–p–U approach has also been shown to be a generally good remedy against undrained pore pressure instabilities, although it is not always effective in 2D/3D problems when all primary unknowns are interpolated with shape functions of the lowest order (Gajo *et al.*, 1994). Since similar issues have also been experienced in MPM/GIMP calculations, the MLSA-based patch recovery proposed in Chapter 3 (Zheng *et al.*, 2021a) is incorporated in the implicit MPM presented herein, so as to improve the recovery of pore pressures to

the MPs and mitigate the effects of hydro-mechanical instabilities. The resulting *u–p–U* MPM enhanced with MLSA-based patch recovery is straightforward to implement in an implicit coupled MPM code, and also efficient owing to the use of a single set of MPs to represent both the solid and fluid phases – the alternative option of using two sets of MPs has been explored, e.g., by Soga *et al.* (2015).

The remainder of this chapter focuses on the formulation and verification of the proposed implicit MPM. Emphasis is on the verification of its accuracy under different regimes of material deformation (small versus large) and dynamic motion (slow versus fast). Special attention is also devoted to highlighting the computational convenience of implicit MPM modelling in comparison to the explicit MPM.

4.2. *u–p–U* FORMULATION OF DYNAMIC HYDROMECHANICAL PROBLEMS

THE equations governing the dynamic motion of a fully saturated porous medium are hereafter summarised following the work of Zienkiewicz and co-workers (Zienkiewicz & Shiomi, 1984; Zienkiewicz *et al.*, 1999). The momentum balance for the whole two-phase mixture prescribes that

$$\mathbf{S}^{\mathrm{T}}\boldsymbol{\sigma} - \rho\ddot{\boldsymbol{u}} - \rho_w\ddot{\boldsymbol{u}}_r + \rho\boldsymbol{b} = \mathbf{0} \tag{4.1}$$

where $\mathbf{S}$ is a differential divergence operator defined for 2D problems as (Zienkiewicz *et al.*, 1999)

$$\mathbf{S} = \begin{bmatrix} \frac{\partial}{\partial x} & 0 \\ 0 & \frac{\partial}{\partial y} \\ \frac{\partial}{\partial y} & \frac{\partial}{\partial x} \end{bmatrix} \tag{4.2}$$

while $\boldsymbol{u}$, $\boldsymbol{u}_r$, and $\boldsymbol{b}$ denote the absolute displacement of the soil skeleton, the displacement of the water phase relative to the solid phase, and an external body acceleration field, respectively. Following Zienkiewicz & Shiomi (1984), the relative water displacement is defined as $\boldsymbol{u}_r = n(\boldsymbol{U} - \boldsymbol{u})$, where $\boldsymbol{U}$ is the absolute displacement of the water phase.

To ensure the equilibrium of the mixture and its individual phases, the following momentum balance equation for the pore water must also be fulfilled:

$$\nabla p - \boldsymbol{R} - \rho_w\ddot{\boldsymbol{u}} - \rho_w\frac{\ddot{\boldsymbol{u}}_r}{n} + \rho_w\boldsymbol{b} = \mathbf{0} \tag{4.3}$$

where $\boldsymbol{R}$ is the drag force exchanged by the soil skeleton and the pore water due to their relative motion. $\boldsymbol{R}$ is proportional to the relative discharge velocity $\dot{\boldsymbol{u}}_r = n\left(\dot{\boldsymbol{U}} - \dot{\boldsymbol{u}}\right)$ according to Darcy's law:

$$\boldsymbol{R} = \frac{n\rho_w g}{k}\left(\dot{\boldsymbol{U}} - \dot{\boldsymbol{u}}\right) \tag{4.4}$$

in which the hydraulic conductivity k is assumed to be isotropic for simplicity, and g is the gravitational acceleration. It should be noted that convective terms are neglected in Equations (4.1) and (4.3) (Zienkiewicz *et al.*, 1999).

The flow of pore water must also obey the following mass conservation equation:

$$\nabla \cdot \dot{\boldsymbol{u}}_r + \nabla \cdot \dot{\boldsymbol{u}} + \frac{\dot{p}}{Q} = \mathbf{0} \tag{4.5}$$

The stiffness constant Q in Equation (4.5) is defined as $1/Q = n/K_w + (1-n)/K_s$, where K_w and K_s are the bulk moduli of the water phase and soil particles, respectively.

The use of $\boldsymbol{u}$, p, and $\boldsymbol{U}$ (in lieu of $\boldsymbol{u}_r$) as primary variables in Equations (4.1), (4.3) and (4.5) gives rise to a u–p–U dynamic coupled formulation. Therefore, each node in the background mesh is associated with, for 2D plane strain problems, five unknown degrees of freedom, i.e., two soil displacement components for the solid and the fluid phases and one pore pressure variable.

Given the focus of this work on the first implementation/verification of a new implicit MPM, the case of a linear elastic solid phase is exclusively considered in what follows. Accordingly, the constitutive relationship between effective stress ($\dot{\boldsymbol{\sigma}}'$) and strain ($\dot{\boldsymbol{\varepsilon}}$) rates can be expressed as

$$\dot{\boldsymbol{\sigma}}' = \mathbf{D}^e \dot{\boldsymbol{\varepsilon}} \tag{4.6}$$

where the elastic stiffness matrix of the solid skeleton ($\mathbf{D}^e$) is used in combination with a linearised/infinitesimal definition of the strain rate (González Acosta *et al.*, 2021; Tran & Sołowski, 2019; Zheng *et al.*, 2021a). It is known that the MPM suffers from numerical oscillations when considering large deformation analysis (González Acosta *et al.*, 2017, 2020; Zheng *et al.*, 2021a). In this work, the main focus lies in the numerical implementation of an implicit time integration algorithm and the corresponding validation of its hydromechanical performance. Fully general modelling of large deformations can be achieved by adopting well-established finite strain measures (Holzapfel, 2000) – such an extension would not be expected to heavily impact the hydromechanical performance of the proposed method.

With reference to a fully saturated porous medium, the boundary conditions for soil/water displacement and pore pressure are all of a Dirichlet type in the considered three-field formulation:

$$\boldsymbol{u}(\boldsymbol{x}, t) = \tilde{\boldsymbol{u}}(t) \quad \text{on} \quad \Gamma_u(t) \tag{4.7a}$$

$$\boldsymbol{U}(\boldsymbol{x}, t) = \tilde{\boldsymbol{U}}(t) \quad \text{on} \quad \Gamma_U(t) \tag{4.7b}$$

$$\boldsymbol{p}(\boldsymbol{x}, t) = \tilde{\boldsymbol{p}}(t) \quad \text{on} \quad \Gamma_p(t) \tag{4.7c}$$

where $\tilde{\boldsymbol{u}}(t)$, $\tilde{\boldsymbol{U}}(t)$, and $\tilde{\boldsymbol{p}}(t)$ are the prescribed boundary values – possibly varying in time – of the soil and water displacements, and pore pressures, respectively. Conversely, a (total) surface traction is represented as a Neumann boundary condition:

$$\boldsymbol{\sigma}(\mathbf{x}, t) \cdot \mathbf{G}_\tau = \tilde{\boldsymbol{\tau}}(t) \quad \text{on} \quad \Gamma_\tau(t) \tag{4.8a}$$

where $\mathbf{G}_\tau$ is a matrix containing components of the unit vector normal to the boundary surface Γ (Zienkiewicz *et al.*, 1999), and $\tilde{\boldsymbol{\tau}}(t)$ is a prescribed surface traction vector.

The modelling of impermeable boundaries requires the enforcement of nil (components of) soil–water relative velocity ($\dot{\boldsymbol{u}}_r$) along certain spatial directions. Such a condition is easily fulfilled in the verification examples presented in Section 4.4, where cases with impermeable boundaries that are also kinematically constrained are exclusively considered (i.e., $\boldsymbol{u}_{x\,\text{and/or}\,y} = \mathbf{0}$): therefore, imposing $\boldsymbol{u}_{x\,\text{and/or}\,y} = \boldsymbol{U}_{x\,\text{and/or}\,y} = \mathbf{0}\,\forall\, t$ also automatically fulfills the impermeability requirement in terms of relative velocity.

4.3. NUMERICAL IMPLEMENTATION OF IMPLICIT GIMP-PATCH METHOD

THIS section provides relevant technical details regarding the numerical formulation and implementation of the implicit GIMP-patch method proposed in this study. In particular, spatial discretisation, time integration, and mitigation of numerical instabilities are discussed.

4.3.1. SPATIAL DISCRETISATION

The primary variables $\boldsymbol{u}$, p, and $\boldsymbol{U}$ are first approximated using their nodal values ($\bar{\boldsymbol{u}}$, $\bar{\boldsymbol{p}}$, and $\bar{\boldsymbol{U}}$) in the background mesh:

$$\boldsymbol{u} = \mathbf{N}_u \bar{\boldsymbol{u}}, \qquad p = \boldsymbol{N}_p \bar{\boldsymbol{p}}, \qquad \boldsymbol{U} = \mathbf{N}_U \bar{\boldsymbol{U}} \tag{4.9}$$

where $\mathbf{N}_u$, $\boldsymbol{N}_p$, and $\mathbf{N}_U$ are matrices containing shape functions of the same low order (bilinear in 2D problems) for the interpolation of solid displacements, pore pressures, and fluid displacements, respectively. Substituting the above approximations (Equation (4.9)) into the weak forms of the governing equations ((4.1), (4.3) and (4.5)) leads to the following discrete system of ordinary differential equations:

$$\begin{bmatrix} \mathbf{M}_u & \mathbf{0} & \mathbf{0} \\ \mathbf{0} & \mathbf{0} & \mathbf{0} \\ \mathbf{0} & \mathbf{0} & \mathbf{M}_U \end{bmatrix} \begin{bmatrix} \ddot{\bar{\boldsymbol{u}}} \\ \ddot{\bar{\boldsymbol{p}}} \\ \ddot{\bar{\boldsymbol{U}}} \end{bmatrix} + \begin{bmatrix} \mathbf{C}_1 & \mathbf{0} & -\mathbf{C}_2 \\ \mathbf{0} & \mathbf{0} & \mathbf{0} \\ -\mathbf{C}_2^{\mathrm{T}} & \mathbf{0} & \mathbf{C}_3 \end{bmatrix} \begin{bmatrix} \dot{\bar{\boldsymbol{u}}} \\ \dot{\bar{\boldsymbol{p}}} \\ \dot{\bar{\boldsymbol{U}}} \end{bmatrix} + \begin{bmatrix} \mathbf{K}_u & -\mathbf{G}_1 & \mathbf{0} \\ -\mathbf{G}_1^{\mathrm{T}} & \mathbf{P} & -\mathbf{G}_2^{\mathrm{T}} \\ \mathbf{0} & -\mathbf{G}_2 & \mathbf{0} \end{bmatrix} \begin{bmatrix} \bar{\boldsymbol{u}} \\ \bar{\boldsymbol{p}} \\ \bar{\boldsymbol{U}} \end{bmatrix} = \begin{bmatrix} \bar{\boldsymbol{f}}_s \\ \mathbf{0} \\ \bar{\boldsymbol{f}}_w \end{bmatrix} \tag{4.10}$$

where: $\mathbf{M}_u$ and $\mathbf{M}_U$ are mass matrices for the soil and water phases; $\mathbf{C}_1$, $\mathbf{C}_2$, and $\mathbf{C}_3$ are damping matrices physically associated with grain–fluid drag; $\mathbf{K}_u$ is the stiffness matrix of the solid skeleton; $\mathbf{P}$ is a compressibility matrix determined by the bulk stiffness of the solid grains and pore water; and $\mathbf{G}_1$ and $\mathbf{G}_2$ are two matrices describing the hydromechanical coupling between the skeleton deformation and pore water flow. The expressions for the matrices emerging from the spatial discretisation process are as follows (Zienkiewicz & Shiomi, 1984):

$$\begin{aligned}
\mathbf{M}_u &= \int_\Omega \mathbf{N}_u^{\mathrm{T}} (1-n)\, \rho_s \mathbf{N}_u \mathrm{d}\Omega & \mathbf{M}_U &= \int_\Omega \mathbf{N}_U^{\mathrm{T}} n \rho_w \mathbf{N}_U \mathrm{d}\Omega \\
\mathbf{C}_1 &= \int_\Omega \mathbf{N}_u^{\mathrm{T}} n^2 k^{-1} \mathbf{N}_u \mathrm{d}\Omega & \mathbf{C}_2 &= \int_\Omega \mathbf{N}_u^{\mathrm{T}} n^2 k^{-1} \mathbf{N}_U \mathrm{d}\Omega \\
\mathbf{C}_3 &= \int_\Omega \mathbf{N}_U^{\mathrm{T}} n^2 k^{-1} \mathbf{N}_U \mathrm{d}\Omega & \mathbf{K}_u &= \int_\Omega \mathbf{B}_u^{\mathrm{T}} \mathbf{D}^e \mathbf{B}_u \mathrm{d}\Omega \\
\mathbf{G}_1 &= \int_\Omega \mathbf{B}_u^{\mathrm{T}} \mathbf{m} (1-n) \mathbf{N}_p \mathrm{d}\Omega & \mathbf{G}_2 &= \int_\Omega \mathbf{B}_U^{\mathrm{T}} \mathbf{m} n \mathbf{N}_p \mathrm{d}\Omega \\
\mathbf{P} &= \int_\Omega \boldsymbol{N}_p^{\mathrm{T}} \frac{1}{Q} \boldsymbol{N}_p \mathrm{d}\Omega
\end{aligned} \tag{4.11}$$

where $\mathbf{B}_u$ and $\mathbf{B}_U$ are compatibility matrices containing spatial derivatives of the shape functions. The nodal force vectors in Equation (4.10), $\bar{\boldsymbol{f}}_s$ and $\bar{\boldsymbol{f}}_w$, relate to external body

forces and surface tractions:

$$\bar{\boldsymbol{f}}_s = \int_{\Gamma_\tau} \mathbf{N}_u^{\mathrm{T}} \bar{\boldsymbol{\tau}}(t) \mathrm{d}\Gamma_\tau + \int_\Omega \mathbf{N}_u^{\mathrm{T}} (1-n)\, \rho_s b \mathrm{d}\Omega \tag{4.12a}$$

$$\bar{\boldsymbol{f}}_w = \int_\Omega \mathbf{N}_U^{\mathrm{T}} n \rho_w \boldsymbol{b} \mathrm{d}\Omega \tag{4.12b}$$

In regular MPM, $\mathbf{N}_u$, $\mathbf{N}_U$ and $\boldsymbol{N}_p$ would feature the same (bi)linear shape functions as in standard FEM. It is well known, however, that regular MPM may suffer from stress oscillations when MPs cross grid cell boundaries due to discontinuous shape function gradients. GIMP was proposed by Bardenhagen & Kober (2004) to reduce such oscillations, with the shape functions $S_i(x)$ being constructed by integrating linear FEM shape functions $N_i(x)$ over the MP support domain Ω_{mp}.

In the framework of GIMP, the matrices in Equation (4.10) are redefined for a specific grid cell node as follows:

$$\mathbf{M}_{u,i} = \sum_{mp=1}^{N_{mp}} \mathbf{S}_{u,i}^{\mathrm{T}}(\boldsymbol{x}_{mp}) m_{u,mp} \mathbf{S}_{u,i}(\boldsymbol{x}_{mp}) = \sum_{mp=1}^{N_{mp}} \mathbf{S}_{u,i}^{\mathrm{T}}(\boldsymbol{x}_{mp})(1-n)\rho_{s,mp} V_{mp} \mathbf{S}_{u,i}(\boldsymbol{x}_{mp}) \tag{4.13a}$$

$$\mathbf{M}_{U,i} = \sum_{mp=1}^{N_{mp}} \mathbf{S}_{U,i}^{\mathrm{T}}(\boldsymbol{x}_{mp}) m_{U,mp} \mathbf{S}_{U,i}(\boldsymbol{x}_{mp}) = \sum_{mp=1}^{N_{mp}} \mathbf{S}_{U,i}^{\mathrm{T}}(\boldsymbol{x}_{mp}) n \rho_{w,mp} V_{mp} \mathbf{S}_{U,i}(\boldsymbol{x}_{mp}) \tag{4.13b}$$

$$\mathbf{C}_{1,i} = \sum_{mp=1}^{N_{mp}} \mathbf{S}_{u,i}^{\mathrm{T}}(\boldsymbol{x}_{mp}) n^2 k^{-1} \mathbf{S}_{u,i}(\boldsymbol{x}_{mp}) V_{mp} \tag{4.13c}$$

$$\mathbf{C}_{2,i} = \sum_{mp=1}^{N_{mp}} \mathbf{S}_{u,i}^{\mathrm{T}}(\boldsymbol{x}_{mp}) n^2 k^{-1} \mathbf{S}_{U,i}(\boldsymbol{x}_{mp}) V_{mp} \tag{4.13d}$$

$$\mathbf{C}_{3,i} = \sum_{mp=1}^{N_{mp}} \mathbf{S}_{U,i}^{\mathrm{T}}(\boldsymbol{x}_{mp}) n^2 k^{-1} \mathbf{S}_{U,i}(\boldsymbol{x}_{mp}) V_{mp} \tag{4.13e}$$

$$\mathbf{K}_{u,i} = \sum_{mp=1}^{N_{mp}} \nabla \mathbf{S}_{u,i}^{\mathrm{T}}(\boldsymbol{x}_{mp}) \mathbf{D}^e \nabla \mathbf{S}_{u,i}(\boldsymbol{x}_{mp}) V_{mp} = \sum_{mp=1}^{N_{mp}} \mathbf{B}_{u,i}^{\mathrm{T}}(\boldsymbol{x}_{mp}) \mathbf{D}^e \mathbf{B}_{u,i}(\boldsymbol{x}_{mp}) V_{mp} \tag{4.13f}$$

$$\mathbf{G}_{1,i} = \sum_{mp=1}^{N_{mp}} \nabla \mathbf{S}_{u,i}^{\mathrm{T}}(\boldsymbol{x}_{mp}) \boldsymbol{m}(1-n) S_{p,i}(\boldsymbol{x}_{mp}) V_{mp} = \sum_{mp=1}^{N_{mp}} \mathbf{B}_{u,i}^{\mathrm{T}}(\boldsymbol{x}_{mp}) \boldsymbol{m}(1-n) S_{p,i}(\boldsymbol{x}_{mp}) V_{mp} \tag{4.13g}$$

$$\mathbf{G}_{2,i} = \sum_{mp=1}^{N_{mp}} \nabla \mathbf{S}_{U,i}^{\mathrm{T}}(\boldsymbol{x}_{mp}) \boldsymbol{m} n S_{p,i}(\boldsymbol{x}_{mp}) V_{mp} = \sum_{mp=1}^{N_{mp}} \mathbf{B}_{U,i}^{\mathrm{T}}(\boldsymbol{x}_{mp}) \boldsymbol{m} n S_{p,i}(\boldsymbol{x}_{mp}) V_{mp} \tag{4.13h}$$

$$P_i = \sum_{mp=1}^{N_{mp}} S_{p,i}^{\mathrm{T}}(\boldsymbol{x}_{mp}) \frac{1}{Q} S_{p,i}(\boldsymbol{x}_{mp}) V_{mp} \tag{4.13i}$$

where the subscript i defines the i^{th} grid cell node, $\boldsymbol{x}_{mp}$ are the coordinates of the MPs, and N_{mp} is the total number of MPs. Similarly, the external force vectors in Equation

(4.12) are re-written as

$$\bar{\boldsymbol{f}}_{s,i} = \sum_{mp=1}^{N_{bmp}} \mathbf{S}_{u,i}^{\mathrm{T}}(\boldsymbol{x}_{mp})\bar{\boldsymbol{\tau}}(t) + \sum_{mp=1}^{N_{bmp}} \mathbf{S}_{u,i}^{\mathrm{T}}(\boldsymbol{x}_{mp}) m_{u,mp}\boldsymbol{b} \tag{4.14a}$$

$$\bar{\boldsymbol{f}}_{w,i} = \sum_{mp=1}^{N_{bmp}} \mathbf{S}_{u,i}^{\mathrm{T}}(\boldsymbol{x}_{mp}) m_{U,mp}\boldsymbol{b} \tag{4.14b}$$

The full set of governing equations after spatial discretisation can be globally represented in the following compact form:

$$\mathbf{M}\boldsymbol{a} + \mathbf{C}\boldsymbol{v} + \mathbf{K}\boldsymbol{d} = \bar{\boldsymbol{f}} \tag{4.15}$$

where: $\mathbf{M}$, $\mathbf{C}$, and $\mathbf{K}$ are the generalised mass, damping, and stiffness matrices, respectively; $\bar{\boldsymbol{f}}$ is a time-varying external load term; and $\boldsymbol{a} = \left[\ddot{\bar{\boldsymbol{u}}}, \ddot{\bar{\boldsymbol{p}}}, \ddot{\bar{\boldsymbol{U}}}\right]^{\mathrm{T}}$, $\boldsymbol{v} = \left[\dot{\bar{\boldsymbol{u}}}, \dot{\bar{\boldsymbol{p}}}, \dot{\bar{\boldsymbol{U}}}\right]^{\mathrm{T}}$, and $\boldsymbol{d} = \left[\bar{\boldsymbol{u}}, \bar{\boldsymbol{p}}, \bar{\boldsymbol{U}}\right]^{\mathrm{T}}$ are the generalised nodal displacement, velocity, and acceleration vectors, respectively.

4.3.2. TIME INTEGRATION

The time integration of Equation (4.15) is performed using the well-established Newmark algorithm (Newmark, 1959). It is worth recalling that, in MPM computations, the problem domain is discretised into a set of MPs that carry relevant information (i.e., about mass, volume, velocity, acceleration, strain, stress), while the underlying governing equations are solved at the background grid cell nodes. Given the problem solution at the MPs for an arbitrary time step n, the corresponding variables are first mapped to the grid nodes in terms of nodal vectors of (generalised) acceleration $\boldsymbol{a}_n$, velocity $\boldsymbol{v}_n$, and displacement $\boldsymbol{d}_n$, and then the global set of discrete governing equations are solved for the subsequent step $n+1$. In compliance with Newmark's time integration and the GIMP shape functions, the nodal values of the following variables are calculated at step n as

$$m_{\alpha,i}^{n} = \sum_{mp=1}^{N_{mp}} S_{\alpha,i}(\boldsymbol{x}_{mp,n}) m_{\alpha,mp} \quad (\alpha = u, U) \tag{4.16a}$$

$$\boldsymbol{v}_{\alpha,i}^{n} = \frac{\sum_{mp=1}^{N_{mp}} S_{\alpha,i}(\boldsymbol{x}_{mp,n}) m_{\alpha,mp}\boldsymbol{v}_{\alpha,mp}}{m_{\alpha,i}^{n}} \quad (\alpha = u, U) \tag{4.16b}$$

$$\boldsymbol{a}_{\alpha,i}^{n} = \frac{\sum_{mp=1}^{N_{mp}} S_{\alpha,i}(\boldsymbol{x}_{mp,n}) m_{\alpha,mp}\boldsymbol{a}_{\alpha,mp}}{m_{\alpha,i}^{n}} \quad (\alpha = u, U) \tag{4.16c}$$

where: the subscript α indicates either the solid ($\alpha = u$) or water ($\alpha = U$) phase; the subscripts i and mp stand for the i^{th} grid node and the mp^{th} MP, respectively; the superscript and subscript n is associated with the n^{th} time step; and $m_{\alpha,i}$, $\boldsymbol{v}_{\alpha,i}$, and $\boldsymbol{a}_{\alpha,i}$ are the generalised nodal mass, velocity, and acceleration, respectively, which can be used to determine the global vectors $\boldsymbol{v}_n$ and $\boldsymbol{a}_n$. Since the background mesh is reset to

its original position at the end of each calculation step, the vector $\boldsymbol{d}_n$ is always entirely populated by nil entries (i.e., $\boldsymbol{d}_n = \mathbf{0}$).

The Newmark algorithm adopts two time integration parameters, γ and β, in the corresponding recurrence relations for stepping from n to $n+1$ (Hughes, 1987):

$$\boldsymbol{a}_{n+1} = \boldsymbol{a}_n + \Delta\boldsymbol{a} \tag{4.17a}$$

$$\boldsymbol{v}_{n+1} = \boldsymbol{v}_n + \Delta t\left[\left(1-\gamma\right)\boldsymbol{a}_n + \gamma\boldsymbol{a}_{n+1}\right] \tag{4.17b}$$

$$\boldsymbol{d}_{n+1} = \boldsymbol{d}_n + \boldsymbol{v}_n\Delta t + \frac{\Delta t^2}{2}\left[\left(1-2\beta\right)\boldsymbol{a}_n + 2\beta\boldsymbol{a}_{n+1}\right] \tag{4.17c}$$

in which $\Delta t = t_{n+1} - t_n$ is the time step size. Substituting Equation (5.8c) into Equation (5.8a) and Equation (5.8b), the recurrence relations for the acceleration $\boldsymbol{a}_{n+1}$ and the velocity $\boldsymbol{v}_{n+1}$ can be rewritten as

$$\boldsymbol{a}_{n+1} = \frac{f_1}{\Delta t^2}\left(\boldsymbol{d}_{n+1} - \boldsymbol{d}_n\right) - \frac{f_1}{\Delta t}\boldsymbol{v}_n - \left(\frac{f_1}{2} - 1\right)\boldsymbol{a}_n \tag{4.18a}$$

$$\boldsymbol{v}_{n+1} = \frac{f_2}{\Delta t}\left(\boldsymbol{d}_{n+1} - \boldsymbol{d}_n\right) - \left(f_2 - 1\right)\boldsymbol{v}_n - \left(\frac{f_2}{2} - 1\right)\boldsymbol{a}_n\Delta t \tag{4.18b}$$

where $f_1 = 1/\beta$ and $f_2 = \gamma/\beta$. In the case of linear elastodynamics, Newmark time integration is unconditionally stable, non-dissipative, and second-order accurate when $\beta = 0.25$ and $\gamma = 0.5$, which is the sole parameter pair considered in the remainder of this study. The final algebraic system of fully discretised equations, after substituting Equations (4.18a)–(4.18b) into Equation (4.15), is

$$\overline{\mathbf{K}}\Delta\boldsymbol{d}_{n+1} = \bar{\boldsymbol{f}}_{n+1} - \boldsymbol{f}_n^{int} + \mathbf{M}_n\left[\frac{f_1}{\Delta t}\boldsymbol{v}_n + \left(\frac{f_1}{2} - 1\right)\boldsymbol{a}_n\right] + \mathbf{C}_n\left[\left(f_2 - 1\right)\boldsymbol{v}_n + \left(\frac{f_2}{2} - 1\right)\boldsymbol{a}_n\Delta t\right] \tag{4.19}$$

where $\overline{\mathbf{K}} = \dfrac{f_1}{\Delta t^2}\mathbf{M}_n + \dfrac{f_2}{\Delta t}\mathbf{C}_n + \mathbf{K}_n$ is an algorithmic dynamic stiffness matrix, and $\boldsymbol{f}_n^{int} = \left[\boldsymbol{f}_{u,n}^{int}, \boldsymbol{f}_{p,n}^{int}, \boldsymbol{f}_{U,n}^{int}\right]^{\mathrm{T}}$ is the internal nodal force vector:

$$\boldsymbol{f}_{u,i}^{int} = \sum_{mp=1}^{N_{mp}} \mathbf{B}_{u,i}^{\mathrm{T}}\left(\boldsymbol{x}_{mp,n}\right)\left[\boldsymbol{\sigma}'_{mp,n} - \left(1-n\right)\boldsymbol{m}p_{mp,n}\right]V_{mp,n} \tag{4.20a}$$

$$f_{p,i}^{int} = \sum_{mp=1}^{N_{mp}}\left[-\left(1-n\right)S_{p,i}(\boldsymbol{x}_{mp,n})\varepsilon_{vol,mp}^{u} - S_{p,i}(\boldsymbol{x}_{mp,n})\frac{p_{mp,n}}{Q} - nS_{p,i}(\boldsymbol{x}_{mp,n})\varepsilon_{v,mp}^{U}\right]V_{mp,n} \tag{4.20b}$$

$$\boldsymbol{f}_{U,i}^{int} = -\sum_{mp=1}^{N_{mp}}\mathbf{B}_{U,i}^{\mathrm{T}}\left(\boldsymbol{x}_{mp,n}\right)n\boldsymbol{m}p_{mp,n}V_{mp,n} \tag{4.20c}$$

and $\varepsilon_{vol,mp}^{u}$ and $\varepsilon_{vol,mp}^{U}$ are the volumetric strain of the soil and water phases at the mp^{th} MP.

Even in the presence of linear constitutive equations, the solution of a large deformation problem is intrinsically non-linear and must be carried out iteratively (Zhao &

Choo, 2020). For this purpose, each time step is solved in combination with a Modified Newton–Raphson iteration scheme (Zienkiewicz *et al.*, 2005). Its algorithmic description is provided in Algorithm 1, where the superscript k denotes the k^{th} iteration within a given time step out of a maximum number equal to k_{max}, $\boldsymbol{\psi}_{n+1}^{(k)}$ is the vector of nodal residuals at the k^{th} iteration ($\|\boldsymbol{\psi}_{n+1}^{(k)}\|$ is its L_2 norm), and ξ is the prescribed error tolerance – here set equal to 1.0×10^{-6}. When convergence is reached according to the prescribed error tolerance, all relevant variables are updated at the MPs using computed nodal values:

$$\boldsymbol{a}_{mp,n+1} = \sum_{i=1}^{N_{node}} \mathbf{S}_{u,i}(\boldsymbol{x}_{mp,n})\boldsymbol{a}_{i,n+1} \tag{4.21a}$$

$$\boldsymbol{v}_{mp,n+1} = \sum_{i=1}^{N_{node}} \mathbf{S}_{u,i}(\boldsymbol{x}_{mp,n})\boldsymbol{v}_{i,n+1} \tag{4.21b}$$

$$\boldsymbol{\sigma}'_{mp,n+1} = \boldsymbol{\sigma}'_{mp,n} + \mathbf{D}^e \sum_{n=1}^{N_{node}} \mathbf{B}_{u,i}(\boldsymbol{x}_{mp,n})\bar{\boldsymbol{u}}_{i,n+1} \tag{4.21c}$$

$$p_{mp,n+1} = p_{mp,n} + \sum_{n=1}^{N_{node}} S_{p,i}(\boldsymbol{x}_{mp,n})\bar{p}_{i,n+1} \tag{4.21d}$$

$$\boldsymbol{x}_{mp,n+1} = \boldsymbol{x}_{mp,n} + \sum_{n=1}^{N_{node}} \mathbf{S}_{u,i}(\boldsymbol{x}_{mp,n})\bar{\boldsymbol{u}}_{i,n+1} \tag{4.21e}$$

where N_{node} is the total number of nodes.

4.3.3. MITIGATING NUMERICAL INSTABILITIES IN COUPLED MPM

Due to its similarity to FEM, MPM can suffer from numerical instabilities when low-order interpolation is equally adopted for the all the primary variables. This is the case for (nearly) incompressible hydromechanical problems in porous media, giving rise to undesired oscillations in the pore pressure field (Belytschko *et al.*, 2013; Bathe, 2001; Chen *et al.*, 2018). Although previous FEM experience has shown the beneficial effects of a three-field u–p–U formulation, pore pressure instabilities may still arise in 2D/3D problems when the same low-order interpolation is adopted for all field variables (Gajo *et al.*, 1994). To alleviate pore pressure instabilities in coupled MPM computations, a patch recovery of pore pressure increments based on the Moving Least Square Approximation (MLSA) has been proposed in Chapter 3 (Zheng *et al.*, 2021a) in combination with an explicit coupled MPM. The same patch recovery technique is also exploited within the implicit MPM presented herein. Hence, an intermediate mapping stage is introduced, in which nodal pore pressure increments are first mapped to central Gauss integration points (GPs), instead of directly to the MPs. Such a GP-mapping operation is performed as follows:

$$\Delta p_{gp,n+1} = \sum_{n=1}^{N_n} S_{p,i}(\boldsymbol{x}_{gp,n})\bar{p}_{i,n+1} \tag{4.22}$$

where $\boldsymbol{x}_{gp}$ indicates the position of a generic central GP in the background mesh. Note that since this mapping is only performed to evaluate pore pressure increments, the computed results are found not to suffer from spurious hourglass modes (Chen *et al.*,

Algorithm 1: Modified Newton-Raphson iteration scheme for a single step

1 Assemble the algorithmic dynamic stiffness matrix $\overline{\mathbf{K}}$ using the converged solution at t_n

$$\overline{\mathbf{K}} = \frac{f_1}{\Delta t^2}\mathbf{M}_n + \frac{f_2}{\Delta t}\mathbf{C}_n + \mathbf{K}_n$$

2 **while** $k \leq k_{max}$ **do**

3 Initialise vectors of nodal (generalised) displacement $\boldsymbol{d}_{n+1}^{(k)}$, velocity $\boldsymbol{v}_{n+1}^{(k)}$, and acceleration $\boldsymbol{a}_{n+1}^{(k)}$

$$\boldsymbol{d}_{n+1}^{(k)} = \boldsymbol{d}_{n+1}^{(k-1)} = \mathbf{0}, \quad \boldsymbol{v}_{n+1}^{(k)} = \boldsymbol{v}_{n+1}^{(k-1)}, \quad \boldsymbol{a}_{n+1}^{(k)} = \boldsymbol{a}_{n+1}^{(k-1)}$$

with $\boldsymbol{d}_{n+1}^{(0)} = \boldsymbol{d}_n = \mathbf{0}$, $\boldsymbol{v}_{n+1}^{(0)} = \boldsymbol{v}_n$, and $\boldsymbol{a}_{n+1}^{(0)} = \boldsymbol{a}_n$

4 Update the acceleration and velocity predictors

$$\boldsymbol{a}_{n+1}^{(k)} = \frac{f_1}{\Delta t^2}(\boldsymbol{d}_{n+1}^{(k)} - \boldsymbol{d}_n) - \frac{f_1}{\Delta t}\boldsymbol{v}_n - (\frac{f_1}{2} - 1)\boldsymbol{a}_n$$

$$\boldsymbol{v}_{n+1}^{(k)} = \frac{f_2}{\Delta t}(\boldsymbol{d}_{n+1}^{(k)} - \boldsymbol{d}_n) - (f_2 - 1)\boldsymbol{v}_n - (\frac{f_2}{2} - 1)\boldsymbol{a}_n\Delta t$$

5 Compute the nodal residual force $\boldsymbol{\psi}_{n+1}^{(k)}$

$$\boldsymbol{\psi}_{n+1}^{(k)} = \bar{\boldsymbol{f}}_{n+1} - \boldsymbol{f}_n^{int} - \mathbf{K}\boldsymbol{d}_{n+1}^{(k)} - \mathbf{M}\boldsymbol{a}_{n+1}^{(k)} - \mathbf{C}\boldsymbol{v}_{n+1}^{(k)}$$

6 Solve the linear equation $\overline{\mathbf{K}}\Delta\boldsymbol{d}_{n+1}^{(k+1)} = \boldsymbol{\psi}_{n+1}^{(k)}$ to obtain the displacement increment $\Delta\boldsymbol{d}_{n+1}^{(k+1)}$ and update the displacement vector $\boldsymbol{d}_{n+1}^{(k+1)}$

$$\boldsymbol{d}_{n+1}^{(k+1)} = \boldsymbol{d}_{n+1}^{(k)} + \Delta\boldsymbol{d}_{n+1}^{(k+1)}$$

7 **if** $\|\boldsymbol{\psi}_{n+1}^{(k)}\| \leq \xi\|\boldsymbol{\psi}_{n+1}^{(0)}\|$ **then**

8 Update values at MPs, set $t_n = t_{n+1}$ and go to the next time step

9 **else**

10 Set $k = k + 1$ and go to Step 3 for the next iteration

11 **end**

12 **end**

Table 4.1: Hydromechanical properties of the soil–water mixture in the considered verification examples

Symbol	Example 1	Example 2	Example 3	Example 4	Example 5	Unit
E	1.0×10^4	7.5×10^5	5.0×10^6	1.0×10^3	100	kPa
ν	0.2	0.2	0.0	0.2	0.3	–
ρ_w	1000	1000	1000	1000	1000	kg/m^3
ρ_s	2650	3003	2667	2650	2650	kg/m^3
n	0.3	0.3333	0.4	0.4	0.4	–
K_w	2.2×10^6	1.0×10^7	2.0×10^6	2.2×10^6	2.2×10^6	kPa
K_s	1.0×10^{10}	1.0×10^{10}	1.0×10^{10}	1.0×10^{10}	1.0×10^{10}	kPa
k	1.0×10^{-4}	see Table 2	1.0×10^{-3} 1.0×10^{-5}	1.0×10^{-4}	1.0×10^{-4}	m/s

2018). After obtaining incremental pore pressures at the central GPs through Equation (4.22), their final recovery to the MPs is performed. Following Zienkiewicz & Zhu (1992), the pore pressure increments are evaluated at the MPs through a patch recovery stage based on a moving least squares approximation (MLSA).

4.4. NUMERICAL VERIFICATION EXAMPLES

THIS section presents the result of several verification examples to support the suitability of the proposed implicit GIMP-patch method. All numerical results have been obtained through sequential computations on a computer equipped with an Intel Xeon E5-1620, 16GB RAM and x64-based processor. The discrete system of equations (4.19) has been solved in all cases using the robust, high-performance PARDISO solver (Schenk & Gärtner, 2002) from the *Intel Math Kernel Library*, which can efficiently solve large sparse linear systems.

4.4.1. 1D COUPLED PROBLEMS WITH SMALL DEFORMATIONS

EXAMPLE 1: CONSOLIDATION OF A SOIL COLUMN

The static, small-strain 1D consolidation of a linear elastic soil column is first considered as a well-established verification example for coupled poromechanical problems (Jeremić *et al.*, 2008; Bandara & Soga, 2015). Figure 4.1a shows the geometry and associated boundary conditions for the one-dimensional consolidation model. The width (w) and initial height (H_0) of the problem domain are 0.1 m and 1.0 m, respectively. The bottom boundary has both solid and water displacements totally fixed, whereas only vertical u-U displacements are allowed along the lateral boundaries. In this boundary configuration, the drainage of pore water is only allowed through the top free surface. A vertical uniform static load p_a of 1.0 kPa is instantaneously applied at the top surface.

The MPM discretisation of the system is shown in Figure 4.1b. The model is discretised by means of 10 4-node quadrilateral grid cells (elements) of size 0.1 m × 0.1 m, with each cell initially hosting four equally-spaced MPs. The hydromechanical properties assumed for the soil–water mixture are are listed in Table 4.1. Both the new implicit GIMP-patch method and the explicit GC-SRI-patch method proposed in Chapter 3 have been tested

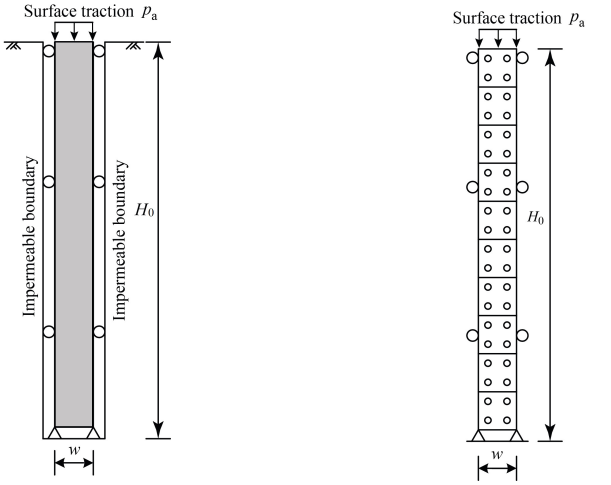

(a) Problem geometry (b) MPM discretisation

Figure 4.1: One-dimensional consolidation model

against Terzaghi's analytical solution (Terzaghi, 1943) for comparative purposes. The GIMP-patch and GC-SRI-patch results have been obtained using time-step sizes Δt of 1.0×10^{-3} s and 1.0×10^{-5} s, respectively.

Figure 4.2 compares the numerical and analytical solutions for different values of the dimensionless time factor T_v, defined as

$$T_v = \frac{c_v t}{H_v^2}$$

where H_v is the drainage path length (here equal to the thickness of the soil layer), and c_v is the coefficient of consolidation:

$$c_v = \frac{k}{\rho_w g(1/E_c + 1/Q)}$$

with $E_c = \frac{E(1-\nu)}{(1-2\nu)(1+\nu)}$ being the constrained 1D stiffness of the soil skeleton obtained as a combination of the Young's modulus E and Poisson's ratio ν. The analytical solution of the problem can be represented in terms of normalised pore pressure ($P = p/p_a$) and layer thickness ($H = H_v/H_0$) for the aforementioned boundary/initial conditions:

$$P(H, T_v) = \sum_{m=1}^{\infty} \frac{2}{M} \sin(MH) e^{-M^2 T_v} \tag{4.23}$$

where $M = (m - \frac{1}{2})\pi$. The corresponding average degree of consolidation U_s assumes the following expression:

$$U_s = 1 - \sum_{m=1}^{\infty} \frac{2}{M^2} e^{-M^2 T_v} \tag{4.24}$$

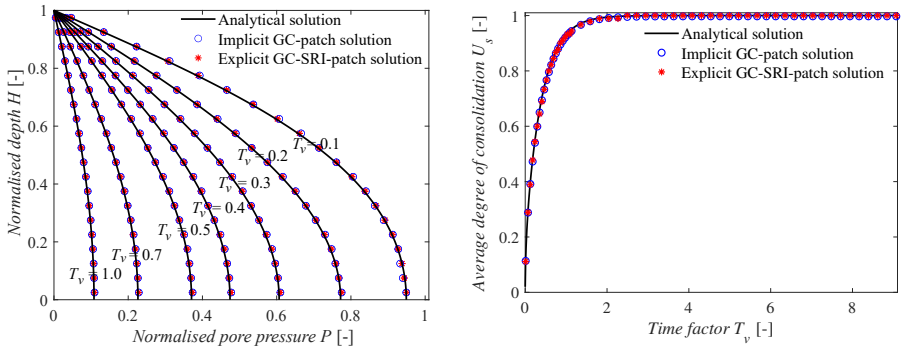

(a) Isochrones of excess normalised pore pressure

(b) Average degree of consolidation

Figure 4.2: 1D small-deformation consolidation of an elastic soil column: comparison between analytical and MPM (implicit GIMP-patch and explicit GC-SRI-patch) solutions

Figure 4.2 shows excellent agreement between the analytical and MPM solutions – both for the implicit GIMP-patch and explicit GC-SRI-patch methods. More quantitatively, Figure 4.3 displays how the relative pore pressure error (e_p) increases with the time step size both for the implicit and explicit MPMs. For a given value of the time factor T_v, the reference error measure e_p is defined over the spatial domain as follows:

$$e_p(T_v) = \frac{\sqrt{\sum_{mp=1}^{N_{mp}} \left[P^*_{mp}(T_v) - P_{mp}(T_v)\right]^2}}{N_{mp}} \tag{4.25}$$

where $P^*_{mp}(T_v)$ and $P_{mp}(T_v)$ are the analytical and numerical pore pressure solutions at the MP locations (normalised with respect to the maximum excess pore pressure, which is equal to p_a at any depth – Figure 4.1). It is apparent that e_p grows with Δt more slowly for the implicit GIMP-patch method – in a similar way for the two T_v values considered. It is also interesting to note that the implicit solution obtained with $\Delta t = 1.0 \times 10^{-3}$ s is characterised by a level of accuracy that the explicit method achieves with a Δt around 100 times smaller. This expected finding confirms the computational convenience of implicit modelling for transient problems of medium-large duration.

The gradual reduction in relative error e_p upon grid refinement is shown for $T_v = 0.5$ in Figure 4.4 – for the proposed implicit GIMP-patch method in comparison to MPM and GIMP solutions (i.e., without patch recovery of pore pressures). Due to the small settlement experienced by the soil layer in the considered example, MPM and GIMP solutions are practically coincident, and exhibit first-order convergence with respect to the number of grid cells (i.e., the ratio between the soil layer thickness and grid cell size). The implicit GIMP-patch method returns generally smaller e_p values, with a convergence rate decreasing from 2 to 1 as the problem domain is more finely discretised.

EXAMPLE 2: DYNAMIC CONSOLIDATION OF A SOIL COLUMN UNDER HARMONIC LOADING

The dynamic steady-state response of an elastic soil column to a harmonic surface load is considered as a second verification case. Specifically, the same kind of system as in Figure

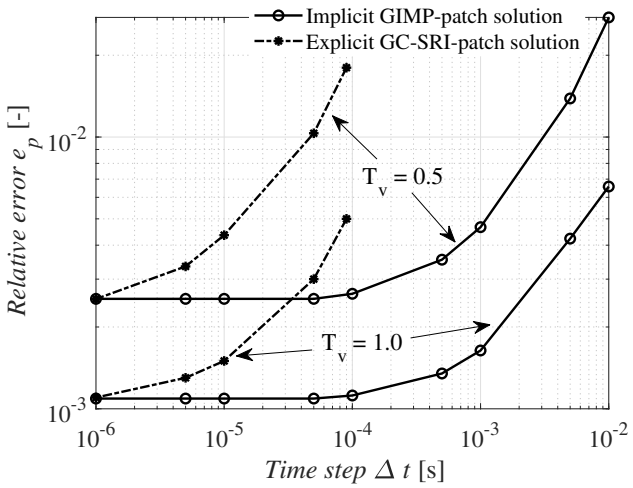

Figure 4.3: Dependence of the relative pore pressure error e_p on the step size for the considered implicit and explicit MPMs (small deformation consolidation)

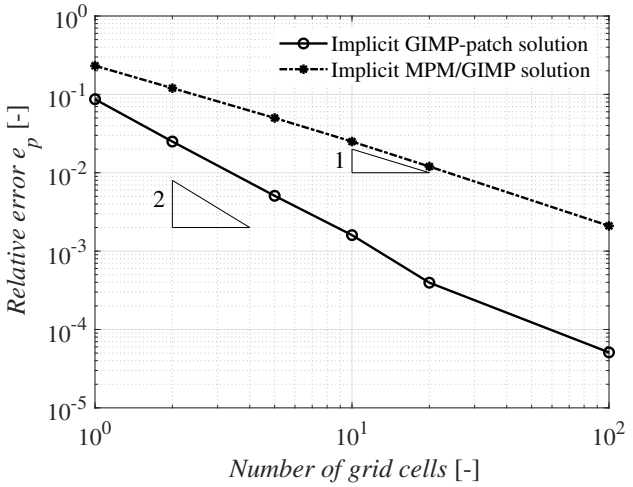

Figure 4.4: Dependence of the relative pore pressure error e_p on the grid cell size at $T_v = 0.5$ (small deformation consolidation)

4.1 is analysed in combination with a time-varying surface load, $p_a = \cos(\omega t)$, where ω is the angular frequency. This problem was first studied by Zienkiewicz *et al.* (1980), who provided an analytical solution that has served numerous numerical verification studies – even in the recent context of meshfree modelling (Navas *et al.*, 2016, 2018). In this case, the soil column width (w) and height (H_0) are 0.2 m and 10.0 m, respectively, and it has been discretised into 50 4-node quadrilateral grid cells (with a cell size equal to

0.2 m × 0.2 m). The relevant hydromechanical properties are listed in Table 4.1.

As discussed by Zienkiewicz *et al.* (1980), the dynamic steady-state response of the system spans three possible regimes of hydro-mechanical coupling (Figure 4.5), depending on the values of two relevant dimensionless factors, namely Π_1 and Π_2:

$$\Pi_1 = \frac{k V_c^2}{g \beta \omega H_0^2}, \quad \Pi_2 = \frac{\omega^2 H_0^2}{V_c^2}$$

where $V_c = \sqrt{(E_c + K_w/n)/\rho}$ is the compression wave velocity, E_c the constrained 1D modulus defined above, and $\beta = \rho_w/\rho$. In Figure 4.5, zone I is associated with slow hydromechanical phenomena, in which the role played by inertial effects is from limited to negligible. The opposite end of the spectrum is represented by Π_1-Π_2 combinations in zone III, which is associated with fast dynamic consolidation and significant relative accelerations between the solid and the water phases. Moderately fast processes take place within the intermediate zone II, where the assumption of negligible relative solid–fluid acceleration is normally acceptable. In order to verify the implicit GIMP-patch method under different consolidation regimes, seven Π_1-Π_2 pairs (P_1-P_7) have been considered – see Figure 4.5 and Table 4.2.

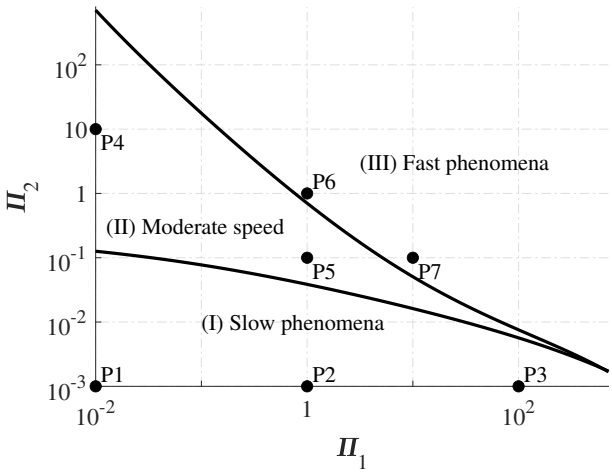

Figure 4.5: Π_1-Π_2 pairs considered in the implicit GIMP-patch simulation of dynamic consolidation – cf. Zienkiewicz *et al.* (1980)

Figure 4.6 compares analytical and GIMP-patch solutions in terms of steady-state profiles of normalised pore pressure ($P = p/p_a^{max}$). The numerical results for the seven simulation cases in Figure 4.5 have been obtained using a time step size of $\Delta t = 1.0 \times 10^{-4}$ s. No explicit GC-SRI-patch solutions have been computed in this case, due to the significant calculation time that the attainment of a harmonic steady state would require using a time step size of the order of $\Delta t = 1.0 \times 10^{-5}$ s. The numerical–analytical comparisons in Figure 4.6 confirm the suitability of the proposed MPM over the whole range of dy-

Table 4.2: Parameter specification for the Π_1-Π_2 pairs indicated in Figure 4.5

Zones	Points	Π_1	Π_2	ω [rad/s]	k [m/s]
I	P1	0.01	0.01	10.14	3.22×10^{-6}
	P2	1.00	0.01	10.14	3.22×10^{-4}
	P3	100.00	0.01	10.14	3.22×10^{-2}
II	P4	0.01	10.00	1013.78	3.22×10^{-4}
	P5	1.00	0.10	101.38	3.22×10^{-3}
III	P6	1.00	1.00	320.59	1.02×10^{-2}
	P7	10.00	0.10	101.38	3.22×10^{-2}

namic consolidation speeds, including in the presence of significant solid–fluid relative accelerations (zone III).

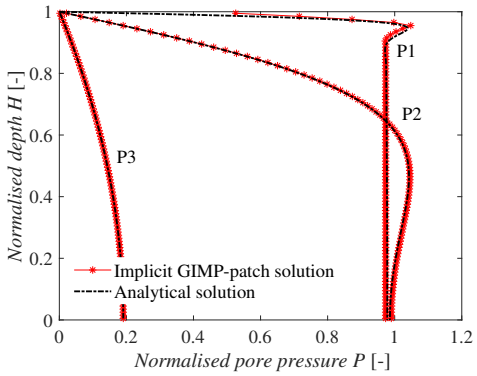

(a) Slow consolidation – zone (I) in Figure 4.5

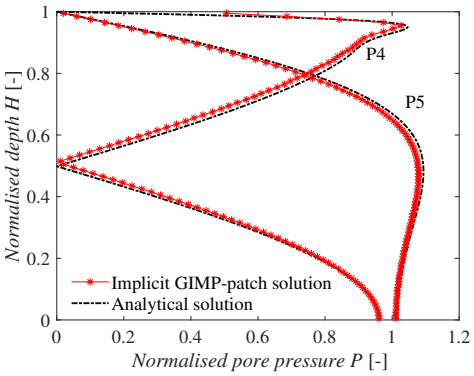

(b) Moderately fast consolidation – zone (II) in Figure 4.5

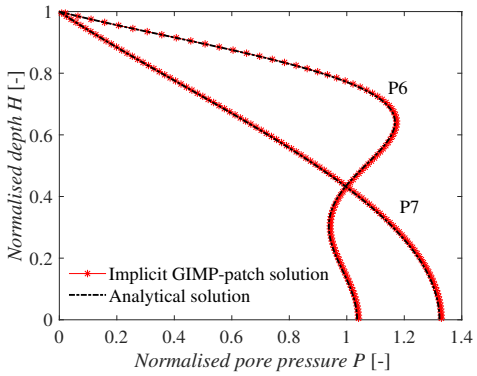

(c) Fast consolidation – zone (III) in Figure 4.5

Figure 4.6: Performance of the GIMP-patch method under different dynamic consolidation regimes

EXAMPLE 3: PROPAGATION OF A SHOCK PRESSURE WAVE

The ability of the implicit GIMP-patch method to reproduce 1D wave propagation along an elastic soil column is assessed. The same kind of boundary conditions as described in Section 4.4.1 have been considered for a soil column of width and height equal to $w = 2.5 \times 10^{-3}$ m and $H_0 = 2.5$ m, respectively. The domain is constrained along the lateral boundaries ($u_x = 0$ and $U_x = 0$) and totally fixed at the bottom boundary ($u_i = 0$ and $U_i = 0$) – as a result of such constraints, the drainage of pore water is only allowed through the top free surface. The relevant hydromechanical properties of the soil–water mixture are reported in Table 4.1 – note that the same values have been set for E_c and K_w/n, so as to obtain an equal distribution of the external load over the solid and fluid phases. Wave motion along the soil column is triggered by imposing a uniform vertical load p_a of 1.0 kPa, which is instantaneously applied and then held constant at the top of the soil column. To accurately capture the propagation of shock waves, a fine spatial discretisation is necessary. For the case under consideration, the soil column has been discretised into 1000 4-node quadrilateral grid cells with a cell size of 2.5×10^{-3} m.

For the selected material properties and applied loading conditions, two shock waves are normally generated which propagate from the top to the bottom of the column. One wave (called the undrained wave) features the synchronous motion of soil and water at the same velocity, while the two phases move asynchronously in a second wave (the damped wave) that propagates with a lower speed (Verruijt, 2009; Chmelnizkij *et al.*, 2019). The propagation velocities of the undrained (V_u) and damped (V_d) waves can be respectively calculated as

$$V_u = \sqrt{\frac{E_c + K_w/n}{\rho}} = 2236\,\text{m/s} \tag{4.26}$$

$$V_d = \sqrt{\frac{K_w}{\rho_w}} \sqrt{\frac{nE_c}{(1-n)K_w + nE_c}} = 1118\,\text{m/s} \tag{4.27}$$

To mobilise different hydromechanical coupling regimes, low and high values of the hydraulic conductivity have been considered, i.e., $k = 1.0 \times 10^{-5}$ m/s and $k = 1.0 \times 10^{-3}$ m/s. Comparative MPM solutions have been obtained using both the implicit and explicit MPMs considered so far. For the explicit method, the time step Δt needs to be smaller than the critical time step $\Delta t_{cr} = l/V_u$ (Van Esch *et al.*, 2011), which is 1.12×10^{-6} s for the reference material properties in Table 4.1. In order to achieve satisfactory accuracy in explicit calculations, a rather small time step size of $\Delta t = 6.0 \times 10^{-7}$ s has been chosen, while a larger time step of $\Delta t = 1.0 \times 10^{-6}$ s has been set for the proposed implicit method. In the latter case, such a choice is driven by accuracy rather than stability – a shock propagation problem will always require fine time stepping for rapid dynamics to be accurately captured.

Figure 4.7 illustrates both the explicit and implicit solutions in terms of normalised excess pore pressure ($P = p/p_a$) at a point 0.4 m below the top surface. In the case of a higher hydraulic conductivity (Figure 4.7a), the presence of both the undrained and damped waves can be observed despite the inevitable Gibbs oscillations (caused by the fast load application). In particular, their arrival times at the reference depth equal 1.79×10^{-4} s and 3.58×10^{-4} s, respectively, which is consistent with the theoretical

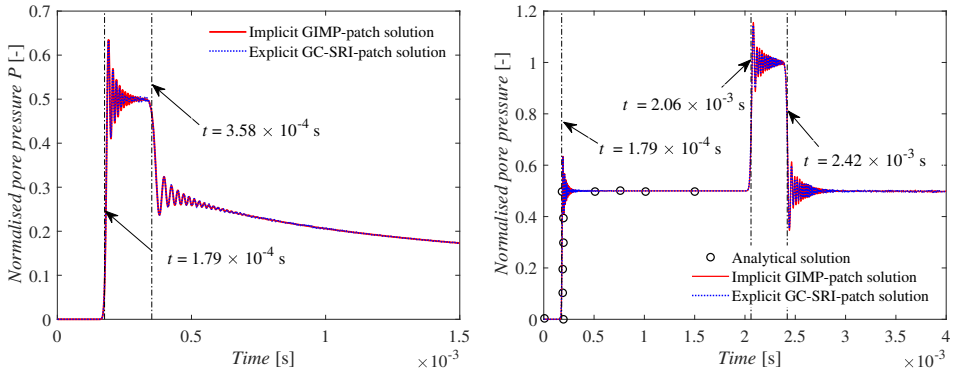

(a) High hydraulic conductivity $k = 1.0 \times 10^{-3}$ m/s

(b) Low hydraulic conductivity $k = 1.0 \times 10^{-5}$ m/s

Figure 4.7: Propagation of a shock pressure wave: comparison between analytical and MPM (implicit GIMP-patch and explicit GC-SRI-patch) solutions

propagation speeds – cf. Equations (4.26) and (4.27). As the hydraulic conductivity decreases, only the undrained wave remains visible, which is consistent with the results in Figure 4.7b (Verruijt, 2009). Also in this second case, the first arrival of the undrained wave complies with the theoretical propagation speed – arrival in 1.79×10^{-4} s; then, due to wave reflection at the fixed bottom boundary, the undrained wave passes again through the reference location at a time equal to 2.06×10^{-3} s and results in a doubling of the pore pressure magnitude. The good agreement between numerical and analytical solutions (Verruijt, 2009) further supports the overall applicability of the proposed implicit method. The high frequency oscillations that are visible in Figure 4.7 could be significantly alleviated by more gradual application of the external load, or by resorting to numerical algorithms more specifically conceived for shock wave propagation problems (Pisanò & Pastor, 2011; Blanc & Pastor, 2013).

4.4.2. EXAMPLE 4: LARGE-DEFORMATION 1D CONSOLIDATION OF A SOIL COLUMN

The case of a two-phase elastic soil column undergoing large-deformation consolidation (Gibson *et al.*, 1967; Tran & Sołowski, 2019; Zheng *et al.*, 2021a) is tackled here using the proposed implicit GIMP-patch method. It should be pointed out that this numerical example has previously been solved using explicit coupled MPMs by Tran and Sołowski (Tran & Sołowski, 2019) and Zheng et al. (Zheng *et al.*, 2021a). Both the proposed solutions using the same time step size of $\Delta t = 1.0 \times 10^{-6}$ s have been previously verified against the consolidation solution provided by Xie and Leo (Xie & Leo, 2004) based on Gibson's large deformation theory (Gibson *et al.*, 1967).

With reference to the same problem layout in Figure 4.1, an elastic soil column of respective width (w) and height (H_0) equal to 0.1 m and 1.0 m is considered. The problem domain is discretised into 10 4-node quadrilateral grid cells of size 0.1 m × 0.1 m, while the relevant hydromechanical material properties of the mixture are given in Table 4.1.

The boundary conditions are exactly the same as shown in Figure 4.1, and an instant external loading $p_a = 200.0\,\text{kPa}$ is applied as a surface compression. The time step size Δt for the proposed implicit MPM is chosen as $1.0 \times 10^{-4}\,\text{s}$, which is 100 times larger than that adopted for explicit calculations (Tran & Sołowski, 2019; Zheng *et al.*, 2021a).

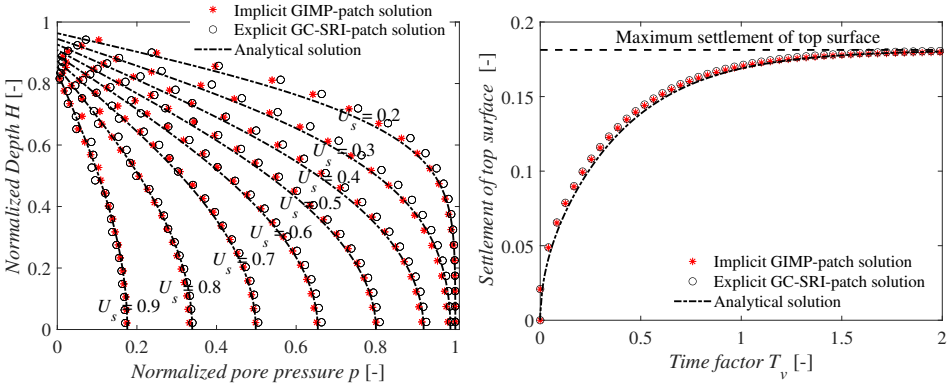

(a) Excess pore pressure isochrones

(b) Settlement of top surface

Figure 4.8: Comparison between implicit GIMP-patch, explicit GC-SRI-patch and analytical consolidation solutions – large deformation analysis

Figure 4.8 shows the comparison between the implicit GIMP-patch, explicit GC-SRI-patch, and analytical solutions in terms of excess pore pressure and settlement of top surface. It is clear that that the two MPM solutions compare well with each other and also match with the analytical large-deformation solution. However, slight oscillations in pore pressure can still be observed from both implicit and explicit solutions near the upper domain surface. Such oscillations are arguably caused by the small nodal mass issue (Ma *et al.*, 2010) and cell crossing that frequently occur during the settlement of the column top surface.

The behaviour of the implicit GIMP-patch method upon grid refinement is also examined in the presence of (1D) large deformations. As an example, Figure 4.9 displays the dependence of the relative pore pressure error e_p (computed using Equation (4.25)) on the grid cell size at $U_s = 0.5$ (i.e., 50 % of consolidation). Similarly to the small deformation consolidation case (Figure 4.4), the order of convergence varies from 2 to 1 upon progressive grid refinement. The reduction in the convergence order for this large deformation consolidation problem can be attributed to the fact that a larger group of material points will be crossing the cell edges, which can cause additional errors that weaken the benefit of the proposed MLSA-based patch recovery. Similar observations and conclusions also can be found in the previous work of Charlton et al. (Charlton *et al.*, 2017).

4.4.3. EXAMPLE 5: 2D SLUMPING BLOCK

The 2D consolidation of an elastic slumping block is analysed as a final case – see also Zhao & Choo (2020) and Chapter 3 (Zheng *et al.*, 2021a). The width and depth of the block are 4.0 m and 2.0 m, respectively. Taking advantage of symmetry, only the right half of the problem domain is considered, as is shown in Figure 4.10 together with the domain

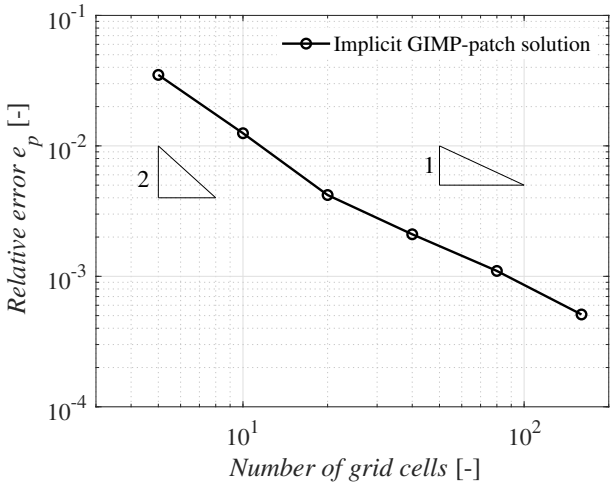

Figure 4.9: Dependence of the relative pore pressure error e_p on the grid cell size at $U_s = 0.5$ (large deformation consolidation)

boundary conditions and applied gravitational acceleration ramp. For comparison purposes, the same material properties as adopted in Chapter 3 for the same problem have been retained – see Table 4.1. The problem domain has been discretised using 16×16, 4-node quadrilateral grid cells of size $0.125\,\text{m} \times 0.125\,\text{m}$. Implicit GIMP-patch simulations have been performed using a time step size equal to $\Delta t = 1.0 \times 10^{-3}\,\text{s}$.

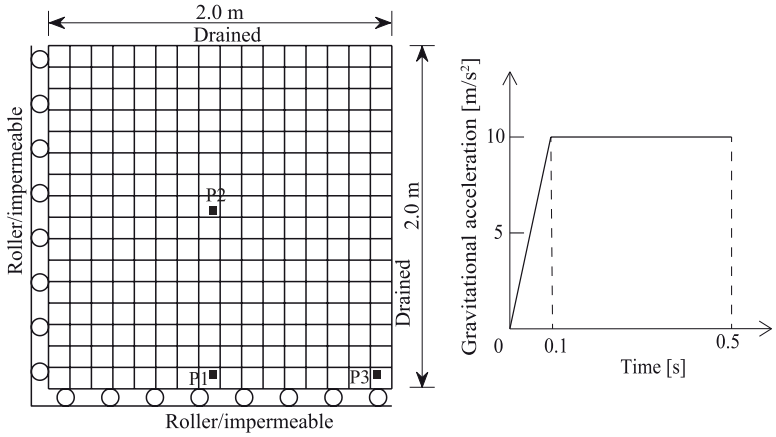

Figure 4.10: Layout of the 2D slumping block problems and corresponding application ramp for the gravitational acceleration

To further highlight the stabilisation benefits of the patch recovery, the above problem has been solved using two versions of the proposed implicit MPM, namely GIMP and GIMP-patch – i.e., with the former using no patch recovery of pore pressures. Figure 4.11

shows the excess pore pressure field at $t = 0.18\,\text{s}$ resulting from both methods. Notwithstanding the underlying three-field formulation, the implicit GIMP (with equal-order interpolation) still produces a checkerboard pore pressure pattern when no patch recovery is performed, which is consistent with the observations of Gajo *et al.* (1994). Such a pattern becomes increasingly pronounced as time elapses, and causes a sudden abortion of the GIMP simulation at approximately $t = 0.21\,\text{s}$. In contrast, the numerical solution obtained using the proposed MLSA-based patch recovery is completely oscillation-free throughout the whole duration of the analysis.

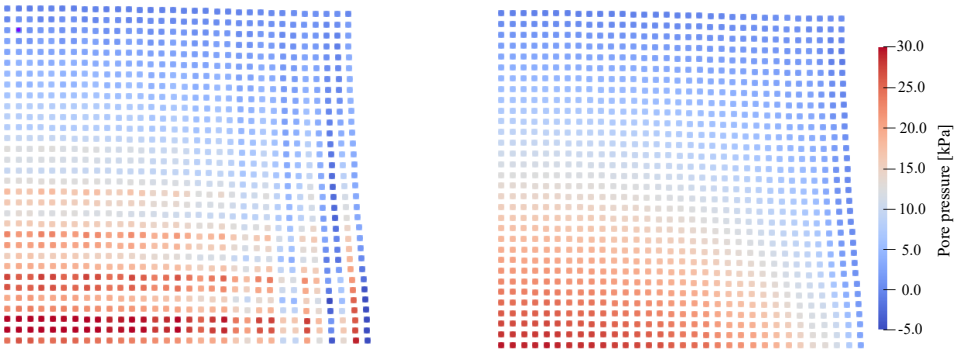

(a) Implicit GIMP method

(b) Implicit GIMP-patch method

Figure 4.11: Excess pore pressure distributions at $t = 0.18\,\text{s}$ with implicit GIMP and GIMP-patch methods

Figure 4.12 displays the excess pore pressure fields obtained at different times ($t = 0.1$, 0.3, 0.5 s) using both the implicit GIMP-patch and explicit GC-SRI-patch methods (with a time step size of $\Delta t = 1.0 \times 10^{-5}\,\text{s}$). For further comparison, the time evolution of the excess pore pressure at three selected points (P1, P2 and P3 in Figure 4.10) is also shown in Figure 4.13. As expected, a build-up in pore pressure occurs during the gravitational ramp, whereas the following pressure dissipation develops non-monotonically due to the so-called Mandel–Cryer effect (Mandel, 1953; Cryer, 1963) – see Figures 4.12 and 4.13. Both methods provide very comparable solutions for the same problem, with smooth/stable pore pressure fields obtained in both cases. Similar conclusions regarding the mutual verification of the two methods are suggested by Figure 4.14 in terms of the final displacement field (vector norm of the solid displacement at $t = 0.5\,\text{s}$). The comparison with the results returned by the explicit method in Chapter 3 supports the overall suitability of the proposed implicit GIMP-patch method, which can be used to solve transient hydromechanical problems with large time steps.

4.4.4. CALCULATION TIME

To compare in more detail the computational performance of the two considered MPMs, selected time steps (giving the same order of accuracy) and associated calculation times (CT) are reported in Table 4.3 for verification examples 1, 4, and 5. Note that the implicit and explicit time steps used for the 1D small-deformation consolidation benchmark

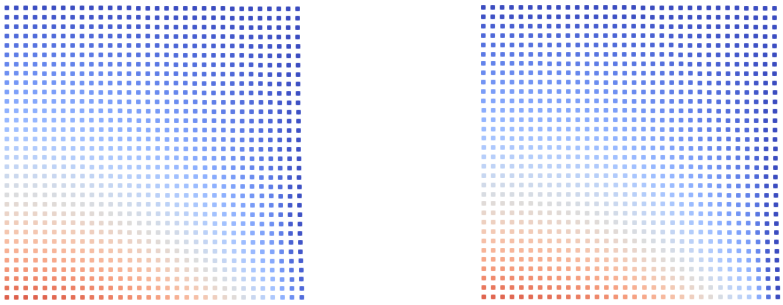

(a) Implicit (left) and explicit (right) solutions at $t = 0.1\,\mathrm{s}$

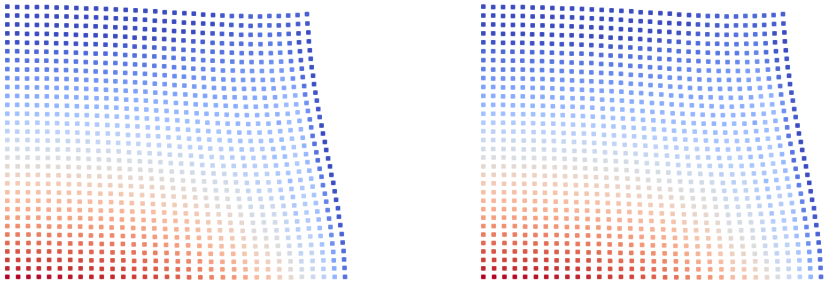

(b) Implicit (left) and explicit (right) solutions at $t = 0.3\,\mathrm{s}$

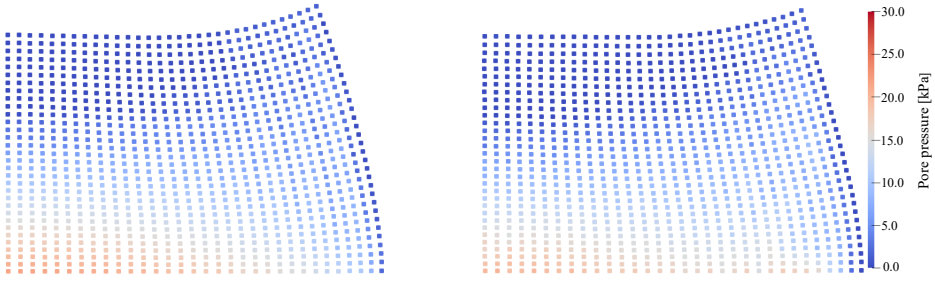

(c) Implicit (left) and explicit (right) solutions at $t = 0.5\,\mathrm{s}$

Figure 4.12: Excess pore pressure field at different times obtained for a 2D slumping block using the implicit GIMP-patch method (left) and explicit GC-SRI-patch method (right)

(Example 1 in Section 4.1.1) have been selected based on a dedicated sensitivity study (see Figure 4.3) and re-adopted to solve the 2D slumping block problem (Example 5 in Section 4.3). A coarser background mesh was employed for the 1D large-deformation consolidation problem (Example 4, in Section 4.2), which enabled the use of larger time steps in both the explicit and implicit analyses.

The benefit of the implicit method in terms of calculation time is readily apparent in Table 4.3 and follows directly from the enabled use of large time steps. However, it is worth noting that the relative difference in calculation time between the implicit and the

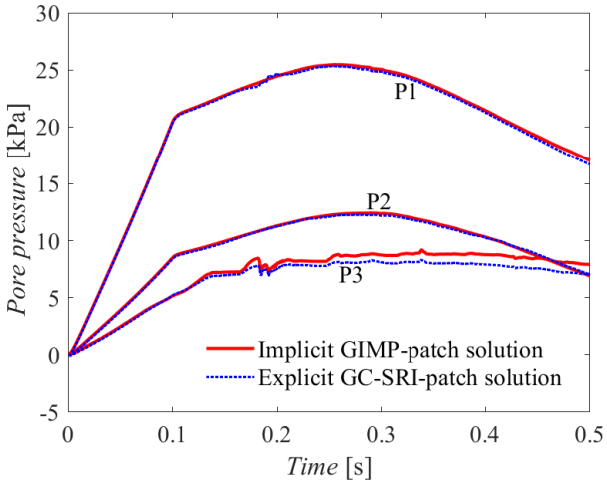

Figure 4.13: Time evolution of the excess pore pressure at three different locations (points P1, P2, P3 in Fig. 4.10) obtained for a 2D slumping block using the implicit GIMP-patch method and the explicit GC-SRI-patch method

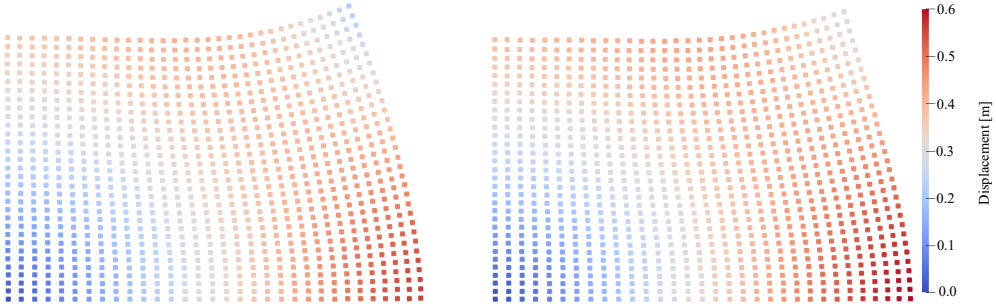

(a) Implicit GIMP-patch method

(b) Explicit GC-SRI-patch method

Figure 4.14: Solid displacement field obtained at $t = 0.5$ s using the implicit GIMP-patch method and the explicit GC-SRI-patch method

explicit codes tends to gradually decrease as the problem domain is discretised with a larger number of MPs and grid cells (e.g., as in the 2D slumping block example). This is due to the implicit solver (in this case, the PARDISO solver), which solves the full system of equations. The PARDISO solver is based on a direct solver (Schenk & Gärtner, 2011), which has numerical factorisation as the major step in the solution, which for 2D problems has an order of complexity $O\left(n^{3/2}\right)$ (where n is the size of the vector of unknowns). In the explicit method, the increase in time is simply proportional to the number of unknowns. Therefore, as the size of the problem increases, the implicit method becomes less advantageous. This aspect should be borne in mind when tackling relatively large problems, which may require, e.g., parallel computing techniques for faster solution

when using the implicit GIMP-patch method.

Table 4.3: Computational performance of the considered implicit and explicit MPMs in relation to the verification examples 1, 4, and 5

Example	Implicit		Explicit	
	Δt	CT	Δt	CT
1	1.0×10^{-3} s	9 s	1.0×10^{-5} s	386 s
4	5.0×10^{-3} s	17 min	5.0×10^{-5} s	279 min
5	1.0×10^{-3} s	5 min	1.0×10^{-5} s	54 min

4.5. CONCLUSIONS

THIS chapter has presented a fully implicit, stabilised MPM for dynamic coupled problems in porous media. The proposed method is based on a three-field *u*–*p*–*U* formulation of the governing conservation laws and equal/low-order interpolation of the three primary variables, namely solid displacement, pore pressure, and water displacement. Combining enhanced GIMP interpolation functions with a Moving Least Square Approximation (MLSA)-based patch recovery scheme for pore pressures has been shown to produce accurate, stable and oscillation-free results over different inertial and deformation regimes. In particular, five 1D/2D poroelastic examples have been used to demonstrate the good performance of the implicit MPM in comparison with analytical solutions (when available) and MPM solutions obtained through the explicit GC-SRI-patch MPM method proposed in Chapter 3 (Zheng *et al.*, 2021a).

The computational benefit of the implicit method is substantial and stems directly from the possibility to use larger time steps. However, it has also been pointed out that its relative advantage with respect to the explicit algorithm tends to reduce as problems of increasing size are tackled. Future work will be devoted to boosting the computational performance (e.g., via parallel computing), as well as to include more realistic soil constitutive models for the solution of a wider class of large-deformation geotechnical problems.

REFERENCES

Abe, K., Soga, K. & Bandara, S. (2013). Material point method for coupled hydromechanical problems. *Journal of Geotechnical and Geoenvironmental Engineering* **140**, No. 3, 04013033.

Arduino, P. & Macari, E. J. (2001). Implementation of porous media formulation for geomaterials. *Journal of Engineering Mechanics* **127**, No. 2, 157–166.

Bandara, S. & Soga, K. (2015). Coupling of soil deformation and pore fluid flow using material point method. *Computers and Geotechnics* **63**, 199–214.

Bardenhagen, S. G. & Kober, E. M. (2004). The generalized interpolation material point method. *Computer Modeling in Engineering and Sciences* **5**, No. 6, 477–496.

Bathe, K. J. (2001). The inf–sup condition and its evaluation for mixed finite element methods. *Computers and Structures* **79**, No. 2, 243–252.

Belytschko, T., Liu, W. K., Moran, B. & Elkhodary, K. (2013). *Nonlinear finite elements for continua and structures*. John Wiley & Sons.

Blanc, T. & Pastor, M. (2013). A stabilized smoothed particle hydrodynamics, Taylor–Galerkin algorithm for soil dynamics problems. *International Journal for Numerical and Analytical Methods in Geomechanics* **37**, No. 1, 1–30.

Brezzi, F. & Bathe, K.-J. (1990). A discourse on the stability conditions for mixed finite element formulations. *Computer Methods in Applied Mechanics and Engineering* **82**, No. 1-3, 27–57.

Charlton, T., Coombs, W. & Augarde, C. (2017). iGIMP: An implicit generalised interpolation material point method for large deformations. *Computers & Structures* **190**, 108–125.

Chen, Z. P., Zhang, X., Sze, K. Y., Kan, L. & Qiu, X. M. (2018). v-p material point method for weakly compressible problems. *Computers and Fluids* **176**, 170–181.

Chmelnizkij, A., Ceccato, F., Grabe, J. & Simonini, P. (2019). 1d wave propagation in saturated soils: verification of two-phase mpm. In *2nd International conference on the material point method for modelling soil-water-structure interaction. Cambridge, UK*.

Coombs, W. M., Augarde, C. E., Brennan, A. J., Brown, M. J., Charlton, T. J., Knappett, J. A., Motlagh, Y. G. & Wang, L. (2020). On lagrangian mechanics and the implicit material point method for large deformation elasto-plasticity. *Computer Methods in Applied Mechanics and Engineering* **358**, 112622.

Cryer, C. (1963). A comparison of the three-dimensional consolidation theories of Biot and Terzaghi. *The Quarterly Journal of Mechanics and Applied Mathematics* **16**, No. 4, 401–412.

Cummins, S. & Brackbill, J. (2002). An implicit particle-in-cell method for granular materials. *Journal of Computational Physics* **180**, No. 2, 506–548.

Gajo, A., Saetta, A. & Vitaliani, R. (1994). Evaluation of three-and two-field finite element methods for the dynamic response of saturated soil. *International Journal for Numerical Methods in Engineering* **37**, No. 7, 1231–1247.

Gibson, R., England, G. & Hussey, M. (1967). The theory of one-dimensional consolidation of saturated clays: 1. Finite non-linear consildation of thin homogeneous layers. *Géotechnique* **17**, No. 3, 261–273.

González Acosta, L. J., Vardon, P. J. & Hicks, M. A. (2017). Composite material point method (CMPM) to improve stress recovery for quasi-static problems. *Procedia Engineering* **175**, 324–331.

González Acosta, L. J., Vardon, P. J. & Hicks, M. A. (2021). Development of an implicit contact technique for the material point method. *Computers and Geotechnics* **130**, 103859.

González Acosta, L. J., Vardon, P. J., Remmerswaal, G. & Hicks, M. A. (2020). An investigation of stress inaccuracies and proposed solution in the material point method. *Computational Mechanics* **65**, No. 2, 555–581.

Guilkey, J. E. & Weiss, J. A. (2003). Implicit time integration for the material point method: Quantitative and algorithmic comparisons with the finite element method. *International Journal for Numerical Methods in Engineering* **57**, No. 9, 1323–1338.

Holzapfel, A. G. (2000). *Nonlinear solid mechanics ii*. Wiley: New York.

Hughes, T. J. (1987). *The finite element method: linear static and dynamic finite element analysis*. Prentice-Hall.

Jassim, I., Stolle, D. & Vermeer, P. (2013). Two-phase dynamic analysis by material point method. *International Journal for Numerical and Analytical Methods in Geomechanics* **37**, No. 15, 2502–2522.

Jeremić, B., Cheng, Z., Taiebat, M. & Dafalias, Y. (2008). Numerical simulation of fully saturated porous materials. *International Journal for Numerical and Analytical Methods in Geomechanics* **32**, No. 13, 1635–1660.

Kularathna, S., Liang, W., Zhao, T., Chandra, B., Zhao, J. & Soga, K. (2021). A semi-implicit material point method based on fractional-step method for saturated soil. *International Journal for Numerical and Analytical Methods in Geomechanics* **45**, No. 10, 1405–1436.

Ma, X., Giguere, P. T., Jayaraman, B. & Zhang, D. Z. (2010). Distribution coefficient algorithm for small mass nodes in material point method. *Journal of Computational Physics* **229**, No. 20, 7819–7833.

Mandel, J. (1953). Consolidation des sols (étude mathématique). *Geótechnique* **3**, No. 7, 287–299.

Navas, P., López-Querol, S., Yu, R. C. & Li, B. (2016). B-bar based algorithm applied to meshfree numerical schemes to solve unconfined seepage problems through porous media. *International Journal for Numerical and Analytical Methods in Geomechanics* **40**, No. 6, 962–984.

Navas, P., Sanavia, L., López-Querol, S. & Rena, C. Y. (2018). Explicit meshfree solution for large deformation dynamic problems in saturated porous media. *Acta Geotechnica* **13**, No. 2, 227–242.

Newmark, N. M. (1959). A method of computation for structural dynamics. *Journal of the Engineering Mechanics Division* **85**, No. 3, 67–94.

Pisanò, F. & Pastor, M. (2011). 1D wave propagation in saturated viscous geomaterials: Improvement and validation of a fractional step Taylor–Galerkin finite element algorithm. *Computer Methods in Applied Mechanics and Engineering* **200**, No. 47-48, 3341–3357.

Schenk, O. & Gärtner, K. (2002). Two-level dynamic scheduling in pardiso: Improved scalability on shared memory multiprocessing systems. *Parallel Computing* **28**, No. 2, 187–197.

Schenk, O. & Gärtner, K. (2011). Pardiso. In *Encyclopedia of Parallel Computing* (Padua, D., ed.), Boston, MA: Springer US, pp. 1458–1464.

Soga, K., Alonso, E., Yerro, A., Kumar, K. & Bandara, S. (2015). Trends in large-deformation analysis of landslide mass movements with particular emphasis on the material point method. *Géotechnique* **66**, No. 3, 248–273.

Staubach, P., Machaček, J., Moscoso, M. & Wichtmann, T. (2020). Impact of the installation on the long-term cyclic behaviour of piles in sand: A numerical study. *Soil Dynamics and Earthquake Engineering* **138**, 106223.

Sulsky, D. & Kaul, A. (2004). Implicit dynamics in the material-point method. *Computer Methods in Applied Mechanics and Engineering* **193**, No. 12-14, 1137–1170.

Taylor, C. & Hood, P. (1973). A numerical solution of the navier-stokes equations using the finite element technique. *Computers & Fluids* **1**, No. 1, 73–100.

Terzaghi, K. (1943). *Theoretical soil mechanics*. Wiley: New York.

Tran, Q.-A. & Sołowski, W. (2019). Temporal and null-space filter for the material point method. *International Journal for Numerical Methods in Engineering* **120**, No. 3, 328–360.

Van Esch, J., Stolle, D. & Jassim, I. (2011). Finite element method for coupled dynamic flow-deformation simulation. In *2nd International Symposium on Computational Geomechanics (COMGEO II), Cavtat-Dubrovnik, Croatia*.

Verruijt, A. (2009). *An introduction to soil dynamics*. Springer Science & Business Media.

Wang, B., Vardon, P. J. & Hicks, M. A. (2018). Rainfall-induced slope collapse with coupled material point method. *Engineering Geology* **239**, 1–12.

Wang, B., Vardon, P. J., Hicks, M. A. & Chen, Z. (2016). Development of an implicit material point method for geotechnical applications. *Computers and Geotechnics* **71**, 159–167.

Xie, K. & Leo, C. J. (2004). Analytical solutions of one-dimensional large strain consolidation of saturated and homogeneous clays. *Computers and Geotechnics* **31**, No. 4, 301–314.

Zhao, Y. & Choo, J. (2020). Stabilized material point methods for coupled large deformation and fluid flow in porous materials. *Computer Methods in Applied Mechanics and Engineering* **362**, 112742.

Zheng, X. C., Pisanò, F., Vardon, P. J. & Hicks, M. A. (2021a). An explicit stabilised material point method for coupled hydromechanical problems in two-phase porous media. *Computers and Geotechnics* **135**, 104112.

Zheng, X. C., Pisanò, F., Vardon, P. J. & Hicks, M. A. (2021b). Formulation and verification of a fully implicit three-field material point method for dynamic coupled problems , Under review.

Zienkiewicz, O., Chang, C. & Bettess, P. (1980). Drained, undrained, consolidating and dynamic behaviour assumptions in soils. *Géotechnique* **30**, No. 4, 385–395.

Zienkiewicz, O. C., Chan, A., Pastor, M., Schrefler, B. & Shiomi, T. (1999). *Computational geomechanics with special reference to earthquake engineering*. John Wiley & Sons.

Zienkiewicz, O. C. & Shiomi, T. (1984). Dynamic behaviour of saturated porous media; the generalized Biot formulation and its numerical solution. *International Journal for Numerical and Analytical Methods in Geomechanics* **8**, No. 1, 71–96.

Zienkiewicz, O. C., Taylor, R. L. & Zhu, J. Z. (2005). *The finite element method: its basis and fundamentals*. Elsevier.

Zienkiewicz, O. C. & Zhu, J. (1992). The superconvergent patch recovery (SPR) and adaptive finite element refinement. *Computer Methods in Applied Mechanics and Engineering* **101**, No. 1-3, 207–224.

5

IMPLICIT MPM SIMULATION OF LARGE-DEFORMATION PROBLEMS IN COUPLED ELASTOPLASTIC GEOMATERIALS

The Material Point Method (MPM) has been gaining increasing popularity as an appropriate approach to the solution of coupled hydro-mechanical problems involving large deformations. This chapter extends the implicit GIMP-patch method proposed in Chapter 4 (Zheng et al., 2021b) to tackle large-deformation problems in (nearly) isochoric elastoplastic geomaterials, particularly by remedying the numerical inaccuracies caused by volumetric locking, such as spurious stress oscillations and, overall, an excessively stiff response of the system at hand. To overcome these difficulties in two-phase coupled analyses, the $\overline{\mathrm{B}}$ approach of Hughes (1980) is incorporated into the implicit GIMP-patch method developed in Chapter 4, which has already been successfully verified for coupled poroelastic problems. Details regarding the formulation and implementation of the proposed method are provided, while several benchmark problems are numerically analysed to evaluate its performance in the presence of elastoplastic behaviour. The numerical results confirm the suitability of the implicit $\overline{\mathrm{B}}$ GIMP-patch method for the solution of geo-problems spanning weak to strong hydro-mechanical coupling and small to large deformations.

Parts of this chapter appear in Zheng *et al.* (2022).

5.1. INTRODUCTION

SIMILARLY to the case of coupled Finite Element Methods (FEMs), MPMs also perform poorly in the presence of incompressibility constraints when built on low-order spatial interpolation. With regard to fluid-saturated geomaterials, incompressible behaviour may be associated with hindered pore water drainage and/or a (nearly) isochoric response of the solid skeleton (Bandara & Soga, 2015): while the former may induce well-known instabilities in the simulated pore pressure field, the latter may give rise to an excessively stiff response of the system (volumetric locking) – it is worth recalling that constitutive models for geomaterials produce only limited volumetric strain increments when substantial plasticity is mobilised. To suppress pore pressure instabilities in low-order coupled MPMs, several stabilisation approaches have been adopted, including fractional time stepping (Jassim *et al.*, 2013; Kularathna *et al.*, 2021), polynomial pressure projection (Zhao & Choo, 2020), and reduced integration (Abe *et al.*, 2013; Bandara & Soga, 2015; Wang *et al.*, 2018; Zheng *et al.*, 2021a,b). On the other hand, locking-related inaccuracies can be mitigated in two-phase coupled problems by means of techniques initially developed for one-phase media. In the context of one-phase MPM modelling, solutions based, e.g., on mixed variational principles (Mast *et al.*, 2012; Iaconeta *et al.*, 2019), fractional time stepping (Kularathna & Soga, 2017; Zhang *et al.*, 2017), and $\overline{\mathrm{F}}$ and $\overline{\mathrm{B}}$ methods (Coombs *et al.*, 2018; Bisht *et al.*, 2021), have already proven successful against locking in one-phase large-deformation problems. In very few instances, such locking remedies have also been implemented in coupled (standard) MPMs (Jassim *et al.*, 2013; Bandara & Soga, 2015), but exclusively in combination with explicit time integration. Most recently, Kularathna *et al.* (2021) proposed a stable time-stepping scheme for the MPM modelling of fluid-saturated porous media within the framework of the Generalised Interpolation Material Point (GIMP) method (which is a variant of standard MPM).

This chapter demonstrates the benefits of combining the well-known anti-locking $\overline{\mathrm{B}}$ approach (originally proposed by Hughes (1980) for incompressible FEM modelling) with the fully implicit, three-field GIMP-patch method developed in Chapter 4 for coupled large-deformation problems (Zheng *et al.*, 2021b). The resulting method, named 'implicit $\overline{\mathrm{B}}$ GIMP-patch' method, is shown in this chapter to score two important goals: (i) it can substantially alleviate (undrained) pore pressure instabilities, owing to a beneficial combination of selective reduced integration and patch recovery based on a Moving Least Square Approximation (MLSA) (see Chapter 3); (ii) it exploits the $\overline{\mathrm{B}}$ approach to remedy locking-related inaccuracies in the presence of a (nearly) isochoric plastic behaviour of the solid skeleton.

To the author's knowledge, the proposed combination of pressure stabilisation and anti-locking techniques is here explored for the first time in the framework of a fully implicit coupled MPM (within the framework of GIMP). The contents of the chapter are organised as follows: after briefly summarising in Section 5.2 the fundamentals of the earlier implicit GIMP-patch method (based on a u–p–U formulation of the reference hydro-mechanical problem), technical details regarding the incorporation of the $\overline{\mathrm{B}}$ method are covered in Section 5.3; in Section 5.4 the performance of the proposed method is discussed with reference to a number of numerical verification examples.

5.2. FORMULATION OF THE IMPLICIT GIMP-PATCH METHOD

In this section, the main equations governing the dynamics of saturated soil-like materials based on the three-field u–p–U formulation are first reiterated; then, the discretisation and stabilisation processes associated with the implicit GIMP-patch method are also summarised. Note that only those equations essential to a full understanding of the development in this chapter are presented. More details and further links to previous literature have already been covered in Chapter 4.

5.2.1. GOVERNING EQUATIONS

For fully-saturated porous media, the momentum balance equations associated with the whole two-phase mixture and the pore water phase read respectively as (Zienkiewicz & Shiomi, 1984; Zienkiewicz *et al.*, 1999)

$$\mathbf{S}^{\mathrm{T}}\boldsymbol{\sigma} - \rho\ddot{\boldsymbol{u}} - \rho_w\ddot{\boldsymbol{u}}_r + \rho\boldsymbol{b} = \mathbf{0} \tag{5.1}$$

$$\nabla p - \boldsymbol{R} - \rho_w\ddot{\boldsymbol{u}} - \rho_w\frac{\ddot{\boldsymbol{u}}_r}{n} + \rho_w\boldsymbol{b} = \mathbf{0} \tag{5.2}$$

where $\mathbf{S}$ is a differential divergence operator, $\boldsymbol{u}$ is the absolute displacement of the soil skeleton, $\boldsymbol{u}_r$ is the displacement of the water phase relative to the solid phase and defined by $\boldsymbol{u}_r = n(\boldsymbol{U} - \boldsymbol{u})$ (where $\boldsymbol{U}$ is the absolute displacement of the water phase), $\boldsymbol{b}$ is an external body force, and $\boldsymbol{R}$ is the drag force exchanged by the soil skeleton and the pore water due to their relative motion; dots are used to indicate time differentiation.

The pore water flow must satisfy the following mass conservation equation:

$$\nabla\cdot\dot{\boldsymbol{u}}_r + \nabla\cdot\dot{\boldsymbol{u}} + \frac{\dot{p}}{Q} = \mathbf{0} \tag{5.3}$$

where the stiffness parameters Q, defined as $1/Q = n/K_w + (1-n)/K_s - K_w$, and K_s are the bulk moduli of the water phase and soil particles, respectively.

In addition to the above conservation laws, hydraulic and mechanical constitutive relationships are also required, namely for the drag force $\boldsymbol{R}$ $(= \frac{n\rho_w g}{k}\left(\dot{\boldsymbol{U}} - \dot{\boldsymbol{u}}\right)$, with k and g standing for soil permeability and gravitational acceleration, respectively) and the soil skeleton behaviour. The latter is normally expressed by relating the rates of effective stress ($\dot{\boldsymbol{\sigma}}'$) and strain ($\dot{\boldsymbol{\varepsilon}}$):

$$\dot{\boldsymbol{\sigma}}' = \mathbf{D}^{ep}\dot{\boldsymbol{\varepsilon}} \tag{5.4}$$

where the elasto-plastic stiffness matrix of the solid skeleton ($\mathbf{D}^{ep}$) is used in combination with a linearised definition of the strain rate (González Acosta *et al.*, 2021; Tran & Sołowski, 2019; Zheng *et al.*, 2021a). It should be noted that this work focuses on the implementation of the $\overline{B}$ approach in a coupled implicit MPM, and on its verification for coupled elastoplastic problems – particularly with respect to the notorious numerical oscillation issues that are often associated with MPM modelling (González Acosta *et al.*, 2017, 2020; Zheng *et al.*, 2021a). Fully general modelling of large deformations can be achieved by introducing well-established finite strain measures (Holzapfel, 2000) – such an extension is not expected to heavily impact the hydromechanical performance of the proposed method and will be pursued in future work.

5.2.2. SPACE AND TIME DISCRETISATION

In the context of a three-field u–p–U formulation, the primary variables $\boldsymbol{u}$ (solid displacement), p (pore pressure), and $\boldsymbol{U}$ (fluid displacement) are first approximated using their nodal values ($\bar{\boldsymbol{u}}$, $\bar{\boldsymbol{p}}$, and $\bar{\boldsymbol{U}}$) in the background mesh:

$$\boldsymbol{u} = \mathbf{N}_u \bar{\boldsymbol{u}}, \qquad p = \boldsymbol{N}_p \bar{\boldsymbol{p}}, \qquad \boldsymbol{U} = \mathbf{N}_U \bar{\boldsymbol{U}} \tag{5.5}$$

where $\mathbf{N}_u$, $\boldsymbol{N}_p$, and $\mathbf{N}_U$ are matrices containing shape functions of the same low order (bilinear in 2D problems). Substituting the above approximations (Equation (5.5)) into the weak form of the governing equations ((5.1), (5.2), and (5.3)) leads to the following discrete system of ordinary differential equations:

$$\begin{bmatrix} \mathbf{M}_u & \mathbf{0} & \mathbf{0} \\ \mathbf{0} & \mathbf{0} & \mathbf{0} \\ \mathbf{0} & \mathbf{0} & \mathbf{M}_U \end{bmatrix} \begin{bmatrix} \ddot{\bar{\boldsymbol{u}}} \\ \ddot{\bar{\boldsymbol{p}}} \\ \ddot{\bar{\boldsymbol{U}}} \end{bmatrix} + \begin{bmatrix} \mathbf{C}_1 & \mathbf{0} & -\mathbf{C}_2 \\ \mathbf{0} & \mathbf{0} & \mathbf{0} \\ -\mathbf{C}_2^{\mathrm{T}} & \mathbf{0} & \mathbf{C}_3 \end{bmatrix} \begin{bmatrix} \dot{\bar{\boldsymbol{u}}} \\ \dot{\bar{\boldsymbol{p}}} \\ \dot{\bar{\boldsymbol{U}}} \end{bmatrix} + \begin{bmatrix} \mathbf{K}_u & -\mathbf{G}_1 & \mathbf{0} \\ -\mathbf{G}_1^{\mathrm{T}} & \mathbf{P} & -\mathbf{G}_2^{\mathrm{T}} \\ \mathbf{0} & -\mathbf{G}_2 & \mathbf{0} \end{bmatrix} \begin{bmatrix} \bar{\boldsymbol{u}} \\ \bar{\boldsymbol{p}} \\ \bar{\boldsymbol{U}} \end{bmatrix} = \begin{bmatrix} \bar{\boldsymbol{f}}_s \\ \mathbf{0} \\ \bar{\boldsymbol{f}}_w \end{bmatrix} \tag{5.6}$$

where: $\mathbf{M}_u$ and $\mathbf{M}_U$ are mass matrices for the soil and water phases; $\mathbf{C}_1$, $\mathbf{C}_2$, and $\mathbf{C}_3$ are damping matrices physically associated with grain–fluid drag (no Rayleigh damping included); $\mathbf{K}_u$ is the stiffness matrix of the solid skeleton; $\mathbf{P}$ is a compressibility matrix determined by the bulk stiffness of the solid grains and pore water; $\mathbf{G}_1$ and $\mathbf{G}_2$ are two matrices describing the hydro-mechanical coupling between the skeleton deformation and pore water flow; $\bar{\boldsymbol{f}}_s$ and $\bar{\boldsymbol{f}}_w$ are nodal force vectors associated with the solid and water phases. The detailed expressions of these matrices emerge from the spatial discretisation process, and are provided by Zienkiewicz & Shiomi (1984) and Zheng *et al.* (2021b) with reference to FEM and MPM modelling, respectively.

Within the framework of MPM, the matrices in Equation (5.6) can be obtained through the assembly of matrix contributions evaluated at the grid cell nodes after mapping from the MPs. If the same bilinear shape functions (in 2D problems) as in low-order FEM are used, then standard MPM results may suffer from spurious oscillations associated with discontinuous shape function gradients, particularly in the event of MP cell-crossing (Bardenhagen & Kober, 2004). To mitigate such oscillations, Bardenhagen & Kober (2004) proposed the GIMP approach, which is based on shape functions constructed by integrating linear shape functions $N_i(x)$ over the MP support domain Ω_{mp} – the subscripts i and mp indicate the i^{th} node and m^{th} MP.

Using GIMP shape functions and their gradients, the matrices in the discrete system (5.6) can be obtained (more details can be found in Chapter 4). The whole equation set, after space discretisation, can be represented in the following compact form:

$$\mathbf{M}\boldsymbol{a} + \mathbf{C}\boldsymbol{v} + \mathbf{K}\boldsymbol{d} = \bar{\boldsymbol{f}} \tag{5.7}$$

where: $\mathbf{M}$, $\mathbf{C}$, and $\mathbf{K}$ are generalised mass, damping, and stiffness matrices, respectively; $\bar{\boldsymbol{f}}$ is a time-varying external load term; $\boldsymbol{a} = \left[\ddot{\bar{\boldsymbol{u}}}, \ddot{\bar{\boldsymbol{p}}}, \ddot{\bar{\boldsymbol{U}}}\right]^{\mathrm{T}}$, $\mathbf{v} = [\dot{\bar{\boldsymbol{u}}}, \dot{\bar{\boldsymbol{p}}}, \dot{\bar{\boldsymbol{U}}}]^{\mathrm{T}}$, and $\boldsymbol{d} = [\bar{\boldsymbol{u}}, \bar{\boldsymbol{p}}, \bar{\boldsymbol{U}}]^{\mathrm{T}}$ are generalised nodal displacement, velocity, and acceleration vectors, respectively.

The ordinary differential system in Equation (5.7) can be implicitly integrated in time using the well-established Newmark algorithm (Newmark, 1959). Using two time integration parameters γ and β, the corresponding recurrence relations for stepping from

n to $n+1$ are (Hughes, 1987):

$$\boldsymbol{a}_{n+1} = \boldsymbol{a}_n + \Delta\boldsymbol{a} \tag{5.8a}$$

$$\boldsymbol{v}_{n+1} = \boldsymbol{v}_n + \Delta t\left[\left(1-\gamma\right)\boldsymbol{a}_n + \gamma\boldsymbol{a}_{n+1}\right] \tag{5.8b}$$

$$\boldsymbol{d}_{n+1} = \boldsymbol{d}_n + \boldsymbol{v}_n\Delta t + \frac{\Delta t^2}{2}\left[\left(1-2\beta\right)\boldsymbol{a}_n + 2\beta\boldsymbol{a}_{n+1}\right] \tag{5.8c}$$

in which $\Delta t = t_{n+1} - t_n$ is the (constant) time step size. After substituting the above recurrence relations into Equation (5.7), the following algebraic system of fully discretised equations results:

$$\overline{\mathbf{K}}\Delta\boldsymbol{d}_{n+1} = \bar{\boldsymbol{f}}_{n+1} - \boldsymbol{f}_n^{int} + \mathbf{M}_n\left[\frac{f_1}{\Delta t}\boldsymbol{v}_n + \left(\frac{f_1}{2}-1\right)\boldsymbol{a}_n\right] + \mathbf{C}_n\left[\left(f_2-1\right)\boldsymbol{v}_n + \left(\frac{f_2}{2}-1\right)\boldsymbol{a}_n\Delta t\right] \tag{5.9}$$

where $\overline{\mathbf{K}} = \dfrac{f_1}{\Delta t^2}\mathbf{M}_n + \dfrac{f_2}{\Delta t}\mathbf{C}_n + \mathbf{K}_n$ is an algorithmic dynamic stiffness matrix based on the evaluations at the n^{th} step of the generalised mass, damping, and stiffness matrices (respectively, $\mathbf{M}_n$, $\mathbf{C}_n$, and $\mathbf{K}_n$), $f_1 = 1/\beta$ and $f_2 = \gamma/\beta$, and $\boldsymbol{f}_n^{int} = \left[\boldsymbol{f}_{u,n}^{int}, \boldsymbol{f}_{p,n}^{int}, \boldsymbol{f}_{U,n}^{int}\right]^{\mathrm{T}}$ is the internal nodal force vector:

$$\boldsymbol{f}_{u,i}^{int} = \sum_{mp=1}^{N_{mp}} \mathbf{B}_{u,i}^{\mathrm{T}}\left(\boldsymbol{x}_{mp,n}\right)\left[\boldsymbol{\sigma}'_{mp,n} - \left(1-n\right)\boldsymbol{m}p_{mp,n}\right]V_{mp,n} \tag{5.10a}$$

$$f_{p,i}^{int} = \sum_{mp=1}^{N_{mp}}\left[-\left(1-n\right)S_{p,i}(\boldsymbol{x}_{mp,n})\varepsilon_{vol,mp}^{u} - S_{p,i}(\boldsymbol{x}_{mp,n})\frac{p_{mp,n}}{Q} - nS_{p,i}(\boldsymbol{x}_{mp,n})\varepsilon_{v,mp}^{U}\right]V_{mp,n} \tag{5.10b}$$

$$\boldsymbol{f}_{U,i}^{int} = -\sum_{mp=1}^{N_{mp}}\mathbf{B}_{U,i}^{\mathrm{T}}\left(\boldsymbol{x}_{mp,n}\right)n\boldsymbol{m}p_{mp,n}V_{mp,n} \tag{5.10c}$$

and N_{mp} is the total number of MPs; $\varepsilon_{vol,mp}^{u}$ and $\varepsilon_{vol,mp}^{U}$ are the volumetric strain of the soil and water phases at the mp^{th} MP; $\boldsymbol{x}_{mp,n}$ and $V_{mp,n}$ are the coordinate and volume of mp^{th} MP at step n, while $\boldsymbol{\sigma}'_{mp,n}$ and $p_{mp,n}$ indicate the corresponding effective stress and pore pressure values; and the subscripts/superscripts u, p and U, respectively, indicate variables associated with the primary variables in the u–p–U formulation. In the remainder of this study, a single pair of integration parameters, $\beta = 0.25$ and $\gamma = 0.5$, is exclusively considered.

Since elasto-plastic large-deformation problems are intrinsically non-linear, the discretised system (5.9) must be solved iteratively. To this end, each time step is solved through the Modified Newton–Raphson iteration scheme (Zienkiewicz *et al.*, 2005). When the state of equilibrium is reached, all relevant variables are updated at the MPs using the

computed nodal values as follows:

$$\boldsymbol{a}_{mp,n+1} = \sum_{i=1}^{N_{node}} \mathbf{S}_{u,i}(\boldsymbol{x}_{mp,n})\boldsymbol{a}_{i,n+1} \tag{5.11a}$$

$$\boldsymbol{v}_{mp,n+1} = \sum_{i=1}^{N_{node}} \mathbf{S}_{u,i}(\boldsymbol{x}_{mp,n})\boldsymbol{v}_{i,n+1} \tag{5.11b}$$

$$\boldsymbol{\sigma}'_{mp,n+1} = \boldsymbol{\sigma}'_{mp,n} + \mathbf{D}^{ep} \sum_{n=1}^{N_{node}} \mathbf{B}_{u,i}(\boldsymbol{x}_{mp,n})\bar{\boldsymbol{u}}_{i,n+1} \tag{5.11c}$$

$$p_{mp,n+1} = p_{mp,n} + \sum_{n=1}^{N_{node}} S_{p,i}(\boldsymbol{x}_{mp,n})\bar{p}_{i,n+1} \tag{5.11d}$$

$$\boldsymbol{x}_{mp,n+1} = \boldsymbol{x}_{mp,n} + \sum_{n=1}^{N_{node}} \mathbf{S}_{u,i}(\boldsymbol{x}_{mp,n})\bar{\boldsymbol{u}}_{i,n+1} \tag{5.11e}$$

where N_{node} is the total number of nodes, and $\bar{\boldsymbol{u}}_{i,n+1}$ and $\bar{p}_{i,n+1}$ are the nodal incremental displacements and pore pressure at the $(n+1)^{th}$ step.

To alleviate pore pressure instabilities in coupled analyses, a patch recovery algorithm based on a Moving Least Square Approximation (MLSA) has been introduced in the implicit GIMP method in Chapter 4 (Zheng *et al.*, 2021b), following the earlier explicit implementation described in Chapter 3 (Zheng *et al.*, 2021a). The implicit GIMP-patch method was tested for poroelastic coupled problems in Chapter 4 and shown to produce stable and oscillation-free solutions.

5.3. IMPLEMENTATION OF THE $\overline{\text{B}}$ LOCKING ANTIDOTE INTO THE IMPLICIT GIMP-PATCH METHOD

In a similar manner to low-order FEMs, the accuracy of the coupled implicit GIMP-patch method may also be negatively impacted by volumetric locking effects, which are likely to manifest themselves when the soil skeleton deforms at (nearly) constant volume (e.g., during plastic flow) and a full strain integration is adopted in the stress analysis (Coombs *et al.*, 2018). In this study, the original version of the $\overline{\text{B}}$ method for low-order FEMs (Hughes, 1980) is implemented in the implicit GIMP-patch method to remedy locking-related inaccuracies in elasto-plastic large-deformation problems. The essence of the $\overline{\text{B}}$ approach is to evaluate the excessively stiff volumetric component of the compatibility matrix ($\mathbf{B}_i$) via reduced quadrature, while full quadrature is still employed for the complementary deviatoric part (Hughes, 1980). Accordingly, the compatibility matrix $\mathbf{B}_i$ is first split at a given node i into deviatoric ($\mathbf{B}_i^{dev}$) and volumetric ($\mathbf{B}_i^{vol}$) components, so that $\mathbf{B}_i = \mathbf{B}_i^{dev} + \mathbf{B}_i^{vol}$. In the case of plane strain conditions, the $\mathbf{B}_i$ and $\mathbf{B}_i^{vol}$ matrices assume the following forms:

$$\mathbf{B}_i = \begin{bmatrix} \frac{\partial N_i}{\partial x} & 0 \\ 0 & \frac{\partial N_i}{\partial y} \\ \frac{\partial N_i}{\partial y} & \frac{\partial N_i}{\partial x} \\ 0 & 0 \end{bmatrix}, \qquad \mathbf{B}_i^{vol} = \frac{1}{3} \begin{bmatrix} \frac{\partial N_i}{\partial x} & \frac{\partial N_i}{\partial y} \\ \frac{\partial N_i}{\partial x} & \frac{\partial N_i}{\partial y} \\ 0 & 0 \\ \frac{\partial N_i}{\partial x} & \frac{\partial N_i}{\partial y} \end{bmatrix}, \qquad \mathbf{B}_i^{dev} = \mathbf{B}_i - \mathbf{B}_i^{vol} \tag{5.12}$$

where N_i is the shape function associated with the i^{th} node.

In the FEM $\overline{\text{B}}$ method, the original volumetric matrix $\mathbf{B}_i^{vol}$ is replaced by the following 'improved' version evaluated at the grid cell centres (gc):

$$\overline{\mathbf{B}}_i^{vol} = \frac{1}{3}\begin{bmatrix} \frac{\partial N_{i,gc}}{\partial x} & \frac{\partial N_{i,gc}}{\partial y} \\ \frac{\partial N_{i,gc}}{\partial x} & \frac{\partial N_{i,gc}}{\partial y} \\ 0 & 0 \\ \frac{\partial N_{i,gc}}{\partial x} & \frac{\partial N_{i,gc}}{\partial y} \end{bmatrix} \tag{5.13}$$

while the deviatoric matrix $\mathbf{B}_i^{dev}$ is directly calculated at the Gauss point (gp) locations. As a result, the following global compatibility matrix $\overline{\mathbf{B}}_i$ is obtained:

$$\overline{\mathbf{B}}_i = \mathbf{B}_i^{dev} + \overline{\mathbf{B}}_i^{vol} = \begin{bmatrix} \frac{2}{3}\frac{\partial N_{i,gp}}{\partial x} + \frac{1}{3}\frac{\partial N_{i,gc}}{\partial x} & -\frac{1}{3}\frac{\partial N_{i,gp}}{\partial y} + \frac{1}{3}\frac{\partial N_{i,gc}}{\partial y} \\ -\frac{1}{3}\frac{\partial N_{i,gp}}{\partial x} + \frac{1}{3}\frac{\partial N_{i,gc}}{\partial x} & \frac{2}{3}\frac{\partial N_{i,gp}}{\partial y} + \frac{1}{3}\frac{\partial N_{i,gc}}{\partial y} \\ \frac{\partial N_{i,gp}}{\partial y} & \frac{\partial N_{i,gp}}{\partial x} \\ -\frac{1}{3}\frac{\partial N_{i,gp}}{\partial x} + \frac{1}{3}\frac{\partial N_{i,gc}}{\partial x} & -\frac{1}{3}\frac{\partial N_{i,gp}}{\partial y} + \frac{1}{3}\frac{\partial N_{i,gc}}{\partial y} \end{bmatrix} \tag{5.14}$$

The same $\overline{\text{B}}$ approach has been previously incorporated into two-phase standard MPM (Bandara & Soga, 2015) and one-phase GIMP (Bisht *et al.*, 2021), in both cases within an explicit time stepping scheme. It should be noted that such an implementation can easily be performed for a standard MPM, since the centre of each grid cell can be directly determined. In contrast, the $\overline{\text{B}}$ extension of GIMP is less straightforward – a specific MP may in fact be influenced by multiple cells when its support domain lies across more than one grid cell, which frequently happens during the movement of MPs. Following the approach proposed by Coombs *et al.* (2018), only that portion of the MP support domain lying within the domain of a grid cell is considered to contribute to the volumetric behaviour of the cell itself.

In order to construct the GIMP shape function and its gradient, the shape function $N_{i,gc}$ and its gradient $\nabla N_{i,gc}$ take values at the centre of a grid cell, which remain constant ($N_{i,gc} = \frac{1}{2}$ and $\nabla N_{i,gc} = \pm\frac{1}{h}$, where h is the size of a quadrilateral cell in a regular background mesh) through the entire cell. The one-dimensional GIMP shape function $S_{i,gc}$ is then computed as

$$S_{i,gc} = \frac{1}{V_{mp}}\int_{\Omega_{mp}} \frac{1}{2}\mathrm{d}x \tag{5.15}$$

Figure 5.1 shows the GIMP shape functions and their gradients sampled at the centre of the grid cell. Using the GIMP shape function, the modified $\bar{\mathbf{B}}_i$ matrix can be written as

$$\bar{\mathbf{B}}_i = \begin{bmatrix} \frac{2}{3}\frac{\partial S_{i,mp}}{\partial x} + \frac{1}{3}\frac{\partial S_{i,gc}}{\partial x} & -\frac{1}{3}\frac{\partial S_{i,mp}}{\partial y} + \frac{1}{3}\frac{\partial S_{i,gc}}{\partial y} \\ -\frac{1}{3}\frac{\partial S_{i,mp}}{\partial x} + \frac{1}{3}\frac{\partial S_{i,gc}}{\partial x} & \frac{2}{3}\frac{\partial S_{i,mp}}{\partial y} + \frac{1}{3}\frac{\partial S_{i,gc}}{\partial y} \\ \frac{\partial S_{i,mp}}{\partial y} & \frac{\partial_{i,mp}}{\partial x} \\ -\frac{1}{3}\frac{\partial S_{i,mp}}{\partial x} + \frac{1}{3}\frac{\partial S_{i,gc}}{\partial x} & -\frac{1}{3}\frac{\partial S_{i,mp}}{\partial y} + \frac{1}{3}\frac{\partial S_{i,gc}}{\partial y} \end{bmatrix} \tag{5.16}$$

After determining the modified $\bar{\mathbf{B}}_i$ matrix, the nodal stiffness and internal force matrices in Equation (5.9) and the effective stress vector in Equation (5.11c) can be computed by simply replacing the original $\mathbf{B}$ matrix with the modified $\bar{\mathbf{B}}_i$ matrix. Aside from the inclusion of the $\bar{\mathbf{B}}$ matrix, all other steps regarding space and time discretisation are the same as in the implicit GIMP-patch method proposed in Chapter 4 (Zheng *et al.*, 2021b).

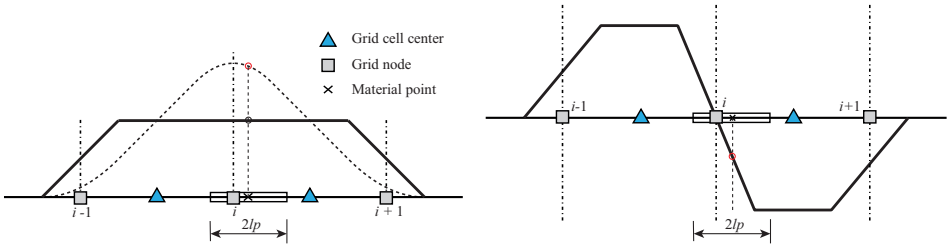

(a) GIMP shape function (b) GIMP shape function gradient

Figure 5.1: One-dimensional GIMP shape function and its gradient sampled at the centre of a grid cell

5

5.4. NUMERICAL VERIFICATION AND APPLICATION EXAMPLES

This section presents the numerical solutions obtained for several verification and application examples using the proposed implicit $\overline{\text{B}}$ GIMP-patch method. In all examples, the mechanical behaviour of the soil skeleton is reproduced by the Mohr-Coulomb model, based on a model implementation that does not include a tension cut-off.

5.4.1. BEARING CAPACITY OF A STRIP FOOTING

Numerical studies regarding the undrained bearing capacity of rough strip footings have often been performed by modelling the soil as a single-phase incompressible material (total stress analysis), both under small- and large-deformation conditions. Such a reference problem has recently been studied by Kiriyama & Higo (2020) and Bisht *et al.* (2021) via single-phase MPM simulations. As a preliminary verification of the implicit $\overline{\text{B}}$ GIMP-patch method, its single-phase, total stress performance is first verified with respect to the bearing capacity problem shown in Figure 5.2 (the symmetry with respect to the median plane has been exploited to reduce the computational cost). To comply with the total stress approach, the inherently two-phase numerical model has been set up to function as a one-phase system by (i) introducing a very large permeability, and (ii) reducing the Mohr-Coulomb frictional model to its cohesive/isochoric version (i.e., the Tresca model, in which the cohesion c coincides with the undrained strength s_u) – all material properties are listed in Table 5.1. As is usual in total stress limit load calculations, the initial stress state of the soil is not influential and, therefore, there is no need to account for its self-weight in the analysis (although a mass density is still assigned to the MPs for the calculation of the inertial terms associated with the u–p–U formulation).

Both the footing (breadth $B = 1$ m) and the soil layer have been discretised using 4-node quadrilateral grid cells, with each cell initially hosting 2×2 equally-spaced MPs. To enable meaningful comparison to static, one-phase solutions, the external load has

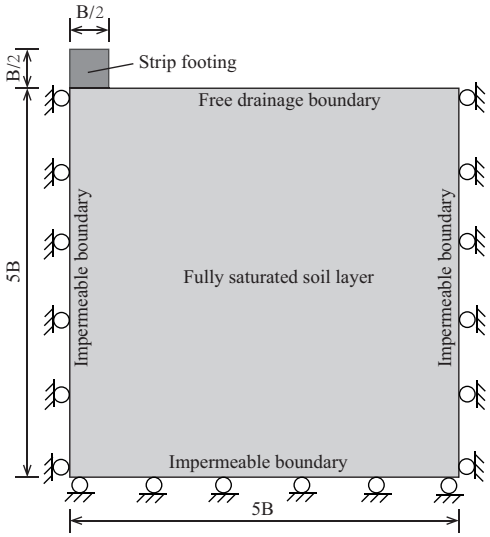

Figure 5.2: Reference bearing capacity problem for a strip footing: computational domain and boundary conditions

been applied at a sufficiently slow rate, so as to ensure negligible acceleration and excess pore pressure generation. Both numerical simulations have been performed with a time step size equal to $\Delta t = 5.0 \times 10^{-2}$ s, setting the same material parameters as those adopted by Bisht *et al.* (2021) for fair comparison. The selected time step size and loading rate have been verified to enable proper modelling of the inherently quasi-static process under consideration using the fully dynamic MPM formulation developed in this study.

SMALL-DEFORMATION ANALYSIS

The small-deformation (SD) analysis of the problem in Figure 5.2 has been performed in combination with a large ratio between the Young's modulus and the cohesion (undrained shear strength) of the soil, $E/c = 10000$, so as to achieve the bearing capacity limit – $q/c = 2 + \pi \approx 5.14$ – with only small settlement of the foundation. In this SD example the external vertical pressure q has been directly applied on the grid nodes below the footing, at a rate of 0.01 kPa/s. Figure 5.3 shows the SD relationship between the normalised load (q/c) and displacement (d/B) obtained for a grid cell size h equal to 0.25 m. In Figure 5.3, the implicit $\overline{\text{B}}$ GIMP-patch solution is compared to those solutions obtained via the implicit GIMP-patch method developed in Chapter 4 (Zheng *et al.*, 2021b) and the explicit $\overline{\text{B}}$ GIMP by Bisht *et al.* (2021). It is apparent that the implicit GIMP-patch solution severely overestimates the analytical capacity limit, while excellent agreement is observed between the result obtained by the method proposed in this study and the result obtained by Bisht *et al.* (2021). This outcome supports the anti-locking effectiveness of the implicit $\overline{\text{B}}$ GIMP-patch method, with a computational convenience that is expected to be superior to Bisht et al.'s method owing to the implicit time stepping scheme.

In more detail, Figure 5.4 displays the final distributions of the mean stress obtained through the implicit GIMP-patch method, as computed using both its original and $\overline{\text{B}}$

Table 5.1: Material properties adopted for the footing and the (two-phase) soil for the total stress analysis of the undrained bearing capacity problem in Figure 5.2

Property	Symbol	Unit	SD analysis	LD analysis
Young's modulus (footing)	E_f	[kPa]	10000	10000
Poisson's ratio (footing)	ν_f	[-]	0.3	0.3
Young's modulus	E	[kPa]	1000	100
Poisson's ratio	ν	[-]	0.49	0.49
Soil grain density	ρ_s	[kg/m^3]	2600	2600
Water density	ρ_w	[kg/m^3]	1000	1000
Friction angle	ϕ	[°]	0	0
Dilation angle	ψ	[°]	0	0
Cohesion	c	[kPa]	0.1	1.0
Initial porosity	n	[-]	0.4	0.4
Water bulk modulus	K_w	[kPa]	2.2×10^6	2.2×10^6
Soil grain bulk modulus	K_s	[kPa]	1.0×10^{10}	1.0×10^{10}
Permeability	k	[m/s]	1.0×10^{-1}	1.0×10^{-1}

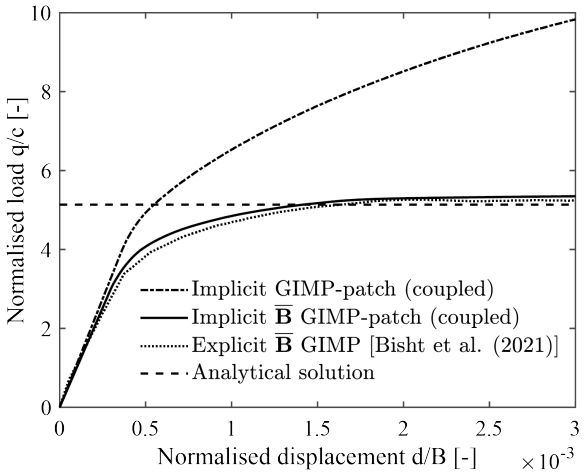

Figure 5.3: SD relationship between normalised load (q/c) and displacement (d/B) for the undrained bearing capacity problem in Figure 5.2

versions. Even for an SD analysis in which the displacements are negligible, Figure 5.4a shows that the implicit GIMP-patch method generates spurious stress oscillations when no anti-locking measures are undertaken. In contrast, the corresponding picture arising from the $\overline{\mathrm{B}}$ analysis shows the typical compression bulb under the foundation without any undesired oscillations (Figure 5.4b).

To explore the influence of space discretisation in the implicit $\overline{\mathrm{B}}$ GIMP-patch method, Figure 5.5 shows the load-displacement curves obtained with four different space discretisations ($h = 0.5\,\mathrm{m}$, $0.25\,\mathrm{m}$, $0.1\,\mathrm{m}$, and $0.05\,\mathrm{m}$). In all cases, the implicit $\overline{\mathrm{B}}$ GIMP-patch solution captures the undrained bearing capacity of the strip footing, with a clearly converging trend towards Prandtl's solution as finer background meshes are considered.

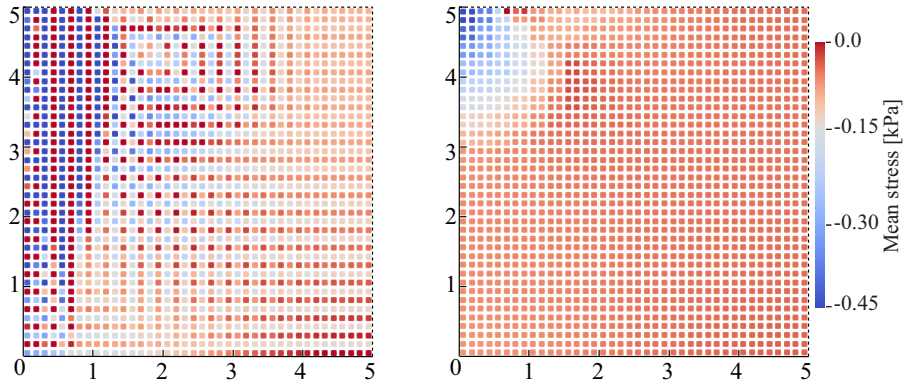

(a) implicit GIMP-patch method (b) implicit $\overline{\text{B}}$ GIMP-patch method

Figure 5.4: SD mean stress distribution associated with the last calculation step of the analyses in Figure 5.3: (a) implicit GIMP-patch method by Zheng *et al.* (2021a) vs (b) implicit $\overline{\text{B}}$ GIMP-patch method (this study). The horizontal and vertical axes refer to distance non-dimensionalised with respect to the foundation width B

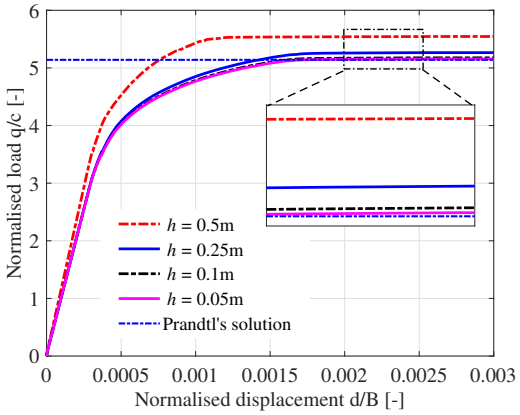

Figure 5.5: SD mesh sensitivity of the implicit $\overline{\text{B}}$ GIMP-patch method for the undrained bearing capacity problem in Figure 5.2 (including a zoom-in on the detail at bearing failure)

LARGE-DEFORMATION ANALYSIS

The static, undrained bearing capacity of a strip footing under large deformations (LD) has previously been studied within a one-phase total stress framework using a variety of numerical methods, including the Arbitrary Lagrangian-Eulerian (ALE) approach (Nazem *et al.*, 2006, 2009), sequential limit analysis (Da Silva *et al.*, 2011), the remeshing and interpolation technique with small strain (RITSS) (Wang *et al.*, 2015), and MPM (Sołowski & Sloan, 2015; Woo & Salgado, 2018; Iaconeta *et al.*, 2019; Kiriyama & Higo, 2020; Bisht *et al.*, 2021). In what follows, the LD performance of the (coupled) implicit $\overline{\text{B}}$ GIMP-patch method is assessed, following the same adopted strategy as in the previous SD sub-section, i.e., with a sufficiently slow application of the external load (0.1 kPa/s) and,

therefore, negligible pore pressure build-up. It is also worth mentioning that, within the MPM framework, it is rather difficult to exactly enforce natural boundary conditions such as surface tractions, due to the substantial displacement of MPs associated with LD processes. Therefore, it has been preferred to model the footing in Figure 5.2 as a solid of increasing unit weight, which easily enables the application of a desired vertical pressure – as previously done by Kiriyama & Higo (2020). For comparison purposes, the simulated load–displacement curve for the foundation has been obtained by calculating the external pressure via the average contact force between the footing block and the underlying (weightless) soil.

In Figure 5.6, the load-displacement curves obtained through the implicit $\overline{\text{B}}$ GIMP-patch method, and grid cell sizes of $h = 0.25\,\text{m}$ and $0.125\,\text{m}$, are plotted. The LD solutions from explicit $\overline{\text{B}}$ GIMP (Bisht *et al.*, 2021), RITSS (Wang *et al.*, 2015), and sequential limit analysis (Da Silva *et al.*, 2011) are also included for comparison – note that the soil is modelled as a strictly rigid-plastic material in the case of sequential limit analysis (Da Silva *et al.*, 2011), whereas typical elasto-plastic behaviour is assumed in all other numerical solutions. It can be observed that the implicit $\overline{\text{B}}$ GIMP-patch solution is in good agreement with other LD results from the literature. The small differences between the $\overline{\text{B}}$ GIMP-patch solutions and the others solutions are likely to be due to the use of a relatively coarse/structured grid in this study, while locally refined meshes have been adopted in the referenced studies.

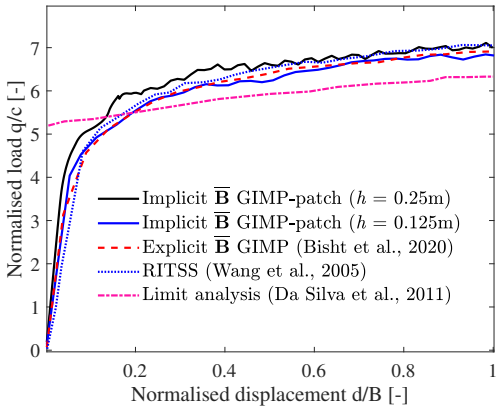

Figure 5.6: LD normalised load-displacement curves for the undrained bearing capacity problem in Figure 5.2

To further assess the LD performance of the implicit $\overline{\text{B}}$ GIMP-patch method, Figure 5.7 illustrates the distributions of the mean (effective) stress distribution and the deviatoric plastic strain invariant $\epsilon_p^d = \sqrt{2/3\boldsymbol{e}_p : \boldsymbol{e}_p}$ (with $\boldsymbol{e}_p$ being the deviatoric plastic strain tensor) associated with a normalised settlement of the footing equal to $d/B = 1$. Also under LD conditions, the mean stress field is mostly oscillation-free and exhibits a well-shaped compression bulb – see Figure 5.7a. However, some small oscillations are still visible near the bottom-right corner of the footing block, where substantial relocation of the MPs takes place during LD settlement. Such a relocation can lead to a discontinuous support

domain of MPs (see also Charlton (2018)) and, as a consequence, cause stress oscillations (though not due to locking effects). In Figure 5.7b, large values of deviatoric plastic strain appear around the foundation, which compare well with the quantitative observations of Iaconeta *et al.* (2019) and Bisht *et al.* (2021).

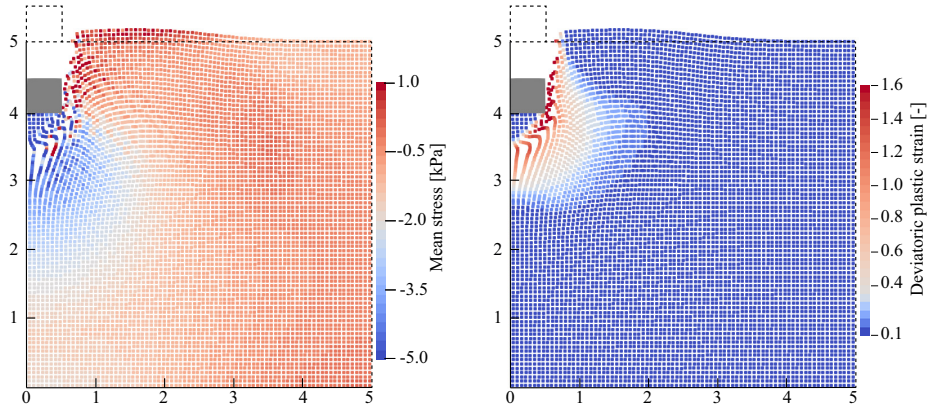

(a) mean stress (b) deviatoric plastic strain

Figure 5.7: LD mean stress and deviatoric plastic strain distributions associated with the last calculation step of the analyses in Figure 5.6 (grid cell size $h = 0.125\,\text{m}$). The horizontal and vertical axes refer to distance non-dimensionalised with respect to the foundation width B

5.4.2. EARTHEN SLOPE FAILURE

In this section, the performance of the implicit $\overline{\text{B}}$ GIMP-patch method is evaluated with respect to slope failure processes triggered by gravity. As is shown in Figure 5.8, the reference slope comprises two soil layers that are henceforth referred to as 'upper' and 'lower' (foundation) layers – all material properties are listed in Table 5.2. The free surface of the slope is unconstrained and freely draining, while the lateral and bottom boundaries are impermeable and supported by rollers. In both example cases considered hereafter, the problem domain has been discretised by means of four-node quadrilateral grid cells of size $0.2\,\text{m} \times 0.2\,\text{m}$, with each cell initially hosting four equally-spaced MPs; implicit time integration has been performed with a time step size of $\Delta t = 5.0 \times 10^{-2}\,\text{s}$.

UNDRAINED ANALYSIS OF SLOPE FAILURE IN SOFTENING CLAY

Undrained slope failure is simulated by resorting to the same total stress approach adopted in Section 5.4.1 – a Tresca-like soil behaviour has been introduced to obtain an isochoric material response. It should be mentioned that an artificially large permeability has been set for the clay, so as to enable total stress/one-phase modelling while using a two-phase formulation – indeed, this simple expedient prevents the build-up of pore pressures during one-phase undrained analyses. To reproduce the gradual reduction in undrained strength during soil sliding, a simple cohesion degradation mechanism has been incorporated into the constitutive law (Wang *et al.*, 2018); specifically by prescribing a linear reduction between the peak (c_p) and residual (c_r) shear strength values with

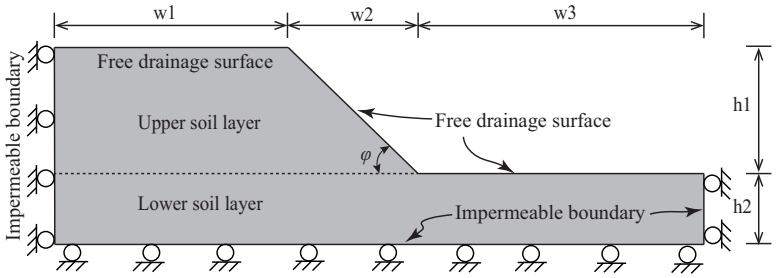

Figure 5.8: Reference slope stability problem: computational domain and boundary conditions

Table 5.2: Soil properties associated with the reference slope in Figure 5.8

Property	Symbol	Clay slope		Sand slope	
		Upper layer	Lower layer	Upper layer	Lower layer
Young's modulus	E [kPa]	1000	1000	1000	1000
Poisson's ratio	ν [-]	0.49	0.49	0.3	0.3
Soil grain density	ρ_s [kg/m^3]	2650	2650	2650	2650
Water density	ρ_w [kg/m^3]	1000	1000	1000	1000
Friction angle	ϕ [°]	0	0	25	25
Initial dilation angle	ψ_{ini} [°]	0	0	-5	-5
Critical dilation angle	ψ_r [°]	0	0	0	0
Dilation evolution parameter	η [-]	–	–	-25.0	-25.0
Peak cohesion	c_p [kPa]	6.4	20.0	3.0	20.0
Residual cohesion	c_r [kPa]	3.6	20.0	3.0	20.0
Deviatoric plastic strain for c_r	ϵ_p^r [-]	0.75	0.75	–	–
Initial porosity	n [-]	0.4	0.4	0.4	0.4
Water bulk modulus	K_w [kPa]	2.2×10^6	2.2×10^6	2.2×10^6	2.2×10^6
Soil grain bulk modulus	K_s [kPa]	1.0×10^{10}	1.0×10^{10}	1.0×10^{10}	1.0×10^{10}
Permeability	k [m/s]	1.0×10^{-1}	1.0×10^{-1}	1.0×10^{-1}	$\sim 1.0\times10^{-6}$

accumulated plastic deviatoric strain ϵ_p^d, and c_r being attained for a value of ϵ_p^d equal to ϵ_p^r, with the latter being an additional material parameter. Note that a much larger strength is assigned to the foundation layer (Table 5.2), in order to force slope failure to occur within the upper layer. Furthermore, the investigation of possible grid-dependence effects associated with strain-softening are out of the scope of this study. The size of the computational domain is defined, with reference to Figure 5.8, by $w_1 = 4.0\,\text{m}$, $w_2 = 2.0\,\text{m}$, $w_3 = 4.0\,\text{m}$, $h_1 = 2.0\,\text{m}$, and $h_2 = 1.0\,\text{m}$, with the slope inclination being $\varphi = 45°$.

Two slope failure analyses have been carried out using both the original and $\overline{\text{B}}$ versions of the implicit GIMP-patch method, according to the following two steps: (i) generation of the initial soil stresses by gradually applying gravity in combination with kinematic constraints to prevent immediate slope deformation; (ii) free slope deformation and failure under its own weight with a degrading cohesion (the peak cohesion in Table 5.2 has been purposely selected to render the 45° slope unstable). In contrast to the footing problem in Section 5.4.1, the gravity-driven failure of a slope does not allow the attainment of a limit response with exactly no pore pressure build-up, not even if a very

large permeability value is used. Therefore, the pore pressure degrees-of-freedom have been forcedly set to zero in the MPM code to study the anti-locking performance of the implicit $\overline{\text{B}}$ GIMP strategy in a large-deformation problem involving material plasticity and softening.

Figure 5.9 shows the mean (total) stress contours at four different time instants, namely $t = 0\,\text{s}$, $1\,\text{s}$, $3\,\text{s}$, and $5\,\text{s}$. Figure 5.9a confirms that severe stress oscillations are returned by the implicit GIMP-patch method without a proper mitigation of volumetric locking. Such oscillations become particularly apparent where plastic straining takes place most intensely (i.e., near the interface between upper and lower layers – see Figure 5.10), and tend to become more severe over time. In contrast, the benefits of the $\overline{\text{B}}$ technique are confirmed once again in Figure 5.9b, even in the presence of material softening. Furthermore, Figure 5.10 also shows how locking can significantly affect the slope failure mechanism: the implicit GIMP-patch method returns a completely 'locked' deformation pattern, whereas significant slope run-out is obtained with the $\overline{\text{B}}$-enhanced calculations. This confirms the possibly extreme consequences of volumetric locking, and the practical importance of its remediation in large-deformation problems.

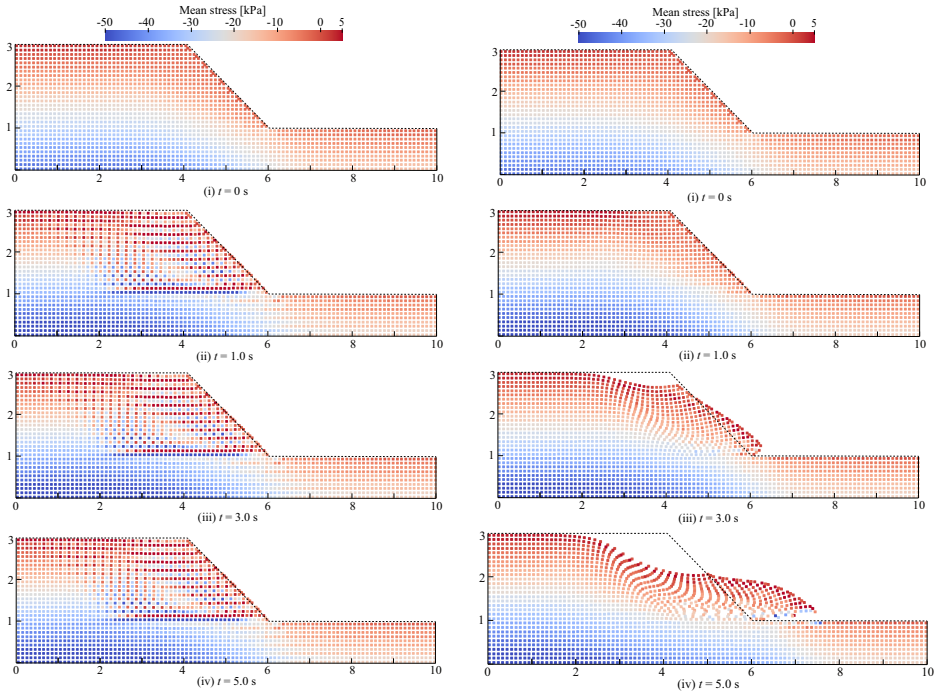

(a) implicit GIMP-patch method

(b) implicit $\overline{\text{B}}$ GIMP-patch method

Figure 5.9: Time evolution of mean stress in the soil during undrained slope failure in softening clay. Results obtained through (a) implicit GIMP-patch method and (b) implicit $\overline{\text{B}}$ GIMP-patch method

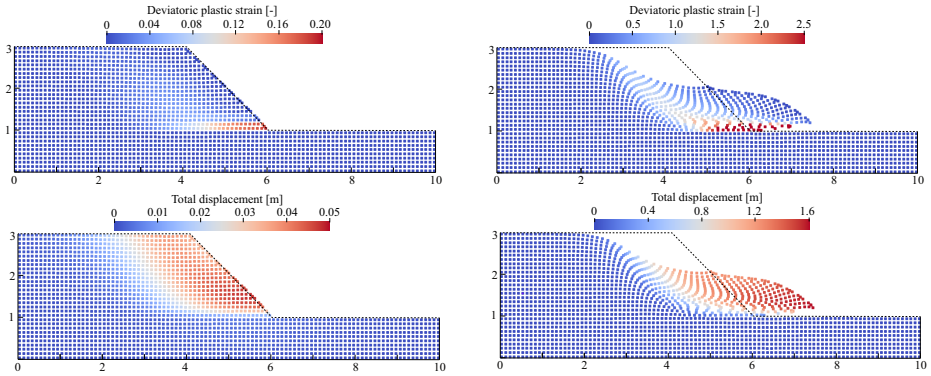

(a) implicit GIMP-patch method

(b) implicit $\overline{\text{B}}$ GIMP-patch method

Figure 5.10: Final distributions of deviatoric plastic strain and total displacement associated with undrained slope failure in softening clay. Results obtained through (a) implicit GIMP-patch method; (b) implicit $\overline{\text{B}}$ GIMP-patch method

5

COUPLED ANALYSIS OF SLOPE FAILURE IN WATER-SATURATED SAND

In this example, the coupled analysis of a sandy slope collapsing under its self-weight is tackled using the implicit $\overline{\text{B}}$ GIMP-patch method. The problem domain in Figure 5.8 is defined by $w_1 = 4.0\,\text{m}$, $w_2 = 2.0\,\text{m}$, $w_3 = 5.0\,\text{m}$, $h_1 = 2.0\,\text{m}$, and $h_2 = 1.0\,\text{m}$, and the slope inclination is $\varphi = 45°$.

Sand behaviour has been simply modelled through the standard, state-independent Mohr-Coulomb model. To more realistically capture the contractive plastic response of a loose sand, a negative initial dilation angle (ψ_{ini}) has been adopted at the beginning of the analysis; upon plastic straining, the dilation angle evolves with deviatoric plastic strain ϵ_p^d towards its (nil) critical state value (ψ_{crit}) according to the following relationship (Lei *et al.*, 2020):

$$\psi = \psi_{crit} + \left(\psi_{ini} - \psi_{crit}\right) e^{-\eta \epsilon_p^d} \tag{5.17}$$

where η is a material parameter governing the variation of ψ with ϵ_p^d. The material properties chosen for this example are listed in Table 5.2 and include, for simplicity, constant values of cohesion and frictional angle. Some small cohesion has been introduced for the upper layer to enable smoother calculations under low mean effective stress; conversely, an unrealistically large cohesion has been set for the foundation layer, with the sole goal of containing the slope failure within the upper layer.

Figure 5.11 shows the contours of pore pressure and mean effective stress at four different time instants, obtained with a soil permeability k of $1.0 \times 10^{-4}\,\text{m/s}$. The gradual development of slope failure due to shear banding is also visible and the slope face (indicated by the dashed line) is compared to the initial geometry (indicated by the dotted line). During all phases of the slope failure, the implicit $\overline{\text{B}}$ GIMP-patch method returns perfectly smooth, oscillation-free distributions of effective stress and pore water pressure. In particular, as failure develops, positive (compressive) excess pore pressures build up as high deviatoric plastic straining takes place, which is consistent with the choice of a negative dilation angle for the soil. The excess pore pressure begins to gradually

dissipate after about 1.25 s, i.e., as the slope gradually approaches its final equilibrium configuration.

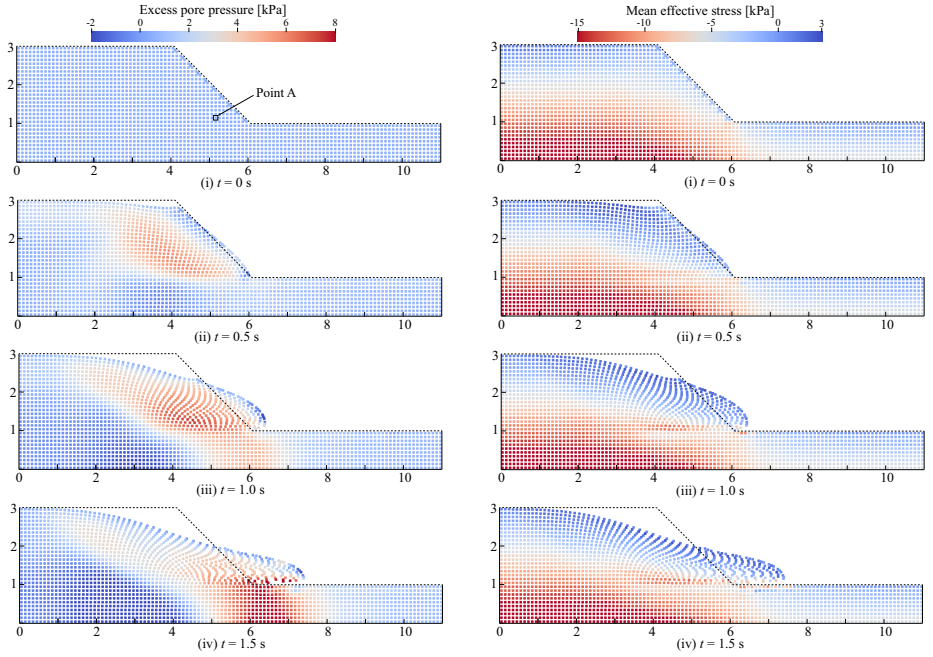

(a) excess pore pressure (b) mean effective stress

Figure 5.11: Time evolution of excess pore pressure and mean effective stress during slope failure in water-saturated sand. Results obtained with soil permeability $k = 1.0 \times 10^{-4}$ m/s and initial dilatancy angle $\psi_{ini} = -5°$

To appreciate the influence of soil permeability on the results of the coupled analysis, the final configuration of the slope at $t = 50.0$ s is shown in Figure 5.12 for three different k values. As expected, the numerical model captures correctly that larger soil displacements develop at the slope toe as the permeability is reduced. Such an occurrence is clearly due to the build-up of larger pore pressures, and therefore to a more pronounced reduction in mean effective stress and, proportionally, soil shear resistance. On a related note, Figure 5.13 displays the time evolution of the excess pore pressure (difference between the current/total pore pressure value and the hydrostatic pore pressure value at the start of simulation) at a point initially located near the slope toe – point A in Figure 5.11a. The figure confirms that larger pore pressure peaks are attained for lower permeability values, with a slower pore pressure dissipation afterwards. The latter is a consequence of the larger drag forces $\boldsymbol{R}$ that locally arise with low permeability, which in turn hinders the relative displacement of the soil skeleton and pore water (see Section 5.2.1). On the other hand, the oscillatory pore pressure dissipation trends obtained for low k values reflect the more pronounced dynamic effects that are associated with a farther/faster soil run-out (Figure 5.12).

The impact of the deviatoric–volumetric coupling on soil behaviour is numerically investigated by considering different values of the initial dilation angle (ψ_{ini} in Equation

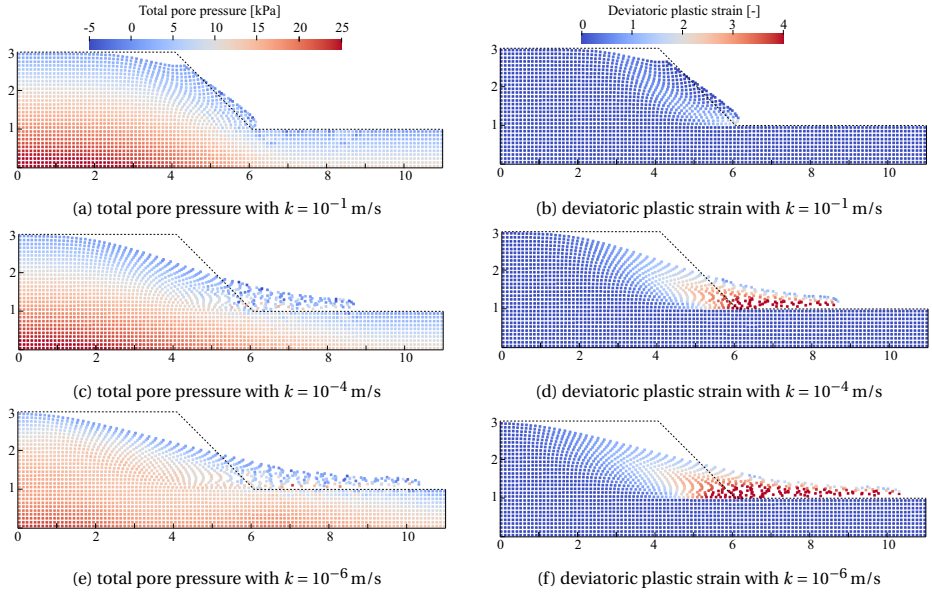

(a) total pore pressure with $k = 10^{-1}$ m/s

(b) deviatoric plastic strain with $k = 10^{-1}$ m/s

(c) total pore pressure with $k = 10^{-4}$ m/s

(d) deviatoric plastic strain with $k = 10^{-4}$ m/s

(e) total pore pressure with $k = 10^{-6}$ m/s

(f) deviatoric plastic strain with $k = 10^{-6}$ m/s

Figure 5.12: Configuration after slope failure (at $t = 50.0$ s) in water-saturated sand for different values of soil permeability, and associated contours of total pore pressure and deviatoric plastic strain. Results obtained with initial soil dilatancy angle $\psi_{ini} = -5°$

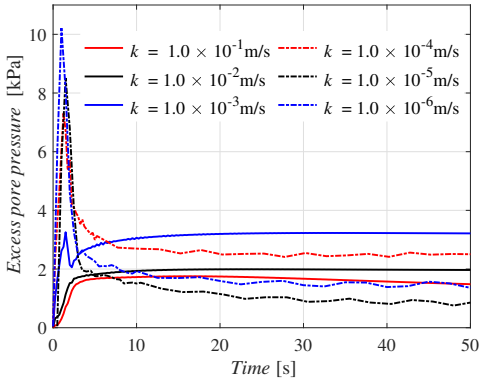

Figure 5.13: Time evolution of the excess pore pressure at the point A shown in Figure 5.11a (initially located near the slope toe) for different values of soil permeability. Results obtained with soil initial dilatancy angle $\psi_{ini} = -5°$

(5.17)), namely $-5°$ (contractive soil), $0°$, and $5°$ (dilative soil), in combination with a soil permeability of $k = 1.0 \times 10^{-4}$ m/s. The distributions of the total displacement and the deviatoric plastic strain at the end of the simulation ($t = 50.0$ s) are shown in Figure 5.14. It is evident that the slope toe undergoes rather limited displacement when dilative soil behaviour is considered, whereas considerable slope deformation takes place in the case

of a contractive soil. Such occurrences mainly stem from the fact that much larger positive excess pore pressures build up when the soil is contractive, which can lead to a significant reduction in the mean effective stress across the soil domain, and therefore to a lower resistance to shear loading. In contrast, negative excess pore pressures result during the deviatoric plastic straining of a dilative soil, which ultimately limits the deformations experienced by the slope as a consequence of an enhanced resistance to shear. These observations are further supported by the excess pore pressure curves plotted in Figure 5.15 for the same point A (near the slope toe) as indicated in Figure 5.11a. The figure confirms the qualitative expectations about the relationship between the value of ψ_{ini} and the sign of the resulting excess pore pressure (Navas *et al.*, 2018).

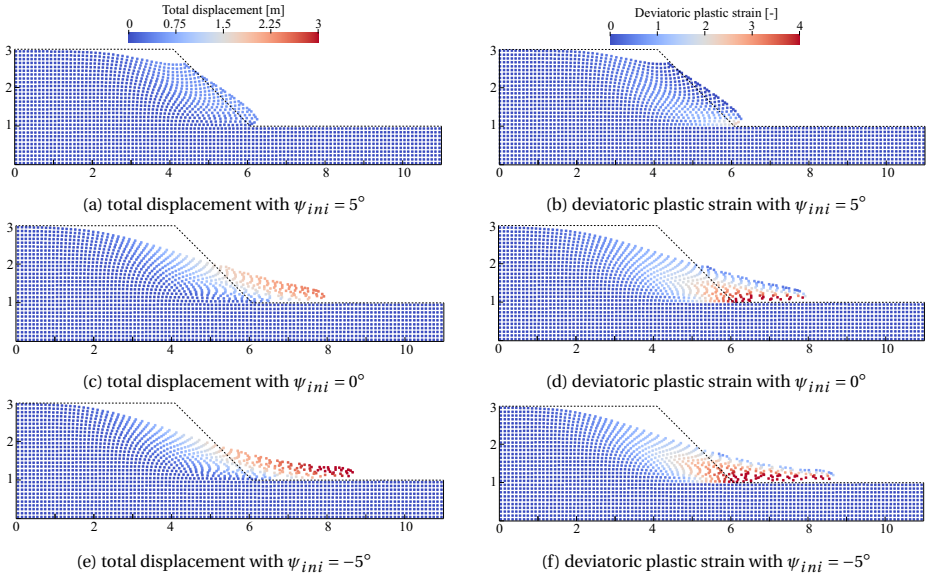

(a) total displacement with $\psi_{ini} = 5°$ (b) deviatoric plastic strain with $\psi_{ini} = 5°$

(c) total displacement with $\psi_{ini} = 0°$ (d) deviatoric plastic strain with $\psi_{ini} = 0°$

(e) total displacement with $\psi_{ini} = -5°$ (f) deviatoric plastic strain with $\psi_{ini} = -5°$

Figure 5.14: Configuration after slope failure (at $t = 50.0\,\text{s}$) in water-saturated sand for different values of the initial soil dilatancy angle ψ_{ini}, and associated contours of total displacement and deviatoric plastic strain. Results obtained with soil permeability $k = 1.0 \times 10^{-4}\,\text{m/s}$

5.4.3. BEARING CAPACITY OF A STRIP FOOTING NEAR A SLOPE

As a final application example, the implicit $\overline{\text{B}}$ GIMP-patch method is used to analyse the bearing capacity of a rough strip footing near the crest of a cohesive–frictional, water-saturated slope. The computational model and the associated boundary conditions are displayed in Figure 5.16. The slope comprises two layers of fluid-saturated soil; $B = 1\text{m}$ is the breadth of the foundation, while $\lambda \cdot B$ denotes the distance between the footing edge and the slope crest. The relevant domain dimensions in Figure 5.16 are $w_1 = 13.0\text{B}$, $w_2 = 5.0\text{B}$, $w_3 = 8.0\text{B}$, $h_1 = 5.0\text{B}$, and $h_2 = 1.0\text{B}$ – note that the a rather large w_1 has been chosen to avoid boundary effects for all the values of $\lambda \cdot B$ considered in the following. The strip footing has been modelled as a stiff elastic block with a Young's modulus $E_f = 10\,000\,\text{kPa}$ and a Poisson's ratio $\nu_f = 0.3$, while the Mohr–Coulomb

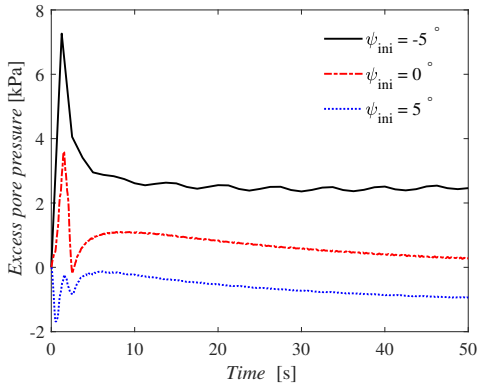

Figure 5.15: Time evolution of the excess pore pressure at the same point A indicated in Figure 5.11a (initially located near the slope toe) for different values of the initial soil dilatancy angle ψ_{ini}. Results obtained with soil permeability $k = 1.0 \times 10^{-4}$ m/s

5

parameters of the soil are listed in Table 5.3. Numerical simulations have been performed using a time step size of $\Delta t = 5 \times 10^{-2}$ s and a loading rate of 20.0 kPa/s. Both the footing and the soil base have been discretised through 4-node quadrilateral grid cells of size 0.5 m × 0.5 m, with each cell initially hosting 2 × 2 equally-spaced MPs. The main purpose of this example case is to demonstrate the suitability of the proposed $\overline{\text{B}}$ GIMP-patch method to study the interplay between the foundation failure and slope collapse mechanism as a function of the footing-to-crest distance.

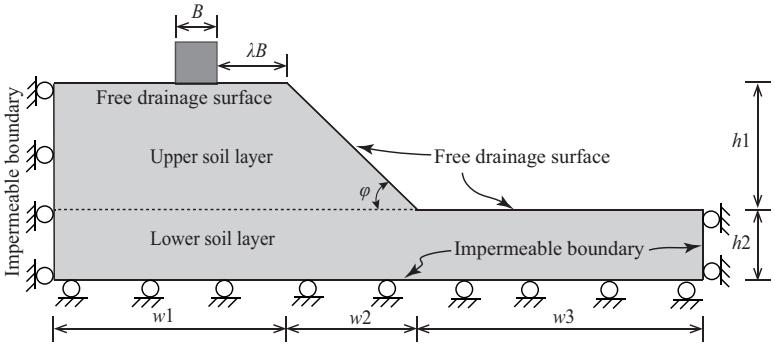

Figure 5.16: Reference footing–slope interaction problem: computational domain and boundary conditions (not to scale)

Figure 5.17 shows how the footing-to-crest distance factor λ affects the large-deformation response of the foundation under the vertical pressure q. The distance between the footing edge and the slope crest has a significant influence on the bearing capacity, which tends to increase for larger values of λ and converge to the case of a foundation on level ground with no slope – see the strong similarity of the responses associated with $\lambda = 6$ and $\lambda = \infty$. The influence of the footing-to-crest distance becomes gradually

Table 5.3: Soil properties associated with the footing–slope interaction problem in Figure 5.16

Property	Symbol	Unit	Upper layer	Lower layer
Young's modulus	E	[kPa]	1000	1000
Poisson's ratio	ν	[-]	0.3	0.3
Soil grain density	ρ_s	[kg/m^3]	2650	2650
Water density	ρ_w	[kg/m^3]	1000	1000
Friction angle	ϕ	[°]	25	25
Initial dilation angle	ψ_{ini}	[°]	-5	-5
Critical dilation angle	ψ_r	[°]	0	0
Dilation evolution parameter	η	[-]	-25.0	-25.0
Cohesion	c	[kPa]	20.0	50.0
Initial porosity	n	[-]	0.4	0.4
Water bulk modulus	K_w	[kPa]	2.2×10^6	2.2×10^6
Soil grain bulk modulus	K_s	[kPa]	1.0×10^{10}	1.0×10^{10}
Permeability	k	[m/s]	1.0×10^{-4}	1.0×10^{-4}

more evident as the foundation response enters the large-deformation regime, i.e., after a settlement of about $0.1B$. The lack of a well-defined capacity plateau may be due to concurrent factors that gradually manifest themselves as large foundation settlement takes place. Such factors include (i) the growing contribution to the total capacity offered by the lower soil layer with larger cohesion (see Table 5.3) as well as (ii) the increase in lateral surcharge, which results in enhanced overburden and confinement. These phenomena are reproduced owing to the large-deformation nature of the performed MPM simulations, and are quantitatively impacted by the specific setting of soil's dilatancy properties.

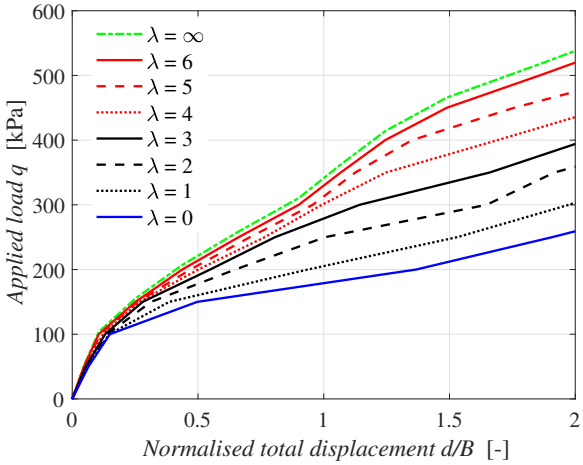

Figure 5.17: Influence of the footing-to-crest distance on the large-deformation load–displacement response of the foundation in Figure 5.16

Figure 5.18 shows contours of excess pore pressure and deviatoric plastic strain associated with a foundation settlement equal to $2B$ and different values of λ . As expected, the

largest pore pressure values emerge in the vicinity of the footing, though with a smaller magnitude as λ decreases and more effective water drainage through the slope surface occurs. λ also affects the type of governing failure mechanisms. For a small footing-to-crest distance (e.g., $\lambda = 0-2$ in Figure 5.18), the failure mechanism is dominated by the development of a shear band through the slope, that is from the footing to the slope toe – as a consequence, the footing experiences a significant in-plane rotation during its collapse. In contrast, larger λ values determine a decreasing influence of the slope, so that a clear vertical foundation failure is first observed prior to a general sideways displacement of the soil towards the slope.

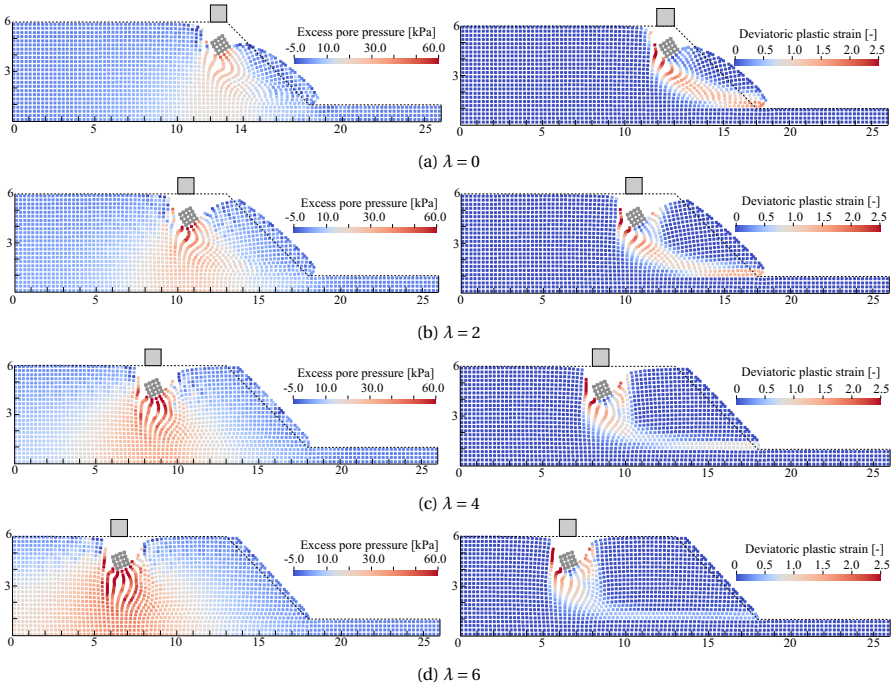

Figure 5.18: Final excess pore pressure (left) and deviatoric plastic strain (right) distributions associated with the footing–slope interaction problem in Figure 5.16. Results obtained with soil permeability $k = 1.0 \times 10^{-4}$ m/s at a total footing settlement equal to $2B$

5.5. CONCLUSIONS

This chapter has presented a numerical method for the analysis of large-deformation hydro-mechanical problems in fluid-saturated elastoplastic geomaterials. The proposed method belongs in the family of MPMs, and builds on the combination of the recently proposed implicit GIMP-patch method and the $\overline{\text{B}}$ kinematic enhancement against volumetric locking. The need for such an enhancement is motivated by the spurious stress oscillations and excessively stiff responses that are obtained when there is a lack of specific anti-locking measures, especially when a (nearly) isochoric behaviour of the soil

skeleton is considered. Details about the formulation and implementation of the implicit $\overline{\text{B}}$ GIMP-patch method have been provided starting from a three-field u–p–U formulation of the coupled hydro-mechanical problem. The proposed $\overline{\text{B}}$ GIMP-patch method has been evaluated through several 2D benchmark problems (footing bearing capacity, slope failure, and footing–slope interaction), and found to be largely satisfactory in terms of accuracy, stability, and anti-locking performance. Further applications to more complex large-deformation coupled problems and soil constitutive relationships, including proper treatment of finite-strain kinematics, will be tackled in future work.

REFERENCES

Abe, K., Soga, K. & Bandara, S. (2013). Material point method for coupled hydromechanical problems. *Journal of Geotechnical and Geoenvironmental Engineering* **140**, No. 3, 04013033.

Bandara, S. & Soga, K. (2015). Coupling of soil deformation and pore fluid flow using material point method. *Computers and Geotechnics* **63**, 199–214.

Bardenhagen, S. G. & Kober, E. M. (2004). The generalized interpolation material point method. *Computer Modeling in Engineering and Sciences* **5**, No. 6, 477–496.

Bisht, V., Salgado, R. & Prezzi, M. (2021). Simulating penetration problems in incompressible materials using the material point method. *Computers and Geotechnics* **133**, 103593.

Charlton, T. J. (2018). *An implicit generalised interpolation material point method for large deformation and gradient elasto-plasticity*. Ph.D. thesis, Durham University.

Coombs, W. M., Charlton, T. J., Cortis, M. & Augarde, C. E. (2018). Overcoming volumetric locking in material point methods. *Computer Methods in Applied Mechanics and Engineering* **333**, 1–21.

Da Silva, M., Krabbenhoft, K., Lyamin, A. & Sloan, S. (2011). Rigid-plastic large-deformation analysis of geotechnical penetration problems. *Proceedings of the IACMAG* **1**, 42–47.

González Acosta, L. J., Vardon, P. J. & Hicks, M. A. (2017). Composite material point method (CMPM) to improve stress recovery for quasi-static problems. *Procedia Engineering* **175**, 324–331.

González Acosta, L. J., Vardon, P. J. & Hicks, M. A. (2021). Development of an implicit contact technique for the material point method. *Computers and Geotechnics* **130**, 103859.

González Acosta, L. J., Vardon, P. J., Remmerswaal, G. & Hicks, M. A. (2020). An investigation of stress inaccuracies and proposed solution in the material point method. *Computational Mechanics* **65**, No. 2, 555–581.

Holzapfel, A. G. (2000). *Nonlinear solid mechanics ii*. Wiley: New York.

Hughes, T. J. (1980). Generalization of selective integration procedures to anisotropic and nonlinear media. *International Journal for Numerical Methods in Engineering* **15**, No. 9, 1413–1418.

Hughes, T. J. (1987). *The finite element method: linear static and dynamic finite element analysis*. Prentice-Hall.

Iaconeta, I., Larese, A., Rossi, R. & Oñate, E. (2019). A stabilized mixed implicit material point method for non-linear incompressible solid mechanics. *Computational Mechanics* **63**, No. 6, 1243–1260.

Jassim, I., Stolle, D. & Vermeer, P. (2013). Two-phase dynamic analysis by material point method. *International Journal for Numerical and Analytical Methods in Geomechanics* **37**, No. 15, 2502–2522.

Kiriyama, T. & Higo, Y. (2020). Arbitrary particle domain interpolation method and application to problems of geomaterial deformation. *Soils and Foundations* **60**, No. 6, 1422–1439.

Kularathna, S., Liang, W., Zhao, T., Chandra, B., Zhao, J. & Soga, K. (2021). A semi-implicit material point method based on fractional-step method for saturated soil. *International Journal for Numerical and Analytical Methods in Geomechanics* .

Kularathna, S. & Soga, K. (2017). Implicit formulation of material point method for analysis of incompressible materials. *Computer Methods in Applied Mechanics and Engineering* **313**, 673–686.

Lei, X., He, S. & Wu, L. (2020). Stabilized generalized interpolation material point method for coupled hydro-mechanical problems. *Computational Particle Mechanics* , 1–20.

Mast, C., Mackenzie-Helnwein, P., Arduino, P., Miller, G. R. & Shin, W. (2012). Mitigating kinematic locking in the material point method. *Journal of Computational Physics* **231**, No. 16, 5351–5373.

Navas, P., Sanavia, L., López-Querol, S. & Rena, C. Y. (2018). u–w formulation for dynamic problems in large deformation regime solved through an implicit meshfree scheme. *Computational Mechanics* **62**, No. 4, 745–760.

Nazem, M., Carter, J. P., Sheng, D. & Sloan, S. W. (2009). Alternative stress-integration schemes for large-deformation problems of solid mechanics. *Finite Elements in Analysis and Design* **45**, No. 12, 934–943.

Nazem, M., Sheng, D. & Carter, J. P. (2006). Stress integration and mesh refinement for large deformation in geomechanics. *International Journal for Numerical Methods in Engineering* **65**, No. 7, 1002–1027.

Newmark, N. M. (1959). A method of computation for structural dynamics. *Journal of the Engineering Mechanics Division* **85**, No. 3, 67–94.

Sołowski, W. & Sloan, S. (2015). Evaluation of material point method for use in geotechnics. *International Journal for Numerical and Analytical Methods in Geomechanics* **39**, No. 7, 685–701.

Tran, Q.-A. & Sołowski, W. (2019). Temporal and null-space filter for the material point method. *International Journal for Numerical Methods in Engineering* **120**, No. 3, 328–360.

Wang, B., Vardon, P. J. & Hicks, M. A. (2018). Rainfall-induced slope collapse with coupled material point method. *Engineering Geology* **239**, 1–12.

Wang, D., Bienen, B., Nazem, M., Tian, Y., Zheng, J., Pucker, T. & Randolph, M. F. (2015). Large deformation finite element analyses in geotechnical engineering. *Computers and Geotechnics* **65**, 104–114.

Woo, S. I. & Salgado, R. (2018). Simulation of penetration of a foundation element in tresca soil using the generalized interpolation material point method (GIMP). *Computers and Geotechnics* **94**, 106–117.

Zhang, F., Zhang, X., Sze, K. Y., Lian, Y. & Liu, Y. (2017). Incompressible material point method for free surface flow. *Journal of Computational Physics* **330**, 92–110.

Zhao, Y. & Choo, J. (2020). Stabilized material point methods for coupled large deformation and fluid flow in porous materials. *Computer Methods in Applied Mechanics and Engineering* **362**, 112742.

Zheng, X. C., Pisanò, F., Vardon, P. J. & Hicks, M. A. (2021a). An explicit stabilised material point method for coupled hydromechanical problems in two-phase porous media. *Computers and Geotechnics* **135**, 104112.

Zheng, X. C., Pisanò, F., Vardon, P. J. & Hicks, M. A. (2021b). Formulation and verification of a fully implicit three-field material point method for dynamic coupled problems , Under review.

Zheng, X. C., Pisanò, F., Vardon, P. J. & Hicks, M. A. (2022). Fully implicit, stabilised MPM simulation of large-deformation problems in two-phase elastoplastic geomaterials , In preparation.

Zienkiewicz, O. & Shiomi, T. (1984). Dynamic behaviour of saturated porous media; the generalized Biot formulation and its numerical solution. *International Journal for Numerical and Analytical Methods in Geomechanics* **8**, No. 1, 71–96.

Zienkiewicz, O. C., Chan, A., Pastor, M., Schrefler, B. & Shiomi, T. (1999). *Computational geomechanics with special reference to earthquake engineering*. John Wiley & Sons.

Zienkiewicz, O. C., Taylor, R. L. & Zhu, J. Z. (2005). *The finite element method: its basis and fundamentals*. Elsevier.

6

Conclusions and Recommendations

6.1. CONCLUDING REMARKS

THE Material Point Method (MPM) has been gaining increasing popularity as a suitable approach to the solution of coupled hydro-mechanical problems involving large deformations. Most previous studies have presented coupled MPMs based on the v–w formulation of the relevant governing equations, the use of low-order interpolation functions, and explicit time integration (conditionally stable). Importantly, MPM has been known to perform poorly in the presence of incompressibility constraints when built on low-order spatial interpolation (such as standard MPM and GIMP) and in the absence of special measures against pore pressure instabilities and volumetric locking. Moreover, in nearly or fully incompressible porous materials, the use of explicit time integration is inevitably associated with extremely small time steps, which seriously limits the applicability of MPM to couple large deformation problems of significant duration. Since only limited MPM work has so far been devoted to the mentioned numerical issues, this work has built on the need to find viable and robust solutions within the framework of coupled MPM modelling.

This thesis has contributed to the improvement of MPM modelling capabilities for large-deformation dynamic problems in fluid-saturated geomaterials, with emphasis on the development and verification of stabilised coupled MPM approaches, as well as on their application to practical geotechnical problems. Three main developments have thus been proposed in this thesis: (i) an explicit stabilised single-point two-field (v–w form) GIMP method with Selective Reduced Integration (GC-SRI-patch), including the patch recovery of pore pressure increments based on a Moving Least Square Approximation (MLSA) and the two-phase extension of the Composite Material Point Method (CMPM) for effective stress recovery; (ii) a fully implicit stabilised single-point three-field (u–p–U form) GIMP method (GIMP-patch), which combines enhanced GIMP shape functions with an MLSA-based patch recovery scheme for pore pressures; (iii) a fully implicit $\overline{B}$ GIMP-patch method, which introduces the anti-locking $\overline{B}$ approach to the implicit GIMP-patch method to tackle large-deformation problems in (nearly) isochoric elastoplastic geomaterials, particularly by remedying the numerical inaccuracies caused by volumetric locking.

The accuracy and computational performance of the proposed methods have been demonstrated with reference to several verification examples and practical applications, spanning different regimes of material deformation (small versus large) and dynamic motion (slow versus fast). The main conclusions of this research are summarised in what follows.

6.1.1. EXPLICIT STABILISED GC-SRI-PATCH METHOD

In Chapter 3, a single-point two-phase fully coupled GIMP method based on a dynamic velocity formulation (v–w form) of the governing hydromechanical equations has been developed in combination with explicit time integration. To achieve accurate recovery of pore pressures at the material points (MPs) and mitigate pore pressure instabilities in the vicinity of the undrained-incompressible limit, a patch recovery based on a Moving Least Square Approximation (MLSA) has thus been proposed for mapping pore pressure increments from Gauss Points (GPs), where a selective reduced integration (SRI) has been adopted to evaluate the pore pressures at the centre of each background cell, to MPs.

The CMPM has been introduced to recover effective stresses and strains at MPs using an enlarged problem domain and shape functions of higher order. The resulting GC-SRI-patch method, which combines GIMP, SRI with MLSA-based patch recovery, and CMPM, has been proven to provide accurate solutions for a number of benchmark problems. In particular, the improvements brought by the GC-SRI-patch method with respect to the simpler GIMP method have been demonstrated for one-dimensional consolidation examples (both small and large deformation analysis) and for the study of an axisymmetric hollow cylinder subjected to internal pressurisation. Instead of piecewise constant pore pressures over each cell, the proposed method returns continuous pore pressure distributions both within grid cells and at inter-cell boundaries. In particular, in the case of 1D large deformation consolidation, the large pore pressure oscillations near the upper domain boundary would lead GIMP simulations to abort after significant displacement of the MPs, while the GC-SRI-patch method can more accurately reproduce relevant analytical solutions. Furthermore, the applicability of the explicit stabilised GC-SRI-patch method has been demonstrated through the simulation of a 2D slumping block problem. It has been shown that the simulated excess pore pressures inside the poroelastic block evolve smoothly in time and without the spurious oscillations that the explicit GIMP method would return.

6.1.2. FULLY IMPLICIT STABILISED GIMP-PATCH METHOD

It is known that the explicit GC-SRI-patch method, similarly to most coupled MPM formulations from the literature, is only conditionally stable, which imposes extreme limitations on the selection of the time step size. As a consequence, the need for stable time integration restricts the applicability of explicit coupled MPM to problems of considerable size and/or duration. To enable the use of larger time steps and more convenient stability properties, a new, fully implicit, stabilised GIMP using a single-point three-field (u–p–U) formulation has been introduced in Chapter 4. As for the explicit method presented in Chapter 3, the implicit stabilised GIMP also adopts an MLSA-based patch recovery to obtain accurate pore pressure fields when the undrained-incompressible limit is approached. Relevant aspects regarding the numerical implementation of the implicit GIMP-patch method have been discussed in detail, including the iterative solution scheme required by the geometrical non-linearity even for linear poroelastic media.

The developed implicit GIMP-patch method has been tested with respect to benchmark problems including the dynamic consolidation of a soil column (both for small and large deformations), the propagation of a shock pressure wave, and the slumping of a 2D poroelastic block. Special attention has been dedicated to comparing the computational performances of the implicit GIMP-patch method and the explicit GC-SRI-patch method described in Chapter 3. It has been shown that the implicit GIMP-patch method can provide accurate, stable, and oscillation-free results that are closely comparable to relevant analytical solutions (where available) and also to numerical results obtained using the explicit GC-SRI-patch method, over different inertial and deformation regimes. The computational convenience of the implicit GIMP-patch method lies in the possibility to use relatively large time steps – however, the superior efficiency with respect to the explicit GC-SRI-patch method tends to gradually reduce as problems of increasing size (number of degrees-of-freedom) are tackled.

6.1.3. IMPLICIT $\overline{B}$ GIMP-PATCH METHOD: APPLICATION TO ELASTOPLASTIC COUPLED PROBLEMS

To enable the implicit GIMP-patch analysis of coupled large-deformation problems also in (nearly) incompressible elastoplastic geomaterials, the implementation of the anti-locking $\overline{B}$ approach has been described in Chapter 5. The effectiveness of the $\overline{B}$ approach has first been tested for the case of a strip footing undergoing both small and large settlements on an incompressible soil (in this case, the original coupled formulation has been set to work according to the one-phase total stress approach by using a very large permeability and the isochoric Tresca plasticity model). To further demonstrate the applicability of the proposed method to relevant geotechnical problems, two typical coupled geotechnical applications have also been studied: (i) the failure of an earthen slope and (ii) the bearing capacity of a strip footing near the crest of a slope. In particular, the failure of slopes in (a) undrained softening clay and (b) water-saturated sand, as well as the mechanisms of footing–slope interaction, have been discussed in detail. In all the analysed cases, the implicit $\overline{B}$ GIMP-patch method has been shown to be accurate and stable, and to successfully mitigate the detrimental effects of volumetric locking. In the case of slope failure problems, the proposed method has proven to be a suitable tool for the analysis of landsliding phenomena, including the quantification of the unstable soil mass and its possible run-out distance upon slope instability.

6.2. RECOMMENDATIONS FOR FUTURE RESEARCH

BOTH the explicit and the implicit coupled MPMs have been developed in this work as tools for the modelling of large deformation dynamic problems in fluid-saturated geomaterials. Their success and applicability may be further enhanced by considering the following recommendations for future research. It is particularly recommended to:

- *develop a more accurate boundary detection algorithm.* Even when a fixed background mesh is used in MPM computations, the mesh nodes may not always coincide with the domain boundaries. This may lead to an inaccurate representation of the domain boundaries, and therefore frequently cause substantial pore pressure oscillations – especially in the vicinity of a free surface under relatively complex boundary conditions (such as the enforcement of an external surface traction and/or inflow/outflow boundary conditions). While in this study the attention has been limited to rather simple cases, more work should be devoted to enable the enforcement of complex boundary conditions in combination with the occurrence of large soil deformations;

- *incorporate more advanced soil constitutive models.* In this thesis, only the standard Mohr–Coulomb model (in some instances with strain-softening) has been adopted to investigate elasto-plastic large-deformation processes, since the main focus of the study has been the development and validation of a stabilised MPM. It is clear that more advanced soil constitutive models, including proper treatment of finite-strain kinematics, are required in order to realistically capture the most complex features of hydro-mechanical behaviour in large deformation analyses, e.g., in relation to the coupled progressive/retrogressive failure of slopes and earthquake-

induced liquefaction phenomena;

- *develop robust contact algorithms in coupled MPM that account for soil–water–structure interaction (SWSI)*, which is essential for the study of numerous large-deformation geotechnical problems such as pile installation. So far, only very few studies have been published on the inclusion of SWSI using MPM, especially for two-phase large-deformation problems. Further research on large-deformation dynamic problems including the presence of SWSI would be extremely interesting and relevant to engineering practice;

- *introduce more efficient parallel computing and develop a 3D version of the current coupled MPM code.* Even though the implicit time integration scheme can significantly improve the efficiency of the explicit coupled MPM in large-deformation analyses, the computational time will increase considerably as problems of larger size are considered. It is thus recommended that more efficient parallel computing should be introduced into the coupled MPM code developed herein, in order to enable the faster solution of 2D problems and, eventually, to make the extension to 3D problems computationally viable;

- *incorporate non-local mesh regularisation methods.* Similarly to the case of FEM, the results of coupled MPM simulations may strongly depend on the adopted background mesh and suffer from pathological mesh-dependency in the presence of strain-localisation phenomena (though not addressed in detail in this thesis). The adoption of non-local regularisation techniques is therefore recommended as a possible countermeasure, so as to obtain objective MPM solutions.

An interesting thread of future research will be to take further the achievements of this dissertation towards their practical application to earthquake engineering problems. It is anticipated that the computational techniques developed in this work for coupled MPM modelling will positively impact the study of seismically-induced landslides and dam failures, with an emphasis on combining large-deformation processes, possible soil fluidisation (liquefaction) effects, and post-failure evolution of the system at hand. Application to the analysis of foundation installation problems, such as vibratory pile driving, is also a natural future development of this dissertation, in that it is closely related to the ability of modelling the large-deformation dynamics of fluid-saturated soils.

A

Composite Material Point Method (CMPM)

A

THIS appendix summarises how shape functions are constructed in the Composite Material Point Method (CMPM) proposed by González Acosta *et al.* (2017, 2020) to improve stress calculations at MPs. As an extended support domain is used in CMPM, new shape functions are required to envelop all the cells inside the extended supported domain. Figure A.1 shows the C^2 shape functions for a central local grid cell in the 1D case. Using Lagrange interpolation, each shape function N^2 envelops both the local grid cell and its neighbour grid cells and is written as:

$$N_n^2(\xi) = \prod_{m=1;\, m\neq j}^{n} \frac{\xi - \xi_m}{\xi_j - \xi_m} \tag{A.1}$$

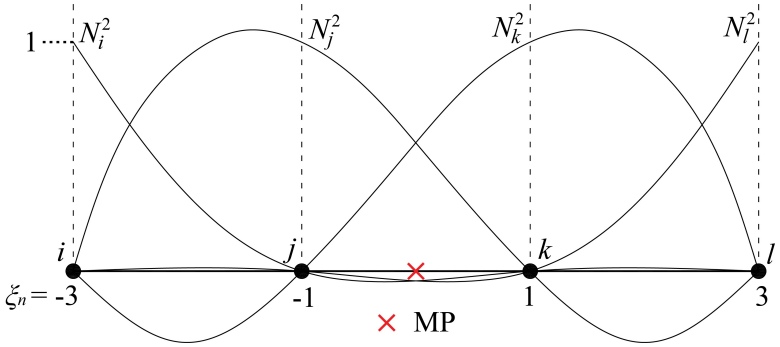

Figure A.1: CMPM shape functions with C^2 continuity for a central local grid cell

where ξ is the nodal local coordinate in the extended domain, n is the total number of nodes, ξ_j is the local coordinate of the N_i^2 shape function, and ξ_m defines the local coordinate of the remaining nodes. The shape function for a cell with two neighbour cells (i.e., MPs located in central grid cells) are computed by solving Equation (A.1):

$$\begin{bmatrix} N_i^2 \\ N_j^2 \\ N_k^2 \\ N_l^2 \end{bmatrix} = \begin{bmatrix} -\frac{1}{48}(\xi^3 - 3\xi^2 - \xi + 3) \\ \frac{1}{16}(\xi^3 - \xi^2 - 9\xi + 9) \\ \frac{1}{16}(-\xi^3 - \xi^2 + 9\xi + 9) \\ \frac{1}{48}(\xi^3 + 3\xi^2 - \xi - 3) \end{bmatrix} \tag{A.2}$$

The CMPM shape functions for a cell with only one neighbour cell (i.e., MPs located in a boundary cell) can be written as

$$\begin{bmatrix} N_i^1 \\ N_j^1 \\ N_k^1 \end{bmatrix} = \begin{bmatrix} \frac{1}{8}(\xi^2 - 4\xi + 3) \\ \frac{1}{4}(-\xi^2 + 2\xi + 3) \\ \frac{1}{8}(\xi^2 + 4\xi + 3) \end{bmatrix} \tag{A.3}$$

and are shown in Figure A.2.

It should be mentioned that the above shape functions can only be used for a structured background mesh. In 2D/3D problems, shape functions are computed by multiplying the individual 1D functions in the different directions.

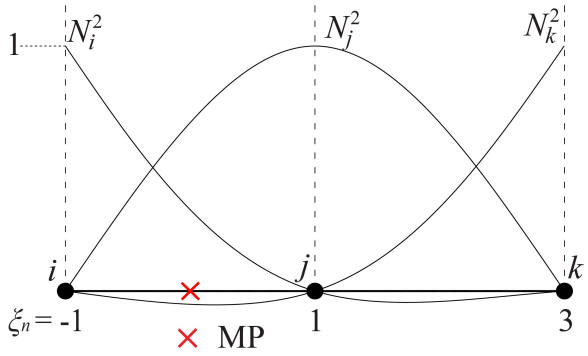

Figure A.2: CMPM shape functions with C^1 continuity for a boundary local grid cell

REFERENCES

González Acosta, L. J., Vardon, P. J. & Hicks, M. A. (2017). Composite material point method (CMPM) to improve stress recovery for quasi-static problems. *Procedia Engineering* **175**, 324–331.

González Acosta, L. J., Vardon, P. J., Remmerswaal, G. & Hicks, M. A. (2020). An investigation of stress inaccuracies and proposed solution in the material point method. *Computational Mechanics* **65**, No. 2, 555–581.

NOTATION

ACRONYMS

ALE	Arbitary Lagrangian–Eulerian method
BSMPM	B-spline Material Point Method
CEL	Coupled Eulerian–Lagrangian method
CMPM	Composite Material Point Method
CPDI	Convected Particle Domain Interpolation method
DDMP	Dual Domain Material Point method
FEM	Finite Element Method
FLIP	Fluid Implicit Particle method
GIMP	Generalised Interpolation Material Point method
GPs	Gauss Points
LD	Large Deformation analysis
MLSA	Moving Least Squares Approximation
MPM	Material Point Method
MPs	Material Points
OTM	Optimal Transportation Meshfree method
PFEM	Particle Finite Element Method
PIC	Particle In Cell method
RITSS	Remeshing and Interpolation Technique with Small Strain
SD	Small Deformation analysis
SPH	Smoothed Particle Hydrodynamics method
SRI	Selective Reduced Integration
UL-FEM	Updated Lagrangian Finite Element Method

GREEK SYMBOLS

β, γ	Implicit time integration parameters
χ_{mp}	Particle characteristic function
Ω	Configuration of problem domain

Ω_{mp}	Support domain of MP
ρ	Soil–water mixture density
ρ_s	Soil grain density
ρ_w	Water density
σ	Total stress
σ'	Effective stress
$\dot{\boldsymbol{\varepsilon}}$	Strain rate
$\tilde{\boldsymbol{\tau}}$	Prescribed boundary values of surface traction

LATIN SYMBOLS

c_v	Coefficient of consolidation
J	Jacobian of the deformation gradient tensor
K_s	bulk modulus of the soil particles
K_w	bulk modulus of the water phase
n	Initial porosity
n_{gp}^t	Weighted porosity evaluated at the central GP position
N_{gp}	Total number of GPs in the approximation domain Ω_i
$N_i(x)$	Linear shape function
p	Pore water pressure
Q	Stiffness parameter defined as $1/Q = n/K_w + (1-n)/K_s$
$\dot{s}_0$	Rate of soil volume expansion due to thermal changes
$S_{i,mp}(x)$	GIMP shape function
$\nabla S_{i,mp}(x)$	Gradient of GIMP shape function
U_s	Average degree of consolidation
V_{mp}	Volume of MP
$\boldsymbol{a}$	Vector containing interpolation degrees-of-freedom
$\boldsymbol{b}$	External body force
$\mathbf{B}$	Compatibility matrix containing spatial derivatives of the shape function
$\overline{\mathbf{B}}$	Modified global compatibility matrix
$\mathbf{C}$	Damping matrix physically associated with grain–fluid drag
$\boldsymbol{D}$	Tangent stiffness matrix of the solid skeleton
$\bar{\boldsymbol{f}}_s$	Nodal force vector relating to external body force

$\bar{\boldsymbol{f}}_w$	Nodal force vector relating to surface traction
$\mathbf{G}$	Matrix describing the hydromechanical coupling between the skeleton deformation and pore water flow
$\mathbf{K}_u$	Stiffness matrix of the solid skeleton
$\boldsymbol{m}$	Kronecker tensor
$\mathbf{M}$	Diagonal mass matrix
$\mathbf{P}$	Compressibility matrix determined by the bulk stiffness of the solid grains and pore water
$\tilde{\boldsymbol{p}}_w$	Prescribed boundary values of pore pressure
$\boldsymbol{Q}$	Vector containing polynomial basis functions
$\boldsymbol{R}$	Drag force exchanged by the soil skeleton and the pore water
$\mathbf{S}$	Differential divergence operator
$\boldsymbol{u}$	Absolute displacement of the soil skeleton
$\boldsymbol{u}^r$	Displacement of the water phase relative to the solid phase
$\boldsymbol{U}$	Total water displacement
$\boldsymbol{v}_s$	Velocity of solid phase
$\boldsymbol{v}_w$	Velocity of water phase
$\tilde{\boldsymbol{v}}_s$	Prescribed boundary values of the solid velocity
$\tilde{\boldsymbol{v}}_w$	Prescribed boundary values of the water velocity
$\boldsymbol{w}$	Average (Darcy) velocity of the water phase relative to the solid phase

ACKNOWLEDGEMENTS

FIRST and foremost, I wish to express my deepest gratitude to my promotor Prof. Michael A. Hicks and daily supervisor Dr. Federico Pisanò for their continuous guidance, support, and patience during the past four years. Prof. Hicks gave me such a precious opportunity to pursue my doctor study in TU Delft. I really enjoyed the countless discussions with him during this journey. His unconditional trust and encouragement made me feel I was always on the right way (even though sometimes I wasn't). I extremely appreciated all freedom he gave me during all of my PhD, which allowing me to explore different possibilities of the research topic. Dr. Pisanò has always given me valuable comments and guided me in the right direction throughout the project. His vast knowledge and experience substantially enriched my work, and the clarity that he brought to the research paper has always added new perspective. I also would like to thank Dr. Phil Vardon for his constructive comments about my research work, and his extensive knowledge of my research topic contributed so much to my work. I really appreciated the working relationship and personal friendship with the three of them.

Many thanks to the China Scholarship Council (CSC) and the Geo-Engineering section for their financial support. Thanks to my friends and colleagues: Leon, Guido, Anne-Catherine, Xuehui, Na, Haoyuan, Weiyuan, Vagelis, Divya, Varun, Stefano, Arash, Ali, Ivo, Kaiyue, Qiang, Zheng, Aoxi, Yu'en, Huan, Rui, Langzi, Liang, Xiaocong, Junhai, Hilmi for the wonderful time we spent, especially Leon and Guido for their kind helps and fruitful discussions. Special thanks to my previous teachers: Prof. Junsheng Yang, Dr. Feng Yang and Prof. Shuying wang for their continuous guidance and support.

I also would like to thank my PhD committee for their valuable time and providing me with their insightful feedback, which greatly helped me improve my work and brought clarity to final thesis.

I am deeply grateful to my family for being there all the time and always putting me first. They undoubtedly believed that their son is excellent in every aspect. Special thanks to my mother for all she has done for the whole family. Even though she suffered from disease during all of my PhD, her love and support never stop. I sincerely wish her good health and all the best.

Last but not the least, I would like to thank my wife, Qin. I felt so lucky and happy that she has accompanied me for more than 7 years. Many thanks to her for the love, all support and understanding during my tough times. I am grateful for all that she has done for our small family. Xiwen, my little funny angel, she brought many happiness moments and laughter to me. Thanks for coming into my life and I am really looking forward to sharing every single moment with both of them.

CURRICULUM VITÆ

Xiangcou ZHENG

05-09-1991	Born in Macheng, Hubei, China.

EDUCATION

2021–now	Postdoctoral Research Associate in Offshore Foundation Systems University of Durham, United Kingdom
2017–2021	PhD candidate in Geotechnical Engineering Delft University of Technology, the Netherlands
2014–2017	Postgraduate in Civil Engineering Central South University, China
2010–2014	Undergraduate in Civil Engineering Wuhan University of Science and Technology, China

AWARDS

2017	Top 100 excellent Master's thesis in Hunan Province
2015	Graduate National Fellowship granted by Ministry of Education of China

List of Publications

Journal Publications

1. **Zheng X.C.**, Pisanò F., Vardon P.J. & Hicks M.A. (2021). An explicit stabilised material point method for coupled hydromechanical problems in two-phase porous media, *Computers and Geotechnics* **135**, 104112.

2. **Zheng X.C.**, Pisanò F., Vardon P.J. & Hicks M.A. (2022). Formulation and verification of a fully implicit three-field material point method for dynamic coupled problems, *Under review.*

3. **Zheng X.C.**, Pisanò F., Vardon P.J. & Hicks M.A. (2022). Fully implicit, stabilised MPM simulation of large-deformation problems in two-phase elastoplastic geomaterials, *Computers and Geotechnics, Accepted.*

Conference Publications

1. González Acosta J.L., **Zheng X.C.**, Vardon P.J., Pisanò F. & Hicks M.A. (2019). On stress oscillation in MPM simulations involving one or two phases, *Proceedings of the 2nd International Conference on the Material Point Method for Modelling Soil–Water–Structure Interaction*, University of Cambridge (UK).

2. **Zheng X.C.**, González Acosta J.L., Remmerswaal G., Vardon P.J., Pisanò F. & Hicks M.A. (2021).Development of a robust coupled material point method, *Challenges and Innovations in Geomechanics – Proceedings of the 16th International Conference of IACMAG*, Torino (Italy), 819-826.